University of Calabria

Department of Computer Science, Modeling, Electronics and Systems Engineering (DIMES)

UNIVERSITÀ DELLA CALABRIA

DIPARTIMENTO DI INGEGNERIA INFORMATICA, MODELLISTICA, ELETTRONICA E SISTEMISTICA

MAIC LAB

mm-wave antennas & integrated circuits

PhD in

Information and Communication Technologies (ICT)

CYCLE XXXVI

Antennas For Non-Terrestrial Networks

PhD Coordinator: Prof. Giancarlo Fortino

*Signature*_____

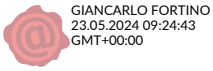

Supervisor: Prof. Luigi Boccia

*Signature*_____

PhD Candidate: Raffaele De Marco

*Signature*_____

Academic Year 2023/2024

Abstract

This doctoral thesis focuses on antennas for Non-Terrestrial Networks (NTN) and satellite communications, showcasing two innovative antenna designs.

First, a novel design for 2-D electronically steerable parasitic array radiator (ESPAR) is presented. This design is based on a 3×3 microstrip patch antenna array and it is intended to serve as a subarray within clustered phased array architecture. Compared to the existing varactor-based 2-D ESPAR designs, the proposed solution allows a continuous beam steering along eight different azimuthal planes, thus, extending the beam scanning capabilities to a conical region. Encouraged by the promising results, the concept is further extended into the Ka-band through integration into a large array configuration. This extension underscores the adaptability and practical viability of the proposed antenna concepts, paving the way for advancements in NTN and satellite communication technologies.

The second contribution involves the design of an innovative dual-band dual-polarized transmitarray antenna (TA) utilizing multilayer frequency selective surfaces (MFSS) operating at K/Ka band. The proposed design achieves an optimal compromise between aperture efficiency and thickness, compared to the existing dual-band dual-polarized transmitarrays. This design approach allows for a cost-effective and low-profile implementation, utilizing a single multilayer PCB without any air gap or vertical transition. An equivalent circuit model for the unit-cell has been formulated and examined, offering insights into the optimal phase control methodology and the transmission mechanism. The proposed design incorporates DL and UL unit-cells that are interleaved and autonomously control the transmitted phase for each band and polarization. Moreover, the proposed unit-cell and transmitarray are versatile, capable of scaling with varying frequencies, making them suitable for implementing other dual-band transmitarrays operating in two distinct frequency bands characterized by a substantial difference in upper and lower frequencies.

Table of Contents

List of Figures

List of Tables

Introduction

The primary objectives of this PhD thesis are centered around the aim of exploring innovative solutions in antenna design tailored for satellite communications (SatCom) and Non-Terrestrial Networks (NTN). The overarching goal is to contribute novel insights and methodologies to the field, with a specific focus on mitigating the cost and complexity associated with antenna systems. These solutions are particularly designed to overcome the challenges posed by standard phased array antennas, which tend to be expensive and complex, especially at high frequencies. By addressing these key challenges, the thesis aims to introduce advancements that foster more accessible and streamlined solutions for both satellite communications and NTN. The research delves into the development of cost-effective antenna systems based on PCB technology without compromising performance, thereby contributing to the broader goal of enhancing the efficiency and accessibility of communication technologies in non-terrestrial environments. The thesis is organized as follows: Chapter 1 provides an overview about Next Generation Wireless Communications with focusing on Non-Terrestrial Networks. Chapter 2 investigates the specifications and challenges of antenna technologies for satellite communications, discussing beam scanning antennas and reconfigurable antennas. The core contributions emerge in Chapter 3, where Electronically Steerable Parasitic Array Radiators (ESPARs) are unveiled. The exploration spans the ESPAR concept, PIN diode-based ESPAR, varactor-based ESPAR, and introduces a new design for conical beam scanning varactor-based ESPAR. In Chapter 4, the focus shifts to Transmitarray antennas (TAs), examining their concept, design techniques, and presenting a novel Low-profile Dual-Band Dual-Polarized Transmitarray based on Multilayer Frequency Selective Surfaces (MFSS). The concluding Chapter 5 encapsulates the thesis, offering a summary of the innovative solutions presented and outlining avenues for future research.

Chapter 1: Next Generation Wireless Communications

1.1 INTRODUCTION AND BACKGROUND

1.1.1 Evolution of wireless communications

Wireless communications have undergone a transformative evolution, tracing a compelling journey from rudimentary experiments to the sophisticated and interconnected networks of the present day. The evolution of wireless technology can be divided into distinct eras, each marked by significant advancements that shaped the landscape of global connectivity [1], [2]. The roots of wireless communication can be traced back to the late 19th century. Pioneers such as Nikola Tesla and Guglielmo Marconi conducted groundbreaking experiments with electromagnetic waves, laying the foundation for wireless telegraphy. Marconi's successful transatlantic radio transmission in 1901 marked a pivotal moment, demonstrating the potential of wireless communication over long distances. The early 20th century witnessed the transition from wireless telegraphy to voice communication. The advent of amplitude modulation (AM) and frequency modulation (FM) allowed for the transmission of voice and music over radio waves. This era saw the rise of radio broadcasting, becoming a mass communication medium and bringing news, entertainment, and information to households worldwide. The mid-20th century ushered in the era of mobile communications. The development of cellular networks, particularly the introduction of the first-generation (1G) mobile networks in the 1980s, marked a revolutionary shift. These networks allowed for wireless voice communication, freeing individuals from the constraints of wired connections [3]. he digital revolution of the late 20th century paved the way for wireless communications to embrace digital technologies. The advent of the second-generation (2G) and subsequent generations of mobile networks introduced digital voice and data transmission. The proliferation of mobile phones and the emergence of the internet era further accelerated the demand for wireless connectivity. The 21st century witnessed the rise of smartphones and the deployment of fourth-generation (4G) networks. The integration of high-speed data transmission, coupled with the widespread adoption of smartphones, transformed the way individuals communicate, access information, and interact with the digital world.

The current focus is on the deployment and advancement of fifth-generation (5G) networks, promising unparalleled data rates, low latency, and massive device connectivity. 5G's impact extends beyond enhanced mobile broadband to support critical applications like the Internet of Things (IoT), autonomous vehicles, and augmented reality. The Sixth-generation (6G) wireless technology represents the next frontier in communication, aiming to surpass the capabilities of 5G. Envisaged as a paradigm shift, 6G is anticipated to deliver unprecedented data rates, ultra-reliable low latency, and advanced connectivity, ushering in a new era of innovation in wireless communications.

1.1.2 Motivation and importance of next generation wireless communications

The motivation behind advancing to the next generation of wireless communications stems from the escalating demands of our increasingly connected world. Next-gen wireless technologies, such as 5G and beyond, are driven by the imperative to deliver higher data rates, ultra-reliable low latency, massive device connectivity, and improved energy efficiency. Moreover, the advent of real-time applications such as remote surgery, autonomous vehicles, and augmented reality necessitates a reduction in communication latency. The motivation for the next generation extends to minimizing delays, ensuring instantaneous response times, and facilitating applications that require near-instantaneous data exchange. The pervasive growth of the Internet of Things (IoT), encompassing a multitude of devices from smart sensors to industrial machines, calls for a paradigm shift in wireless communication capabilities. The motivation for the next generation lies in accommodating the massive scale of device connectivity intrinsic to the IoT, ensuring efficient communication, and sustaining a robust infrastructure capable of handling diverse IoT applications. Furthermore, the next generation of wireless communications acts as a catalyst for the integration and optimal functioning of emerging technologies such as artificial intelligence, edge computing, and quantum computing. The motivation stems from the imperative to create an ecosystem that seamlessly supports the coalescence of these technologies, unlocking unprecedented possibilities for innovation. Security and privacy considerations are paramount as the volume of sensitive data transmitted over wireless networks continues to rise. The drive for the next generation lies in fortifying communication channels against emerging cyber threats, employing advanced

encryption techniques, and establishing protocols that safeguard user privacy in an era of heightened digital connectivity.

1.1.3 Current challenges in wireless communications

Current challenges in wireless communications underscore the need for ongoing innovation and development. One pressing challenge is the escalating demand for bandwidth due to the proliferation of data-intensive applications and the Internet of Things (IoT). This strains existing network capacities, leading to concerns about congestion and degraded performance. Additionally, the increasing complexity and heterogeneity of wireless networks pose challenges in terms of seamless integration and interoperability. Security remains a paramount concern, with the rising threat of cyber-attacks targeting sensitive data transmitted over wireless channels. Moreover, ensuring low latency for real-time applications, such as autonomous vehicles and augmented reality, is a persistent challenge. Among all these challenges, current networks fall short of providing adequate broadband coverage to rural regions [4]. Even in the most technologically advanced countries, existing cellular infrastructures show vulnerability to natural disasters. Disruptions in connectivity amid natural disasters have the potential to hinder or delay timely responses, inflict considerable harm to businesses and properties, and, in severe cases, result in loss of life. To address these issues, 6G research is currently focusing on the development of non-terrestrial networks (NTNs) to promote ubiquitous and high-capacity global connectivity [5].

1.1.4 Emerging technologies and applications

The dynamism of wireless communications is illuminated by emerging technologies that promise to reshape the landscape. Among the most crucial advancements are:

1. 6G Technology: as the successor to 5G, 6G is an emerging wireless communication technology expected to provide unprecedented data rates, ultra-reliable low latency, and advanced connectivity.
2. Terahertz (THz) Communications: utilizing frequency bands in the terahertz range, THz communications hold promise for significantly higher data rates compared to current technologies. This can benefit applications such as high-speed wireless links and data-intensive communication in futuristic networks.

3. Quantum Communication: leveraging principles of quantum mechanics, quantum communication ensures secure and unbreakable communication channels. Quantum key distribution (QKD) is a notable application, providing a highly secure method for cryptographic key exchange.

4. Massive MIMO (Multiple Input, Multiple Output): going beyond current MIMO technologies, massive MIMO employs a large number of antennas at both the transmitter and receiver. This technology enhances spectral efficiency and enables higher data rates by serving multiple users simultaneously.

The ongoing evolution of wireless communications continues to foster innovation across various sectors, shaping the landscape of future connectivity. Numerous applications depend on wireless communication, including:

1. Internet of Things (IoT): wireless communications play a crucial role in connecting and enabling communication among IoT devices. From smart homes and wearables to industrial IoT applications, wireless connectivity forms the backbone of the IoT ecosystem.

2. Smart Cities: wireless technologies are integral to building smart cities, facilitating applications such as smart infrastructure, intelligent transportation systems, and efficient energy management.

3. Healthcare: wireless communication in healthcare enables remote patient monitoring, telemedicine, and the transmission of medical data, contributing to improved patient care and healthcare delivery.

4. Autonomous Vehicles: the development of connected and autonomous vehicles relies heavily on wireless communication technologies. Vehicular communication systems enhance safety, traffic management, and vehicle-to-everything (V2X) communication.

5. Industry 4.0: wireless communication is a cornerstone of the fourth industrial revolution, supporting smart manufacturing processes, predictive maintenance, and real-time monitoring in industrial settings.

6. Extended Reality (XR): augmented reality (AR) and virtual reality (VR) applications heavily depend on wireless communications for seamless, low-latency interactions. These technologies find applications in gaming, education, training, and entertainment.

7. Blockchain and Cryptocurrency: wireless networks facilitate the functioning of blockchain technologies and cryptocurrency transactions. Decentralized networks rely on robust and secure wireless communication channels.

1.2 6G WIRELESS TECHNOLOGY

1.2.1 Introduction to 6G

The Hexa-X project, funded by the H2020 EU initiative, serves as the pioneering 6G endeavor. It aims to define the role of 6G in societal evolution. The project outlines six primary research challenges that establish a groundwork for anticipating relevant 6G use cases, taking into account societal and economic trends. These use cases draw insights from ongoing European research activities on 6G driven through initiatives

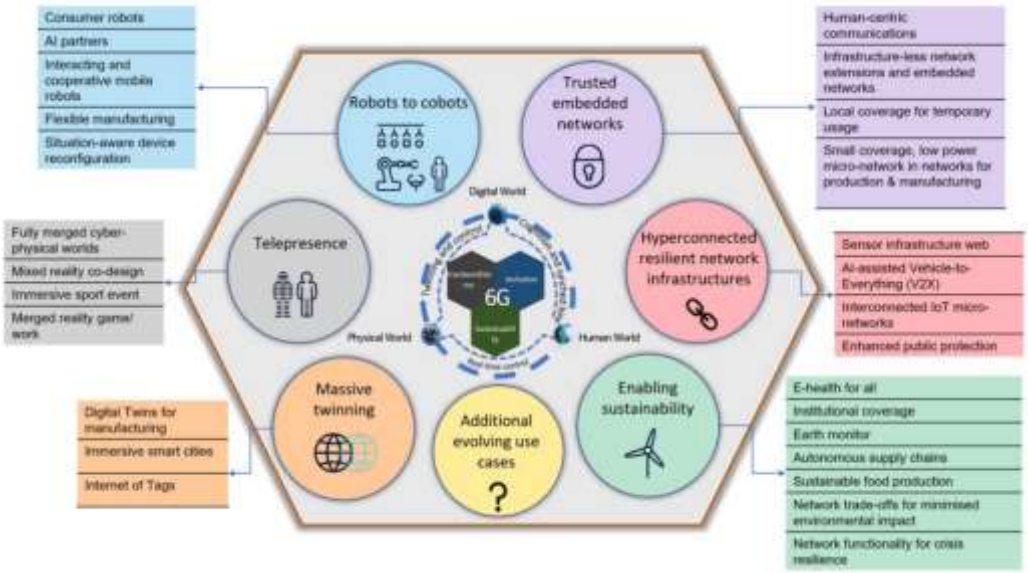

Figure 1-1 6G uses cases families [HEX-D13].

like 5G PPP and 6G-IA, as evident in [HEX-D12], [HEX-D13]. The identified use cases span a broad spectrum, ranging from evolutionary ones that extend and enhance 5G capabilities to more disruptive scenarios that unveil new possibilities for 6G to contribute to and transform society. These use cases are categorized into families based on usage types, research challenges, and addressed values, as depicted in Fig. 1-1.
Drawing insights from these use cases, their requirements, the technological trends influencing 6G architecture, and the gaps of currently 3GPP defined 5G architecture, several crucial components essential for the upcoming 6G architecture have been identified [6]: enabling AI, programmability, cloud native and service-based architecture, and continuum orchestration.

Enabling AI involves leveraging the significant advancements in computational resources, edge- and cloud-computing, along with the abundance of network and application data. This allows AI to be applied comprehensively across mobile networks, automating network operations and supporting user applications/services. For 6G systems to harness the benefits of AI, they must be AI- and computation-pervasive, necessitating a data-driven architecture. The vision is for the 6G network to optimize the air interface using AI, encompassing physical layer configuration, mobility and resource management, and QoS assurance. This transformative approach aims to turn the 6G network into a potent distributed AI platform, introducing the concept of AI as a Service (AIaaS) as a key enabler.

Programmability, a long-standing feature in network devices, has seen significant enhancement in the past decade. Spearheaded by the Software-defined Networking (SDN) paradigm and trends toward softwarization, edgification, and cloudification, programming capability for Network Functions (NFs) has evolved. The introduction of Smart Network Interface Cards (SmartNICs) and switches enables programming not only in the Control Plane (CP) but also in Data Planes (DP). Technologies like the P4 domain-specific language play a crucial role in achieving reusability and flexibility through programmability, especially at edge and extreme-edge locations. While programmability trends are expected to continue in 6G, questions remain, and competing concepts need resolution, as most deployments are still in trial phases.

Cloud native, softwarization, and service-based architecture are integral aspects of the 5G Core Network (CN), supporting a cloud-native implementation of the service-based architecture (SBA). Cloud native design involves applications built for operation in Cloud compute environments without a monolithic software codebase. Although 5G has made strides in adopting service-based principles, improvements are identified, particularly in functional allocation and procedures preventing full integration of cloud-native NFs across all domains and layers. As cloudification advances, the overall 6G architecture should ensure architectural consistency, streamline feature introduction, and facilitate customization for new end-user devices and access network topologies.

Continuum Orchestration introduces the concept of evolving regular management and orchestration techniques toward a continuum that encompasses various orchestration domains. This includes CN, transport network, edge, extreme-edge, and external networks (e.g., fixed access networks, private networks, or hyperscaler networks). While pre-5G generations primarily focused on CN for management and orchestration, 5G allowed joint management and orchestration services for both core and edge. The Continuum Orchestration concept takes this further by incorporating additional resources, emphasizing the need for a new architecture to accommodate these diverse orchestration domains effectively.

1.2.2 6G architecture

6G architecture is conceptualized as a three-layer structure, encompassing infrastructure, network service, and application layers. This hierarchical organization, illustrated in Fig. 1-2, serves as a foundational framework for the design and deployment of the next-generation wireless networks.

The infrastructure layer provides all the physical resources to host the network service and application elements. It consists of Network RAN, Network CN, and transport Networks, switches, routers, communication links, cloud infrastructure, and so on [6]. The infrastructure layer encompasses enhancements in Radio Access Network (RAN) technology, ensuring exceptionally low latency, high reliability, availability, increased data rates, enhanced capacity, cost-effective coverage, heightened energy efficiency,

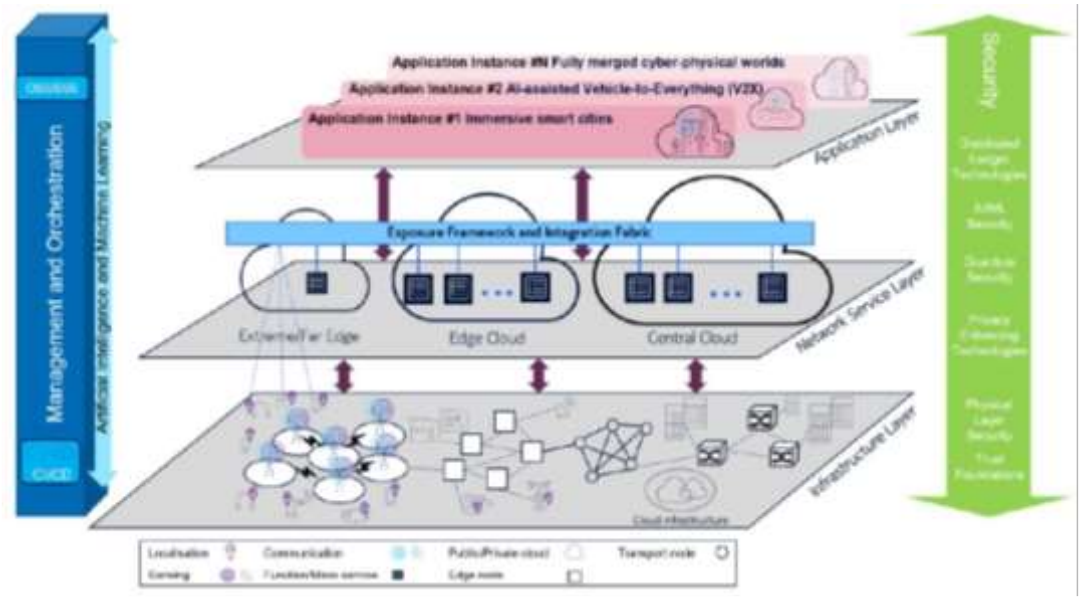

Figure 1-2 High-level view of the 6G architecture [HEX-D13].

precise localization, and integrated sensing capabilities. Further insights into the evolution of RAN technologies within the Hexa-X project can be explored in deliverables D2.1 [HEX-D21] and D2.2 [HEX-D22]. The 6G architecture integrates diverse subnetwork solutions into a dynamic network of networks. This interconnected framework exhibits adaptability and flexibility, easily conforming to new topologies to fulfill the demands of both extreme performance and global service coverage, surpassing the capabilities of 5G.

The softwarized and intelligent 6G architecture envisions the network service layer as cloud and microservice-based, expanding functions and microservices from the central cloud to the extreme edge cloud, which includes all devices beyond the Radio Access Network (RAN). The implementation of all network functions, operations, and applications as microservices paves the way for a more intelligent and efficient 6G architecture. To support AI in 6G and enable AI as a Service (AIaaS), programmability, and network automation, various enablers for an intelligent network are introduced. Additionally, adopting a cloud-native approach allows streamlining the architectures of both the RAN and Core Network (CN), reducing complexity by eliminating multiple processing points for specific messages and eliminating the duplication of functionalities among functions.

The progression in network management and orchestration involves a gradual transition toward higher levels of automation, including fully automated closed-loop control. This evolution is underpinned by concurrent advancements in AI/ML technologies. The primary objective of this shift is to establish a framework that optimally enhances reliability, flexibility, resilience, and availability. This is achieved through the concept of "continuum orchestration," which entails seamless orchestration spanning from device to edge to cloud. This approach is designed to address changes in infrastructure, evolving requirements, and potential failures within the network.

In the comprehensive architecture, security and privacy mechanisms play a vital role, impacting not only all network layers but also the management and orchestration domain. The implementation of privacy-enhancing technologies holds significance across layers where sensitive data is collected or processed, extending to the management domain. Likewise, AI/ML security assumes relevance for all functions utilizing AI/ML, involving the protection of this usage specifically. Additionally, it encompasses AI/ML-driven security mechanisms, exemplified in the management domain [UKT22].

In [6] a functional view of 6G architecture is provided, Fig. 1-3. As can be seen, four stratums have been detected. The network stratum includes CU/CPP and UP network functions responsible for ensuring the expected QoS, and an efficient data exchanging with the network. The second stratum of the functional view is the network intelligence stratum. It covers from the infrastructure environment to management plane coordinating functions in all the network ranging from the intelligent operation of network functions to the network management and orchestration. Since the network infrastructure is extended to include environmental aspects, a sensing stratum is needed to extend the network coverage area through the use of beam steering systems or Unmanned Aerial Vehicle (UAV).

The last stratum is the security one which includes all the cyber security aspects and data privacy in all the layers of the architecture up to the vertical service provider.

1.2.3 Architectural principles

In the formulation of the 6G architecture, [HEX-D51] and [EWS+22] have articulated eight distinct architectural principles. These principles are intended to function as comprehensive guidelines, steering the development process of the 6G architecture. Figure 1-4 provides a concise summary, encapsulating the essence of these architectural principles. It serves as a visual representation, offering a quick reference for the fundamental tenets shaping the overarching design framework of 6G.

Principle 1: Exposure of capabilities

The architectural solution should make both new and existing network capabilities accessible to end-to-end applications and management, including predictive orchestration. The analytical data may encompass various aspects, such as performance predictions like latency and throughput, as well as information related to localization and sensing.

Principle 2: AI for full automation

The architectural framework must facilitate complete automation for the management and optimization of the network, eliminating the need for human intervention. This

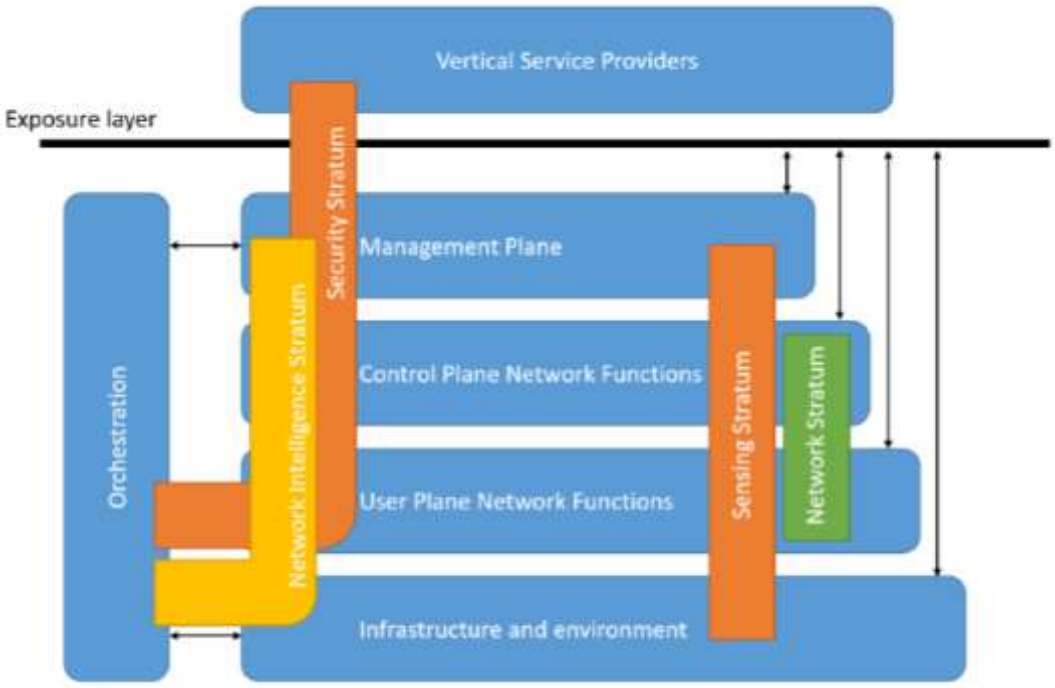

Figure 1-3 Functional view of 6G architecture [6].

closed-loop network automation is contingent on the integration of AI/ML technologies.

Principle 3: Flexibility to different topologies

The network's capability to seamlessly adjust to diverse topologies without compromising performance, all while allowing straightforward deployment. This includes its capacity to accommodate new traffic demands, respond to changes in spectrum situations, support private networks, and facilitate the creation of ad hoc mesh networks.

Principle 4: Scalability

The scalability of the network architecture is essential, encompassing support for deployments ranging from very small to very large scales. This involves the ability to adjust network resources up or down according to specific requirements.

Principle 5: Resilience and availability

The architecture must demonstrate resilience in service and infrastructure provisioning through features like multi-connectivity and the elimination of single points of failure.

Principle 6: Exposed interfaces are service based

Network interfaces should be crafted with a cloud-native design, effectively leveraging cutting-edge cloud platforms and IT tools in a cohesive and uniform manner.

Principle 7: Separation of concerns of network functions

The network functions possess a well-defined context, and their interdependencies are solely through their APIs, minimizing reliance on other network functions. This ensures that network functions can be developed, deployed, and replaced independently of one another.

Principle 8: Network simplification in comparison to previous generations

Simplify the network architecture by employing cloud-native upper-layer RAN and CN functions, featuring fewer (well-justified) parameters for configuration and a reduced number of external interfaces.

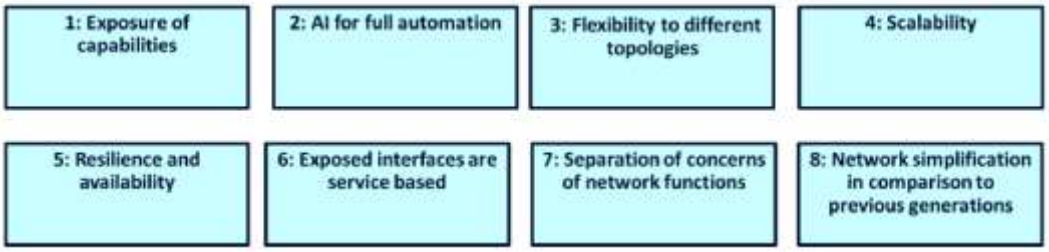

Figure 1-4 6G architecture principles from [HEX-D51].

1.2.4 Architectural enablers

From the previous section it can be inferred that new technologies are needed to implement the next generation communications infrastructure. 6G network must be an intelligent, sustainable, secure, and, most importantly, a flexible network.

Intelligent network

The Intelligent Network's ultimate goal is to facilitate autonomous and adaptable networks, minimizing human intervention. It aims to employ cognitive, closed-loop control network functions that can be activated on-demand, even across network domain boundaries. The task of the Intelligent Network involves defining the underlying mechanisms to support embedded AI for 6G and ensuring the dynamic adaptability of the network architecture to new use cases while maintaining infrastructure and energy costs at acceptable levels. Integrated AI/ML relies on intelligence distribution and management, facilitated by distributed data and AI/ML pipelines, automated closed-loop network operations, and orchestration to meet end-to-end service KPIs. Consequently, constituent network functions must be flexible to adapt to unforeseen environments. The Intelligent Network integrates various software implementations of AI functionality, diverse AI-agent setups, different learning architectures, AI-driven network orchestration, cross-domain function placement, and built-in data analytics frameworks. The 6G architecture must be designed to inherently support the integration of intelligence in the network by incorporating architecture extensions in the Network Intelligence Stratum. These extensions include a new AI-driven air interface design on RF hardware impairment compensation [FS20], channel estimation [CMWT21] and resource allocations, and development of AI functions to provide AI as a Service (AIaaS) to enable AI training, monitoring and Life Cycle Management (LCM) accounting for the specific tasks and procedures related to the

intelligence training, deployment, and monitoring [6]. The key technological enablers for 6G intelligent network are:

Network Automation: this involves replacing tasks handled by human operators with machine or software processes. In 6G networks, AI-based automation is crucial to manage technological and service complexities, ensuring quality, security, and resilience. It aims to reduce human errors in network management, enhance service provisioning speed, and address network and security issues through closed-loop operations. Customized AI/ML techniques, such as loss functions for specific network problems like capacity forecasting, play a vital role in achieving this automation.

AI as a Service: to make AI as a Service (AIaaS) accessible in 6G, new network functions and interfaces are required. This includes AI repository, training, monitoring, and AI agent functions. The architecture supports distributed AI services, facilitating AI as close to applications as possible. It involves AI service chaining for managing AI traffic flow, cross-domain AI service consumers and producers, and features like Federated Learning (FL) and Explainable AI (XAI). The AIaaS-supporting 6G network dynamically allocates resources based on service requirements and device capabilities.

Dynamic Function Placement: addressing the Network Function (NF) migration and placement problem, Dynamic Function Placement (DFP) is extended to 6G architecture. It operates across different domains, from end-user to central cloud, enabling continuum orchestration. DFP optimally deploys functions for differentiated services, supporting single and multi-domain environments. It involves monitoring cross-layer Key Performance Indicators (KPIs) for decision-making, potentially using AI/ML techniques. DFP functions include relocating function instances and transferring runtime contexts, posing challenges in defining movable runtime states and ensuring secure state transfer. Special emphasis is placed on supporting multi-domain operations in the orchestration and management scope.

Sustainable network

Sustainability, a fundamental research challenge and a foundational principle of 6G, is a comprehensive idea that encompasses environmental, social, and economic

dimensions. It revolves around satisfying current needs without jeopardizing the capacity of future generations to fulfill their own requirements. Within the context of 6G, this pertains to the sustainability of the 6G technology (Sustainable 6G) and the potential for 6G to contribute to the advancement of sustainability across various sectors of the economy, benefiting society and stakeholders (6G for Sustainability). It includes both environmental aspects and social impacts. The key targets are reduction of CO_2 emissions major than 30%, reduction of the Total Cost of Ownership (TCO) for 6G by at least 30% is targeted with respect to current networks and, reduction of the energy transmitted per bit of 90%. Some key technologies that will allow 6G to achieve the expected goals in terms of sustainability are:

1. Disaggregated and virtualized RAN: the use of a disaggregated and virtualized Radio Access Network (RAN) is highlighted. This technology allows for more flexibility and efficiency in managing network resources, contributing to the overall sustainability of the network.

2. Elastic edge computing architectures: the combination of disaggregated and virtualized RAN enables elastic edge computing architectures. This approach provides dynamic and scalable computing resources at the network edge, contributing to improved energy efficiency.

3. Energy-Efficient End-to-End (E2E) resource allocation: the text emphasizes the importance of energy-efficient resource allocation for communication, computation, and storage resources. Efficient allocation is crucial in the heterogeneous environment of 6G networks, where various technologies and resource types are employed.

4. Cloudification trend: the ongoing trend of cloudification is expected to continue in 6G. Cloud-optimized network procedures are mentioned, and the challenge lies in designing a 6G architecture that can fully utilize and interact with cloud platforms while maintaining standardization and rapid evolution.

5. Wireless power transfer and energy harvesting: technologies at the device level, such as wireless power transfer and energy harvesting, are identified as promising

techniques. These technologies target energy-neutral devices with advanced characteristics, reducing the reliance on batteries and contributing to sustainability.

6. Integration with renewable energy sources: there is a call for the combination of wireless power transfer and energy harvesting with renewable sources of energy to further enhance sustainability and environmental friendliness.

Secure network

The evolution toward next-generation networks necessitates increased security to meet the trustworthiness requirements associated with a growing number of use cases and a critical infrastructure. Trustworthiness, a key research challenge in the Hexa-X project, emphasizes the foundational role of security in establishing trust in connectivity systems. Security considerations span cyber-security aspects, including resilience against attacks, privacy preservation, and ethical application of automation, particularly AI, in network operations. Managing threat surfaces, proactive measures like prevention, and reactive measures such as attack discovery are crucial for security. As network services become essential in numerous application scenarios, their dependability and perceived trustworthiness become vital for network operators, service providers, application developers, and end-users.

Recognizing the unattainability of complete security, a balanced approach is required, considering the cost, risks, and impact of security breaches on mission objectives. The Level of Trust (LoT) in a specific network service is proposed as a key performance indicator (KPI) for evaluating trustworthiness. Analyzing security features involves identifying applicable technologies, analyzing solutions based on domain experts' experience, and understanding feasible attack patterns. The analysis of network data to enhance security and performance has seen notable progress. However, privacy concerns, especially regarding user and company data confidentiality, arise when sharing data among partners. Protecting users against malware and network attacks involves monitoring network traffic. Security analysis is imperative at all levels, considering individual technologies, planes, layers in the communications stack, network segments, and a holistic perspective addressing network services and human roles. Security activities focus on evolving base security technologies, analyzing specific solutions, and evaluating scenarios for network evolution.

The technologies that will enable a secure network include:

1. Data Access and Collaboration Control:
    - Solutions for selectively accessing and sharing data in a cooperative way for executing specific analyses.
    - Techniques for on-the-fly encryption to protect data during exchanges and collaborative computations.
    - Flexible models for representing access privileges to distributed data, supporting different visibility levels.

2. Integrity Assessment of Outsourced Computations:
    - Techniques to assess the integrity of results from computations outsourced to external parties.
    - Probabilistic techniques for detecting integrity violations in contexts where computations are not fixed a priori.
    - Formal models to evaluate the effectiveness and synergy of probabilistic techniques.

3. ML Technologies for Network Data Analysis:
    - Utilization of Machine Learning (ML) technologies for analyzing network data to enhance security and performance.
    - Advances in the analysis of network data for improved security.

4. Decentralized Blockchain-based Platform:
    - Development of a decentralized, blockchain-based platform supporting network slicing transactions via Smart Contracts.
    - Creation of a Decentralized Autonomous Organization (DAO) for dynamic negotiation of Network Slice contracts.

5. Hardware Accelerated Threat Detection:
    - Hardware-accelerated solutions for a decentralized Threat Detection Engine.
    - Centralized Threat Analysis Engine for improved performance of signature-based solutions against zero-day or evolving attacks.

- Leveraging ML-based threat detection for the design of Threat Detection Engine (TDE).

These technologies collectively address issues related to secure data access and collaboration, integrity assessment, network data analysis, decentralized platforms, and hardware-accelerated threat detection, contributing to a more secure and robust network environment. In Figure 1-5, the comprehensive architecture is depicted, illustrating the relevant security and privacy components across all domains. It emphasizes the specific 6G security technology enablers introduced in [HEX-D12].

Flexible network

Flexible networks aim to achieve exceptional performance and provide global service coverage. Therefore, the network's functionality and architecture must possess the required flexibility to adapt to diverse topologies. The concept of the "Network of Networks," as outlined in [HEX-D51] and [ECR+21], explores the utilization of technologies that support flexible topologies, enhancing connection availability and reliability. The evolution of mobile networks has grown increasingly intricate across generations. In the 4G era, discussions revolved around Heterogeneous Networks (HetNets), addressing the collaboration between wide-area macro and small-cell pico base stations. The introduction of mmWave spectrum in 5G added another layer to flexible deployment. Looking ahead to 6G, deployments will feature nodes operating in higher sub-THz spectrum with limited coverage, alongside nodes at lower frequencies offering seamless coverage. Additionally, the 6G landscape is expected to

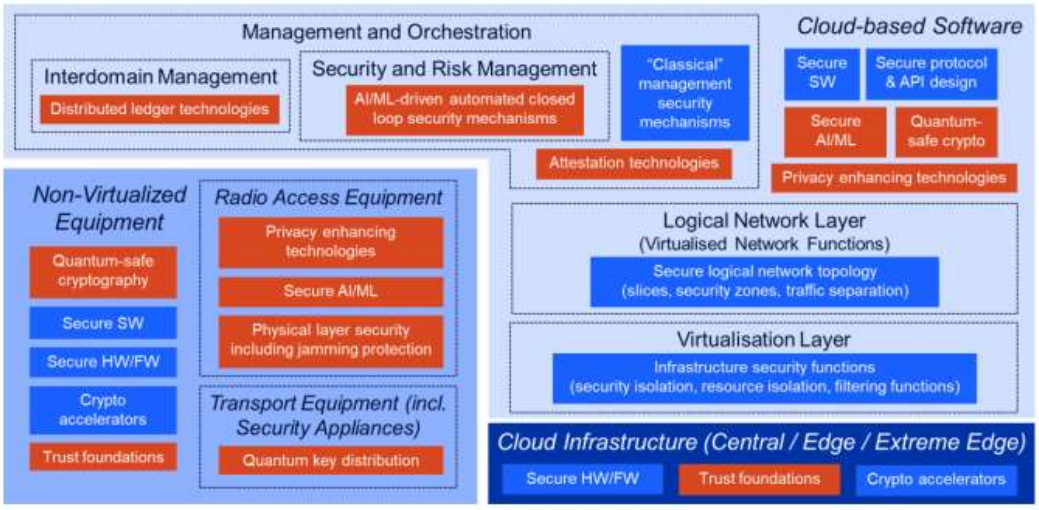

Figure 1-5 6G security architectural components [6].

witness a rise in diverse network solutions for capacity and coverage, including Distributed MIMO (D-MIMO) networks, Non-Terrestrial Networks (NTN), campus networks, mesh networks, and the cloudification of network elements. Consequently, 6G is envisioned as a network of networks, Fig. 1-6.

With the combination of Terrestrial Networks (TN) and NTNs it will be possible to achieve 100% global coverage [BFC21]. NTNs are well suitable for rural areas, oceans, or low population density areas. There are two architectural options for Non-Terrestrial Networks (NTN): Transparent and Regenerative payload architecture. The Transparent type serves as a signal relay between the User Equipment (UE) and the ground-based base station. On the other hand, the Regenerative architecture involves integrating the base station (RAN) functions onboard the satellite. A key research question for 6G revolves around solving the mobility challenges between NTN and terrestrial networks. Given the movement of Low Earth Orbit (LEO) and Medium Earth Orbit (MEO) satellites, it becomes essential to seek solutions that minimize handovers and signalling requirements for robust mobility.

Another potential enhancement for 6G involves leveraging Device-to-Device (D2D) communications within a mesh network. Although the concept of D2D communications is not new, having been discussed since 4G networks, its implementation in 6G could bring improvements such as minimizing handovers, reducing signalling needs, and enhancing the coverage and capacity of cellular

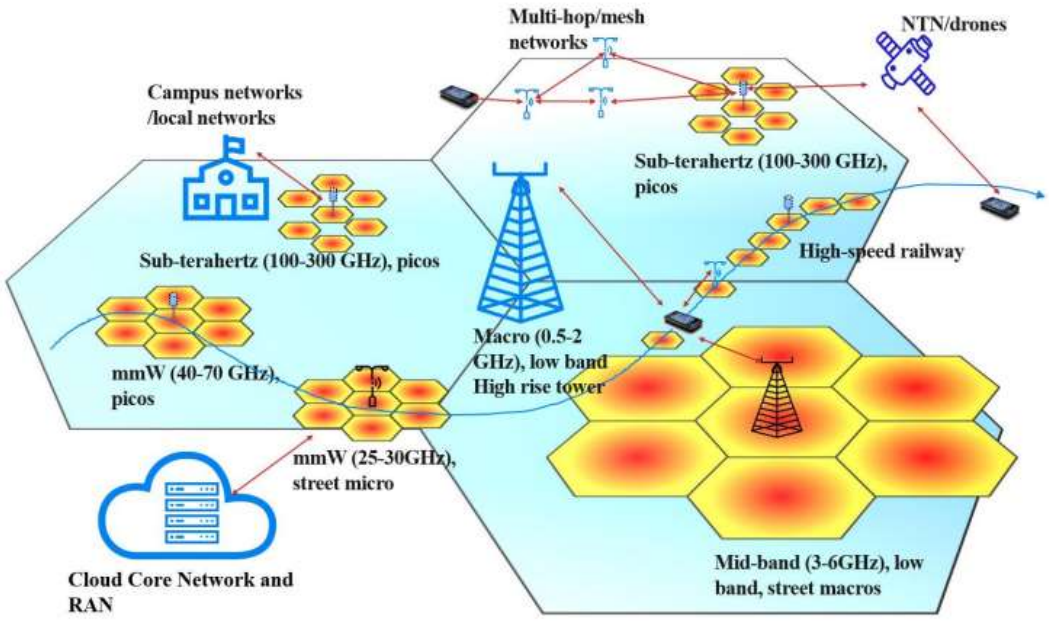

Figure 1-6 6G network of networks [HEX-D51].

networks through UE relaying. The technologies that can enable a flexible network in the context of 6G architecture include:

1. *Cloud-Native approach* is considered crucial to meeting the requirements of future network segments associated with Core Network (CN) and Radio Access Network (RAN). This approach aims to improve efficiency in terms of capacity, coverage, signalling overhead, scalability, and energy consumption.

2. *Reduction of Dependencies and Processing Points:* the redesigning of network functionalities involves performing all relevant processing for a specific network task in a single point to reduce unnecessary complexity and latency. Candidate actions to minimize the effects of dependencies include:
    - Separating subscription, policy handling, and UE capabilities for RAN.
    - Merging entities responsible for radio interface configuration to avoid delays and complexity.
    - Separating UP control for direct signaling between UP nodes, reducing latency and enabling vendor optimizations.
    - Separating UE signaling to enable separate association for UP controls, security, etc.
    - Harmonizing the service framework and context handling procedures.

3. *Function Elasticity* is identified as a key enabler for 6G architecture. Co-locating common 6G-CN Network Functions (NFs) with the 6G RAN Control Plane (RAN-CP) in the cloud environment enhances elasticity. This approach improves signalling performance and reduces latency, especially for critical signaling procedures like 6G mobility management and session management.

4. *Enhanced Signalling Possibilities* is crucial for improving 6G architecture, enabling direct signaling between NFs to eliminate potential bottlenecks. Introducing Service-Based Interfaces (SBI) allows information exchange directly between the NG-RAN NFs without passing through the Access and Mobility Management Function (AMF), thereby streamlining information transfer and reducing dependencies.

These technological approaches aim to make the 6G network more adaptive, efficient, and responsive to the diverse requirements anticipated in the 6G era.

1.3 NON-TERRESTRIAL NETWORKS

1.3.1 NTN role in Next-Gen wireless communications

In the last years, there has been a significant surge in interest in Non-Terrestrial Networks (NTNs), with both academia and industry showing a heightened enthusiasm. This heightened interest has led to the emergence of commercial solutions. One notable example is SpaceX Starlink, which provides satellite broadband services in remote areas, boasting low latency (below 30 ms) and impressive individual data rates (above 100 Mb/s).

The integration of NTNs into the evolving 6G wireless ecosystem is deemed crucial to ensure service availability, continuity, ubiquity, and scalability. Given the limitations faced by Terrestrial Networks (TN) in terms of deployment and coverage, NTNs may serve as a complementary solution to achieve global connectivity, such as through nano-satellite constellations. The deployment of a unified wireless system that incorporates both TNs and NTNs could be significantly streamlined by leveraging the same radio technology in both Radio Access Networks [7].

While earlier generations of wireless networks were conventionally crafted to offer connectivity within a quasi two-dimensional space, the concept of 6G introduces a three-dimensional (3D) heterogeneous architecture. In this envisioned structure, terrestrial infrastructures are enhanced by the inclusion of non-terrestrial stations. NTN platforms range from Geostationary/Medium/Low Earth Orbit (GEO, MEO, LEO) satellites to Unmanned Aircraft Systems (UAS), including High Altitude Platform Systems (HAPS) [8]. These elements not only offer cost-effective coverage on demand in crowded and underserved areas but also ensure trunking, backhauling, support for high-speed mobility, and high-throughput hybrid multiplay services. Importantly, the potential of Non-Terrestrial Networks has been recognized in standardization activities. In fact, a work item for 3GPP Rel-17 was approved in December 2019 to define and assess solutions related to NTNs for NR, with a specific focus on satellite access. Study items have also been designated for Rel-18 and Rel-19, indicating a commitment to long-term research within the 6G timeframe [9].

1.3.2 NTN architecture

Non-terrestrial network architecture features: a terrestrial terminal, an aerial/space station, a service link between the terrestrial terminal and the aerial/space station, and a gateway that connects the non-terrestrial access network to the core network through a feeder link [9]. The general architecture of an NTN is depicted in Fig. 1-7. As shown, different types of stations can be used:

Unmanned Aerial Vehicles (UAVs), flying at low altitudes (e.g., a few hundred meters), have garnered growing interest due to their flexibility. They are increasingly recognized for their ability to offer broadband, wide-scale wireless connectivity in disaster or temporary events and to serve as relays for terrestrial mobile nodes. On one hand, UAVs can be deployed as needed, enhancing energy efficiency compared to constantly active fixed terrestrial infrastructures. On the other hand, they face challenges related to high propulsion energy consumption required to sustain their movement, leading to significant power management constraints.

High Altitude Platform (HAP), operating within the stratosphere at approximately 20 km altitude, HAPs are currently under consideration for their rapid deployment and extensive geographical coverage spanning hundreds of kilometers. These elements are being explored as a means to facilitate highly flexible deployment and provide cost-effective wireless services, eliminating the prohibitive costs associated with terrestrial infrastructures. Nonetheless, challenges for HAPs may arise due to the requirement for refueling and issues related to maintaining stability in the air.

Satellites can be categorized based on their orbit characteristics. Geostationary Earth Orbit (GEO) satellites, positioned at an altitude of approximately 35,800 km on the Earth's equatorial plane, provide expansive coverage over large geographical areas. Despite the significant signal propagation delay and attenuation experienced at such distances, GEO satellites remain continuously visible from terrestrial terminals. In contrast, Low Earth Orbit (LEO) and Medium Earth Orbit (MEO) satellites orbit at altitudes ranging from 200 to 2,000 km and 2,000 to 35,000 km, respectively. These satellites offer improved signal strength and lower propagation delay compared to

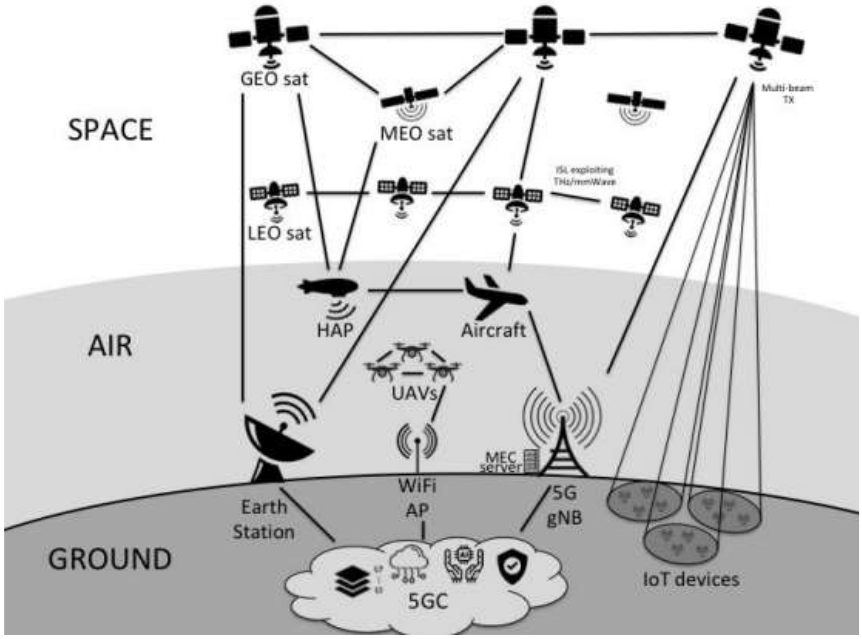

Figure 1-7 NTN architecture [10] .

GEO systems. However, they are non-stationary relative to the Earth's surface and need to operate in constellations to maintain continuous service.

Based on the integration level between the aerial/spaceborne elements three different NTN architecture have been proposed by 3GPP [9]:

1. a *transparent* satellite-based Radio Access Network (RAN) architecture in which the satellite repeats the user's signal from the feeder link to the service link and vice versa.
2. a *regenerative* satellite-based RAN architecture in which the satellite payload implements regeneration of the signals received from the Earth, while also providing intersatellite connectivity.
3. a *multi-connectivity* architecture involving two transparent RANs (either GEO or LEO or a combination thereof), where integration of terrestrial and non-terrestrial access is also supported.

1.3.3 NTN use cases

For an extended period, non-terrestrial devices have been contemplated for supporting services such as home delivery, meteorology, video surveillance, television

broadcasting, remote sensing, and navigation. Nevertheless, recent technological advancements in the aerial and space industry have paved the way for the integration of terrestrial and non-terrestrial technologies, enabling the realization of more sophisticated use cases. Some examples of advanced NTN use cases are reported in Fig. 1-8, including:

Communication Resilience and Service Continuity: non-terrestrial stations offer diverse capabilities for enhancing communication resilience and ensuring service continuity. These elements can be strategically deployed to support existing base stations, delivering high-capacity wireless coverage in scenarios such as hot-spot areas or during terrestrial infrastructure overload. In instances where the primary communication path is compromised, non-terrestrial elements can serve as a secondary backup route. This is particularly valuable in scenarios like rural areas, oceans, or post-natural disasters when terrestrial towers may be out of service. Furthermore, these elements can provide on-demand additional capacity to cell-edge users, promoting fairness within the network. Aerial platforms equipped with Mobile Edge Cloud (MEC) functionalities contribute to coverage evolution by offering additional computing and storage capabilities on the ground, ushering in a three-dimensional aspect. Despite potential energy challenges in the MEC environment, ongoing studies explore machine-learning-assisted migration and renewable energy technologies to minimize power consumption.

Global Satellite Overlay: in scenarios where the distance between two terrestrial infrastructures makes inter-site connectivity through optical fiber prohibitively expensive, a satellite constellation becomes a viable solution. These satellites, interconnected through inter-satellite links, form a mesh network, providing high-capacity access connectivity to on-the-ground devices. This overlay space mesh network relays user signals efficiently and cost-effectively, overcoming the limitations of traditional inter-site optical fiber connectivity.

*Ubiquitous Internet of Things (IoT) Broadcasting: a*erial and space platforms, owing to their wide geographical coverage and inherent broadcast nature, enable the widespread distribution of multimedia and entertainment content. This capability extends to in-motion terminals, such as planes or vessels, which may not benefit from

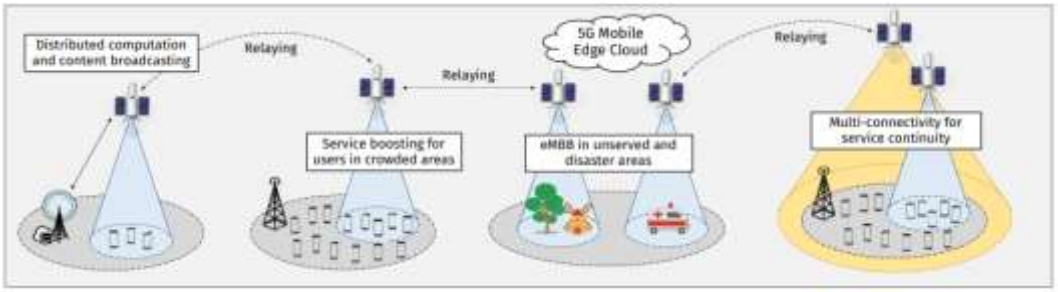

Figure 1-8 Examples of NTN use cases [8].

terrestrial coverage. UAVs and satellites also serve as moving aggregators for IoT traffic, ensuring global continuity of service for sensor-based applications.

Advanced Backhauling: non-terrestrial terminals play a crucial role in serving on-the-ground backhaul requests wirelessly, especially in locations lacking wired backhaul solutions. This approach not only conserves terrestrial resources for access traffic but also eliminates the costs associated with traditional fiber-like deployments. Satellites and other aerial platforms further complement terrestrial backhaul, particularly in densely populated regions with high peak traffic demands, facilitating load balancing.

*Energy-Efficient Hybrid Multiplay: a*ir and spaceborne platforms contribute to high-speed connectivity while emphasizing energy efficiency. Aerial platforms like UAVs, despite consuming significant energy for hovering, can be deployed on demand with smart duty cycle control mechanisms, reducing the management costs associated with constantly active terrestrial infrastructures. Additionally, space platforms like satellites leverage solar panels to operate efficiently, providing clean and renewable energy compared to traditional sources powering terrestrial devices.

1.3.4 Key Enabling Technologies for NTN

Recent technological advancements in the aerial/space industry will play a crucial role in the evolution of Non-Terrestrial Networks. Enabling technologies for non-terrestrial networks are:

*Architecture advancements: s*pace manufacturers are enhancing satellite technologies, reducing operational costs, and improving efficiency. Emerging innovations, such as nano- and pico-satellites in Low Earth Orbit (LEO), boast reduced component costs,

low communication latency, and energy efficiency. Gallium Nitride (GaN) technologies on satellites offer smaller form factors, efficient components, and potential adoption in 6G. Multi-layered satellite networks, including LEO and GEO constellations, promise improved spatial/temporal coverage. However, true integration between terrestrial and non-terrestrial networks seems distant, with standardization activities scheduled for 6G. UAV technology advancements, particularly with solid-state lithium batteries, enable longer operational durations. UAV swarms, combined with High Altitude Platforms (HAPs) and satellites, enhance information broadcasting through redundancy against single points of failure. Architecture optimization benefits from the transition to Software Defined Networking (SDN), contributing to a disaggregated architecture in 6G. This design enhances flexibility, automation, and agility in service delivery to terrestrial terminals. Satellite payloads can be adapted in software, allowing flexible adjustments to beam patterns, frequency, and power allocation. Hybrid payload implementations, distributing signal processing between on-the-ground gateways and non-terrestrial stations, are studied for improved trade-offs.

Higher-Layer advancements: NTNs present challenges compared to standalone terrestrial systems, impacting standard transmission protocols like TCP. Network operators develop acceleration techniques for better transport protocol performance. TCP spoofing and multiplexing are employed to enhance TCP performance in non-terrestrial connections, aiming to quickly reach the maximum supported rate.

Frequency bands and spectrum allocation: non-terrestrial devices traditionally operate below 6 GHz, but high-frequency communications in the mmWave and optical bands offer potential for ultra-fast connections. Satellite communications in the Ku-band and Ka-band represent pivotal components of the modern communication landscape. The Ku-band, operating in the frequency range of 12–18 GHz, is extensively utilized for both upstream and downstream communication. Widely employed for satellite television broadcasting, Very Small Aperture Terminal (VSAT) systems, and broadband data transmission, the Ku-band strikes a balance between atmospheric absorption and the size of ground station equipment. On the other hand, the Ka-band, spanning from 26.5 to 40 GHz, offers higher bandwidth potential, making it well-

Table 1-1 Enabling technologies for NTNs [9].

	Technology	Advantage
Architecture	Nano/pico satellites	Small component costs, low latency, low energy consumption
	Gallium Nitride (GaN)	Feasible to install, small form-factor and more efficient components
	Multi-layered networks	Better spatial and temporal coverage by deploying satellites in different orbits
	Solid-state lithium batteries	Safe and efficient source of power
	Software Defined Networking (SDN)	Improved flexibility, automation, agility through Virtualization Network Functions (VNFs)
	Flexible payloads	Dynamic adaptation of beam patterns, frequency, and power allocation
	Hybrid payloads	Better trade-off between performance and payload complexity
Spectrum	Millimeter waves	Feasibility of ultra-fast connections, antenna gain, spatial isolation and security
	UWB modulation	Reduced non-linear signal distortion by encoding the transmitted pulse
	Cognitive spectrum	Reduced interference through dynamic spectrum utilization in different frequency bands
	Optical communications	Feasibility of terabits-per-second connections through extreme bandwidth and directivity
Antenna	Reconfigurable phased antennas	Reduced power consumption, size and weight
	Metasurface antennas	Component miniaturization, high directivity, low sidelobes, fine beamwidth control
	Inflatable/fractal antennas	High-directivity in dynamic scenarios
	Coherent antenna arrays	Maintainability, scalability, flexibility, robustness to single points of failure
	Multi-beam architectures	High spectrum efficiency through spatial diversity
Higher layers	TCP spoofing	Fast TCP full-buffer capacity through TCP acknowledgements
	TCP multiplexing	High performance by splitting TCP session into multiple data flows

suited for high-throughput satellite (HTS) systems and broadband satellite services. Despite its susceptibility to atmospheric absorption, particularly during heavy rain, the Ka-band is gaining prominence for its ability to support increased data throughput. Both Ku-band and Ka-band satellite communications play vital roles in delivering diverse services, from entertainment broadcasting to broadband internet connectivity, contributing to the evolution of global communication networks. Solutions are proposed for mmWave adoption challenges, including impulse-based ultra-wideband (UWB) modulation to reduce non-linear signal distortion. Cognitive spectrum techniques enable dynamic spectrum utilization while minimizing interference. Optical wireless technology in the feeder link achieves terabit-per-second aggregate capacity with advantages in bandwidth, directivity, power consumption, and mass. Despite the potential, optical solutions are not yet included in NTN standards, targeting beyond-5G use cases.

New antenna technologies: aerial/space devices benefit from reconfigurable antennas with electronic beam-steering, reducing power consumption and size. Programmable environments, enabled by metasurfaces and intelligent structures, contribute to antenna component miniaturization and improved performance. Future trends suggest the use of inflatable and fractal antennas for high directivity. UAVs and/or nano-satellites in swarms create distributed coherent antenna arrays, offering maintainability, scalability, and robustness. Advanced antenna solutions support multi-beam architectures for spatial diversity, particularly favored in mmWave and

optical domains. A more in-depth exploration of various antenna technologies better suited for Non-Terrestrial Networks (NTNs) will be presented in detail in the upcoming second chapter. A summary of the key enabling technologies for NTNs is reported in Table 1-1.

1.3.5 Open challenges in NTN

While ongoing efforts are directed at standardizing Non-Terrestrial Networks, several unresolved issues in protocol design necessitate long-term research, Table 1-2, [9].

Channel modeling remains a significant concern, despite the 3GPP's specification of mmWave propagation characterization for the satellite channel. Currently, the investigation lacks the exploration of second-order statistics, including spatial and temporal correlation, and the nuanced analysis of Doppler, fading, and multipath components—crucial aspects, particularly at high frequencies. Additionally, a comprehensive and accurate model of a fully-layered space-air-ground channel is still absent.

Consideration must be given to spectrum co-existence as non-terrestrial systems venture into mmWave bands, which have been occupied by other systems, such as satellites providing weather forecasting services, for many years. The primary challenge lies in the development of flexible spectrum-sharing techniques. These techniques must strike a balance by maintaining sufficient isolation among different communications to ensure reliable operation, all while keeping licensing costs reasonable.

In the realm of non-terrestrial communication, compensating for the substantial Doppler effect, induced by the high speed of aerial/space stations, poses a challenge even with the highest available sub-carrier spacing in the frame structure. The extensive propagation delays characteristic of Non-Terrestrial Networks (NTNs) further exacerbate the situation, leading to an increased response time for the Adaptive Modulation and Coding (AMC) scheme loop. This necessitates a margin to account for potential outdated control signals exchanged during channel estimation. Notably, within an integrated terrestrial/non-terrestrial framework, diverse network elements

Table 1-2 Open challenges for NTNs [9].

Open challenge	Explanation
Channel Modeling	Missing adequate characterization of mmWave second order statistics, Doppler, fading, multipath
Spectrum co-existence	Spectrum sharing is required to provide isolation among different non-terrestrial services
PHY procedures	Design of flexible numerology to compensate for large Doppler shift Non-linear payload distortions may complicate signal reception Large RTTs increase the response time for ACM scheme Large RTTs make it infeasible to operate in TDD
HARQ	Large RTTs may exceed the maximum possible number of HARQ processes
Synchronization	Large non-terrestrial station's footprint creates a differential propagation delay among users in the cell
Initial access	Channel dynamics may result in obsolete channel estimates
Mobility management	Directionality complicates user tracking, handover, and radio link failure recovery
Constellation management	Non-terrestrial stations may need to serve a very large number of users Constellation of non-terrestrial stations is necessary to maintain ubiquitous service continuity High cost of satellite launches complicates deployment of dense constellations Wireless coordination among air/spaceborne vehicles complicates constellation management
Higher-layer design	Channel dynamics result in obsolete topology information Large RTTs result in longer duration of the slow start phase of TCP Channel dynamics result in decreased resource utilization due to sudden drops in the link quality
Architecture technologies	Unclear where to distribute SDN planes Long RTTs prevent long duration of batteries Design of central authority making secure network/communication decisions

along the end-to-end communication path may process information at varying rates, contributing to an overall communication delay. Furthermore, the feasibility of employing Time Division Duplexing (TDD), a common practice in terrestrial networks, becomes questionable in non-terrestrial networks due to the necessity for guard times that are proportional to the propagation delay.

Exceeding the maximum allowable number of Hybrid Automatic Repeat reQuest (HARQ) processes, a typical feature in 5G NR systems, becomes a challenge in non-terrestrial networks with their prolonged round trip time (RTT). Addressing this issue by merely increasing the number of processes proves unfeasible due to memory constraints on the mobile terminal's end. The extensive RTTs also necessitate sizable transmission buffers, potentially imposing restrictions on the number of retransmissions permitted for each transmission.

Synchronization issues arise in non-terrestrial systems, characterized by their high mobility and larger cell sizes in comparison to terrestrial networks. Particularly at low elevation angles, a substantial differential propagation delay may emerge between users at the cell edge and those at the center, reaching up to 10 ms for GEO satellites.

In non-terrestrial applications, where the channel may exhibit rapid variations over time, initial access becomes a challenging process. On-the-ground terminals initiate a physical connection with a non-terrestrial station by detecting synchronization signals. The challenge lies in the fact that the channel's quick variations can render the initial estimate obsolete swiftly. Additionally, in space-ground integrated networks, each intermediate node often associates with a gateway based on its individual benefit, overlooking potential disadvantages that may impact the overall network performance.

In the non-terrestrial domain, where high-capacity connections at mmWaves demand directionality for sufficient link budget, mobility management presents significant challenges. Achieving fine alignment of beams is crucial in this scenario, impacting the design of control operations such as user tracking, handover, and radio link failure recovery. These challenges become even more critical due to the very high speed of aerial/space platforms, which could lead to the loss of beam alignment before completing a data exchange. The increased Doppler effect at high speed adds complexity, potentially making the channel non-reciprocal and impairing feedback over a broadcast channel.

Constellation management faces challenges in non-terrestrial scenarios where a station's larger footprint is required to serve numerous on-the-ground terminals, potentially leading to bandwidth saturation with implications for latency and throughput performance. The rapid movement of air/spaceborne vehicles relative to the Earth's surface may create coverage gaps, necessitating a constellation to ensure continuous service. However, configuring multiple satellites moving in different orbits for integrated operation introduces complexities such as handovers and load balancing among the layers. Additionally, unlike the terrestrial scenario where coordination between base stations is facilitated through fiber connections or a central entity, non-terrestrial air/spaceborne stations must implement wireless coordination, further complicating constellation management.

In non-terrestrial networks, higher-layer design encounters challenges with current network/transport protocols exhibiting suboptimal performance. The unpredictable mobility, such as in UAV swarms, leads to rapid obsolescence of topology information, necessitating constant refreshing and thereby increasing communication

overhead. Additionally, a substantial Round Trip Time (RTT) prolongs the slow start phase of TCP, delaying the sender's reach to full bandwidth. Common occurrences of sudden drops in link quality within NTNs prompt the sender to reduce transmission rate, causing a drastic decrease in resource utilization. Furthermore, in the context of a multi-layered integrated network, the support for different (and occasionally conflicting) communication protocols by various network devices complicates network management.

NTNs' architecture technologies present challenges in determining the optimal distribution of Software-Defined Networking (SDN) planes for effective service delivery. Factors influencing this decision include processing capabilities and achievable transmission rates. Additionally, due to the significant distances involved and resulting severe path loss, transmit power needs to be set close to the saturation point, potentially impacting battery duration—critical in scenarios where aerial devices support IoT applications. Lastly, an integrated space-air-ground architecture must incorporate a trusted central authority to ensure secure network topology and communication decisions, preventing the selection of malicious nodes as gateways.

1.4 SPACE SEGMENT IN NTN

1.4.1 Introduction to satellite communications

In the USA and Europe, around 20% and 28% of the population, respectively, resides in rural areas. Globally, this figure increases to 40%. Fiber deployment often does not reach rural areas, particularly the last mile, due to the high cost for network operators, which is challenging to justify in terms of Average Revenue per User (ARPU). The estimated cost for every meter of fiber connectivity is approximately $100, with the majority of expenses attributed to digging, trenching, and general civil works [10]. In situations where fiber is impractical, such as deep rural, seaside, desert, mountains, etc., satellites emerge as a viable solution for providing broadband connectivity. In recent years, there has been a race within the research community to deploy various satellite constellations catering to both rural and remote areas. The reduction in satellite launch costs, approximately a few thousand USD per kg of mass for SpaceX Falcon 9 [11], has contributed to the increase in the number of the satellites orbiting

the Earth. Currently, there are more than 9.200 satellites in orbit, comprising 8.300 in Low Earth Orbit (LEO), 200 in Medium Earth Orbit (MEO), and 550 in Geostationary Orbit (GEO). This number is projected to grow to 50,000 within the next decade.

While GEO and MEO constellations experience high two-way delays in the order of several hundred milliseconds, leading to performance degradation of TCP protocols, LEO constellations can significantly reduce these delays to a few tens of milliseconds. High-Altitude Platforms (HAPs) at a distance of 20 km can further reduce Round-Trip Times (RTTs) to a few milliseconds. It's important to note that light travels approximately 300,000 km/s through the air, which is 50% faster than the 200,000 km/s over silica fiber. This translates into a propagation delay of 3.33 μs/km for free-space communications and 5 μs/km for fiber transmission. Some argue that satellite communications can be faster than fiber in wide area scenarios beyond 1,000 km [12], [13], especially in challenging terrains for fiber deployment, such as deserts and mountains.

Several companies have concentrated on deploying Low Earth Orbit (LEO) satellite constellations (ranging from 500 to 1200 km altitude) as the latency in these cases is moderate, typically within few tens of milliseconds. Apart from offering coverage to rural areas, satellites can provide worldwide connectivity and are highly resilient to natural disasters and wars. LEO satellite constellations can sufficiently support Machine-Type Communications (MTC) and Mobile Broadband (MBB) in remote areas, paving the way for Non-Terrestrial Networks (NTN) complementing existing Terrestrial Networks, both fixed and mobile. The integration of LEO constellations in the 5G and even 6G ecosystems is explored in [14], [15], with an in-depth survey provided in [16]. Currently, four major companies—Telesat, Tesla's Starlink, OneWeb, and Amazon Kuiper—are actively deploying LEO satellite mega-constellations. A comprehensive comparison of these constellations and the features provided by these companies is presented in [17], demonstrating latency in the tens of milliseconds and average throughput on the order of Gb/s per satellite.

1.4.2 Throughput

In satellite communications the throughput is highly influenced by the altitude of the space-borne entity as it is correlated with the round-trip time. Latency plays a significant role in affecting TCP throughput within TCP/IP-based networks. TCP throughput can be estimated by the Mathis formula [18]:

$$Throughput_{TCP} = \frac{MSS}{RTT}\frac{C}{\sqrt{p_{loss}}} \quad (1.1)$$

where *RTT* is the end-to-end Round-Trip Time, *MSS* is the Maximum Segment Size, *C* is a constant (usually is between 1 and 1.5), and p_{loss} is the packet loss probability.

Satellites stationed in Geostationary Earth Orbit (GEO) are positioned at an altitude of 35,876 km. GEO configurations typically feature Very High Throughput Satellites (VHTS), offering substantial capacity ranging from tens to hundreds of gigabits per second. In such scenarios, Doppler effects are minimal, but there can be notable propagation delays, especially in the case of transparent satellites, reaching several hundreds of milliseconds.

Satellites in Non-Geostationary Orbits (NGSO), specifically Medium Earth Orbit (MEO) ranging from 7,000 to 25,000 km or Low Earth Orbit (LEO) within 300 to 2,000 km, exhibit relative motion to the Earth. In such instances, latency values may fall within the moderate range, typically in the tens of milliseconds, but compensating for Doppler effects becomes necessary. Satellite coverage and their cells can either be stationary or exhibit motion. In the former, beams are fixed on Earth, while in the latter, beams move at a speed consistent with the satellites (typically a few km/s for LEO sats). For non-stationary cells, methods for handover operations and roaming become essential.

1.4.3 Frequency spectrum

The frequency bands allocated by ITU for satellite communications span from the L to the Q/V band, Table 1-3. The L and S bands, typically offering limited bandwidth ranging from tens to hundreds of KHz to a few MHz, are often designated for IoT

applications with low bandwidth requirements. In contrast, the Ka and Ku bands provide significantly more bandwidth, in the range of tens or hundreds of MHz, enabling Mobile Broadband (MBB) connectivity comparable to DSL connections (e.g., around 20 Mb/s) and, in some cases, akin to fiber-to-the-home (100 Mb/s and above), particularly in scenarios with high antenna gains. Moving further, the Q/V bands offer even larger bandwidth capacities (ranging from hundreds of MHz to a few GHz), albeit they are more susceptible to atmospheric losses and absorption from rain. Some satellite companies are exploring the V band for inter-satellite links (ISL) due to its location above the clouds, facilitating mesh connectivity between satellites. Additionally, experimental scenarios consider the W Band (between 75-110 GHz), offering even more bandwidth than the Q and V bands, suitable for ISL applications despite facing challenges like propagation impairments and rain fade.

1.4.4 Link-budget and bitrate

Traditional link budget calculations in satellite communications adhere to Friis propagation model, wherein the power at the receiver antenna (Pr) is determined as follows:

$$P_r = P_t \frac{G_t G_r \lambda^2}{(4\pi)^2 d^2} \tag{1.2}$$

where P_t is the transmitted power, G_t and G_r are the gain of the transmitting and receiving antenna, λ is the transmission wavelength, and d is the slant range between the transmitter and receiver in the satellite link.
The noise at the receiver antenna is:

$$N = k_B T B_w \tag{1.3}$$

where k_B is the Boltzmann constant, T is the noise temperature and B_w is the bandwidth of the receiving filter.

Table 1-3 Frequency bands for satellite communications [18].

Sat Band	Downlink (DL)	Uplink (UL)
L band (GEO)	1518 – 1559 MHz	1626.5 – 1660.5 MHz 1668 – 1675 MHz
L band (Non-GEO)	1613.8 – 1626.5 MHz	1610.0 – 1626.5 MHz
C band	3400 - 4200 MHz 4500 - 4800 MHz	5725 - 7025 MHz
S Band	2160 -2200 MHz 2483.5 - 2500 MHz	1980 - 2025 MHz
Ku band	10.7 - 12.75 GHz	12.75 - 13.25 GHz 13.75 - 14.5 GHz
Ka band (GEO)	17.3 – 20.2 GHz	27.0 – 30.0 GHz
Ka band (Non-GEO)	17.7 – 20.2 GHz	27.0 – 29.1 GHz 29.5 – 30.0 GHz
Q/V band	37.5 – 42.5 GHz 47.5 - 47.9 GHz 48.2 - 48.54 GHz 49.44 - 50.2 GHz	42.5 – 43.5 GHz, 47.2 – 50.2 GHz 50.4 – 51.4 GHz

The signal-to-noise ratio (SNR) can be computed as follows [19]:

$$\begin{aligned} SNR = {} & EIRP(dBW) \\ & + \frac{G_r}{T}\left(\frac{dBi}{K}\right) \\ & - FSPL(dB) \\ & - AtmLoss(dB) \\ & - AdLoss(dB) \\ & - B_w(dBHz) \\ & - k_B\left(\frac{\frac{dBW}{K}}{Hz}\right) \end{aligned} \tag{1.4}$$

where the *EIRP* is the Effective Isotropic Radiated Power and it corresponds to the product $G_t P_t$, *FSPL* is the Free Space Patch Loss. The atmospheric and additional losses, $AtmLoss$ and $AdLoss$, take into account the attenuation resulting from the absorption of various molecules in the atmosphere, predominantly oxygen and water.

Rain fade and availability, factors not considered in equation (1.4), encompass the attenuation due to passing through clouds, rain, etc., potentially lowering link availability to below 99%. Typically, link budget calculations consider clean sky assumptions (i.e. null attenuation due to rain and fading), but a margin value between 2 and 10 dB is often recommended to compensate from rain fading and other unexpected sources of power loss and attenuation.

After determining a specific Signal-to-Noise Ratio through the link-budget analysis, combining this value with the transmission bandwidth establishes an upper limit for the maximum attainable bit rate (*Rmax*), as dictated by Shannon-Hartley's theorem:

$$R_{eff} < R_{max} = B_w \cdot \log_2(1 + SNR) \tag{1.5}$$

where R_{eff} is the effective bitrate and it cannot be larger than the Shannon's limit R_{max}. The factor $\log_2(1 + SNR)$ is referred to as spectral efficiency (SE) and indicates what is the bitrate achievable with a given bandwidth. Also:

$$\beta_{eff} < \beta_{max} = \log_2(1 + SNR) \tag{1.6}$$

Typical spectral efficiency values vary from 0.5 to 2 bps/Hz, occasionally reaching up to 4 bps/Hz in certain specific scenarios. Achieving values beyond 5 bps/Hz in satellite communications is often challenging, particularly unless they are in close proximity to Earth. Usually, each satellite is provided with multiple antenna beams pointing at different regions in its footprint area allowing frequency reuse like in mobile network. Certainly, High or Very-High Throughput Satellites (HTS/VHTS) signify a progression in satellite technology, offering increased capacity through more spot beams and enhanced frequency reuse. When implemented in Low Earth Orbit (LEO) constellations, they can deliver high bandwidth and reduced latency, facilitating Mobile Broadband (MBB) and Machine-Type Communications (MTC) in areas with limitations on fiber and 5G connectivity. V/HTS satellites are characterized by the use of multiple spot beams (often tens or hundreds) covering small geographical area cells and the frequency reuse of allocated bandwidth in non-adjacent beams/cells, resulting in higher satellite throughput. Indeed, by dividing a particular region into smaller sub-

regions or cells covered by individual spot beams and employing frequency reuse, more capacity can be provided to the area. This approach allows for scalability of capacity, akin to mobile networks, where the same frequency is reused multiple times across non-adjacent cells. It is crucial to ensure that the Signal-to-Noise and Interference Ratio (SINR) remains within acceptable limits for digital communications. The total bitrate increases with the number of beams and polarizations as:

$$R_{tot} = \beta B_w \left(\frac{N_p N_b}{N_c}\right) \cdot \left(1 - \eta_{guard}\right) \tag{1.7}$$

where N_p is the number of polarizations (1 or 2), N_b is the number of spot beams, N_c is the number of colors or frequencies, and η_{guard} is the guard-band between sub-bands (typically between 5 and 10%). However, it's important to note that utilizing multiple spot beams onboard significantly increases the size and weight of the satellite. Moreover, when employing multiple beams, each individual beam may cause interference with adjacent ones in the operating frequency. By combining the noise and the interference it is possible to determine the Signal to Interference and Noise Ratio (SINR):

$$SINR = \frac{1}{\frac{1}{SNR} + \frac{1}{SIR}} \tag{1.8}$$

This means that the satellite antenna must be designed with high directivity to effectively illuminate a specific cell, ensuring that sidelobes in neighbouring cells are significantly lower. Chapter two will provide a thorough examination of antenna specifications and various technologies applicable to satellite communications.

Chapter 2: Antenna technologies for satellite communications

2.1 SPECIFICATIONS AND CHALLENGES

Antennas used in satellite communications face different challenges and specifications based on whether the satellite is in Geostationary Earth Orbit (GEO), Medium Earth Orbit (MEO), or Low Earth Orbit (LEO).

Geostationary Earth Orbit satellite:

- *Fixed pointing:* GEO satellites orbit at an altitude that allows them to remain stationary relative to a specific point on Earth's surface. Antennas on both the satellite and the ground station must maintain a fixed pointing configuration for effective communication. This simplifies the tracking requirements compared to satellites in other orbits.
- *High directivity:* antennas on GEO satellites need high directivity to cover a specific footprint on the Earth's surface efficiently.
- *Coverage footprint design:* antennas need to be designed to cover a specific geographic area on the Earth's surface. The beam shape and coverage footprint are critical considerations in ensuring seamless communication within the designated service area.
- *Mitigation of atmospheric effects:* atmospheric conditions can affect the propagation of signals. Therefore, antenna designs for GEO satellites must incorporate methods to mitigate the impact of atmospheric effects, including phenomena like rain fade, clouds, absorption, etc., ensuring optimal signal quality and reliability.

Medium Earth Orbit satellite:

- *Tracking and handover strategies:* since MEO satellites are not stationary in the sky, antennas must implement robust tracking mechanisms. Efficient handover strategies become crucial for seamless transitions between different satellites or cells within a satellite constellation.

- *Coverage Footprint Optimization:* MEO satellites have a larger coverage footprint compared to Low Earth Orbit (LEO). Antennas must employ beamforming and beam-steering techniques to optimize coverage while maintaining signal strength and link quality.
- *Interference Mitigation and Frequency Reuse:* in MEO constellations with multiple satellites, antennas must address interference challenges. Efficient frequency reuse strategies in non-adjacent cells are essential for maximizing throughput and maintaining signal quality.

Low Earth Orbit satellite:

- *Rapid movement and tracking:* LEO satellites orbit the Earth at lower altitudes, resulting in higher orbital speeds and frequent movements across the sky. Antennas for LEO satellites must be capable of rapid and precise tracking to maintain a reliable communication link, which is not as critical for slower-moving GEO satellites.
- *Doppler shift management:* the fast movement of LEO satellites induces significant Doppler shifts in the transmitted signals. Antennas need advanced tracking and compensation mechanisms to handle these frequency changes and maintain proper signal alignment.
- *Short communication windows:* LEO satellites have shorter visibility windows from a specific ground station compared to GEO satellites. Antennas must efficiently utilize these brief communication opportunities to transmit and receive data effectively.
- *Frequent handovers:* as LEO satellites traverse the sky quickly, users or ground stations may experience more frequent handovers between satellites or cells within a satellite constellation. Antennas must seamlessly manage these handovers to ensure continuous connectivity without disruptions.
- *Variable coverage footprint:* LEO satellites exhibit a changing coverage footprint due to their orbital dynamics. Antennas need to adapt to varying coverage areas and implement dynamic beamforming to maintain consistent signal strength across different locations on Earth.

- *Interference and frequency reuse:* in dense LEO satellite constellations, the proximity of satellites increases the potential for interference. Antennas must employ effective interference mitigation strategies and optimize frequency reuse to manage co-channel interference.

Table 2-1 presents the key parameters of currently operational LEO constellations, including Telesat, OneWeb, Starlink, and Kuiper, all of which operate in the Ku-Ka bands.

Table 2-1 Key parameters of Telesat, OneWeb, Starlink, and Kuipers constellations [21].

	Telesat	**OneWeb**	**Starlink**	**Kuiper**
Number of satellites (first phase full constellation)	298 (1,671)	716 (6,372)	1,584 (4,408)	578 (3,236)
Altitude	1,015–1,325 km	1,200 km	550–570 km	590–630 km
User link frequencies	Up: 27.5–30 GHz Down: 17.8–20.1 GHz	Up: 12.75–14.5 GHz Down: 10.7–12.7 GHz	Up: 14–14.5 GHz Down: 10.7–12.7 GHz	Up: 28.35–30 GHz Down: 17.7–20.1 GHz
		Downlink		
	Telesat	OneWeb	Starlink	Kuiper
Number of user beams	≥16	16	≥16	≥16
Channel bandwidth	<400 MHz	250 MHz	250 MHz	100 MHz
Maximum antenna gain	38 dB	N/A	37.1 dB	39 dB
Maximum EIRP	39 dBW	34.6 dBW	32.71 dBW	43.1 dBW
		Uplink		
	Telesat	OneWeb	Starlink	Kuiper
Channel bandwidth	<400 MHz	125 MHz	125 MHz	50 MHz
Maximum antenna gain	37.1 dB	N/A	37.1 dB	39 dB
Maximum G/T	13.2 dB/K	−1 dB/K	9.8 dB/K	–

EIRP: effective isotropic radiated power; dBW: decibel watt; G/T: antenna gain-to-noise-temperature.

Addressing shared challenges in GEO, MEO, and LEO satellite communications encompasses considerations related to atmospheric effects, power consumption, and physical dimensions. Antennas face the task of navigating atmospheric conditions that impact signal propagation, particularly in higher-frequency bands. Meanwhile, the power constraints inherent in satellites, especially smaller ones with limited power resources, necessitate efficient antenna operation within these limitations. To meet payload constraints, antennas must be meticulously designed to be lightweight and compact. These challenges and specifications vary based on the orbit type and specific mission requirements of the satellite communication system.

2.2 BEAM SCANNING ANTENNAS

Beam scanning antennas play a pivotal role in satellite communication systems, offering a dynamic and versatile solution to address the challenges of communicating with satellites in various orbits and changing conditions. Unlike fixed antennas, beam scanning antennas can adjust the direction of the antenna beam, allowing for precise targeting of satellites, efficient beamforming, and adaptation to different geographic locations. This capability is particularly valuable in non-terrestrial networks where satellites in low Earth orbit (LEO) or other orbits may necessitate frequent adjustments to maintain optimal communication links. The importance of beam scanning antennas lies in their capacity to enhance the agility and responsiveness of satellite communication systems, ensuring reliable connectivity, minimizing signal disruptions, and accommodating the diverse and dynamic nature of satellite networks. The versatility of beam scanning technology contributes significantly to the overall efficiency and effectiveness of satellite communication, making it an indispensable component in modern satellite systems. Beam scanning antennas can be classified in two very broad categories: mechanically scanned antennas and electronically scanned antennas.

2.2.1 Mechanical beam scanning

Mechanically scanned antennas offer an expanded angular coverage and demonstrate exceptional performance in terms of polarization purity, operational bandwidth, and the antenna gain-to-noise-temperature (G/T) ratio. Mechanically scanned antennas can be classified into four main classes: gimbals-based, allowing full 2D mechanical pointing, hybrid systems, moving feeds, and rotatable surfaces [20].

Full 2D Pointing antennas

Achieving full 2D pointing necessitates intricate mechanical gimbals. Many existing solutions adhere to conventional concepts, particularly reflector antennas [21], [22]. These antennas typically exhibit substantial size and weight, often mandating a gimbal equipped with at least two servomotors to manage both the pointing direction of the radiated beam and its polarization. Over time, efforts have been made to streamline the profile of mechanically steered antennas for enhanced integration into mobile platforms like airplanes. Waveguide-based arrays [23] have emerged as alternatives due to their reduced profile and improved efficiency compared to reflector antennas.

However, they require complexities in pointing mechanisms, involving the coupling of azimuthal rotation with movement in elevation.

Hybrid Systems

In hybrid systems only the azimuthal rotation is achieved by mechanical rotation, this reduces the overall complexity of the system. Elevation pointing is accomplished by scanning the beam using conventional phase shifters, quasi-optical beamformers, and, in the case of lens antennas, adopting multi-feed systems and moving feeds. Recent years have seen various designs proposed for the Ku-band, integrating a planar array with phase shifters to scan the beam in one direction [24], [25]. In [26], elevation beam steering is achieved through a switched-beam architecture realized in microstrip technology, employing a Rotman lens. Planar quasi-optical beamformers, like the Rotman lens, offer the advantage of generating simultaneous independent beams, enabling a make-before-break handover between different satellites. Additionally, their design typically relies on nonresonant true-time delay structures, making them intrinsically broadband. Specifically, this implies that Transmit (Tx) and Receive (Rx) functions can be combined into the same aperture, potentially covering multiple bands. Lens-based concepts in parallel plate waveguide (PPW) technology have been introduced in the Ka-band to maintain the wideband operation of reflector-based solutions while providing wide coverage between ±50° in elevation [27]. Arrays based on a long slot fed by multimode PPWs, as proposed in [29], and [30], exhibit polarization agility. However, this comes at the expense of a complex design process, a field of view of ±45° in elevation, and a reduced bandwidth, 29–32 GHz.

Movable Feeds and Multifeed Systems

Utilizing movable feeds and multifeed systems, volumetric lenses present another category of mechanically scanned antennas suitable for Satcom communications. These lenses can achieve a wide scan range with reduced antenna dimensions compared to reflectors. They can be broadly classified into two main types: homogeneous lenses [30], with a limited scan range due to aberrations, and graded-index lenses, which offer the advantage of being aberration-free.

In recent years, there has been a suggestion to apply transformation optics concepts [31] to reduce the profile of the Luneburg lens. The scanning in this case is achieved by simply displacing the feed, albeit with the trade-off of increased scanning loss and

a reduction in scanning range. Arrays of smaller lenses, providing better efficiency than a single lens with a similar aperture, have shown promise for achieving a lower profile. Additionally, a 2D version of the Luneburg lens, implemented in Parallel Plate Waveguide (PPW) technology, can offer full azimuthal coverage with a low-profile arrangement. This 2D lens can also function as a beamforming network for a radiating aperture. Various solutions have been proposed to achieve the required effective refractive index variation in these lenses. These include machining a distribution of metal posts between PPW plates, photolithographically etching holes into one side of a standard printed circuit board ground plane and loading the parallel plates with electrically small patches printed on a grounded dielectric slab. It is crucial to note that, in all the 2D lenses the scanning is achieved by displacing the feed and implementing a multifeed system.

Rotatable Surfaces Systems

Low-profile antennas capable of full 2D scanning can be realized through the use of rotatable surfaces. Among the leading performers in the Ku- and Ka-bands within this category are the antennas designed by ThinKom. Employing Variable-Inclination Continuous Transverse Stub (VICTS) technology, ThinKom's antennas feature an array of stubs rotating around a single axis, offering a wide field of view and operational bandwidth [32], [33]. These terminals facilitate interoperability among various constellations, boasting a large field of view, from 7.5° to 90° in elevation, and highly favorable G/T performance (>12 dB/K at a 20° elevation). Unlike mechanical solutions, these antennas typically lack multiple-beam radiation and employ buffering mechanisms to swiftly control the radiated beam when switching between satellites.

Another approach to achieving 2D scanning involves rotatable graded-index lenses positioned in front of a radiating aperture. Operating on a principle akin to Risley prisms, this solution utilizes a fixed primary radiator with a broadside pencil beam illuminating two parallel planar lenses, creating a linear phase shift. These lenses can be rotated either synchronously or independently around the axis of the primary radiator to steer the beam in the upper hemisphere. This architecture is notably simpler and less bulky than the traditional azimuth/elevation positioner used for reflector antennas, maintaining a consistent profile during beam scanning. The required screens are passive and lack reconfigurable elements. The feasibility of this scanning mechanism based on rotatable metalenses was initially demonstrated in [34], using a

horn as the primary feed. Recent advancements have achieved higher aperture efficiency and reduced thickness by employing a low-profile primary radiator. The primary challenge in designing such antennas for Satcom applications lies in controlling the grating lobes during scanning, an aspect closely tied to the metalenses' design.

A similar solution involves translating lenses, where elevation steering is accomplished through lateral translation of a thin flat lens positioned a few wavelengths above a feed antenna. Azimuth steering is achieved through the rotation of the lens, or both the lens and the feed horn. Demonstrations have showcased dual-band operation and a beam steering range of up to 50° [35].

2.2.2 Electronical beam scanning

Electronic beam steering antennas prove to be the optimal choice for satellite tracking, especially when seeking reliable and agile operation. Electronic scanning offers significant advantages, particularly in the context of Satcom on-the-move systems, such as those on aircraft, where flat antennas are essential for rapid repositioning to compensate for platform motion. Fully electronic active arrays bring forth various reconfigurability features, radiation pattern shaping, wide scanning capabilities, multiple-beam generation, and power sharing among beams through distributed amplification.

Despite the extended capabilities provided by phased arrays, their high cost and complexity have historically limited widespread use in commercial systems. To address this limitation, various cost-effective electronic scanning antennas have been proposed, including tunable reflectarrays, transmitarrays, and liquid crystal-based antennas. However, the components typically used for tuning the elements, such as p-i-n and varactor diodes, microelectromechanical systems, and liquid crystals, are associated with increased dissipation losses.

Recent advancements in electronic chipsets, featuring lower cost and higher power have played a significant role in renewing interest in active array antennas. Specifically, the cost of fully active phased arrays has seen a recent decline, thanks to the progress of Si multichannel chips for Tx/Rx modules. This advancement has paved the way for the realization of commercially available Satcom phased arrays.

Beamforming approaches

The architecture od electronical beam scanning antennas is significantly influenced by the adopted beamforming technique. Numerous beamforming solutions, including fully analog [36], or digital [37], have been proposed. Additionally, various hybrid beamforming topologies, emphasizing different analog/digital partitioning approaches, have been explored like in [38]. Figure 2-1 shows a schematic view of the beamforming architectures. Analog beamformers remain prevalent in active phased array systems, manipulating signals at the radiating elements through analog circuits. The distinction between different implementations of the analog beamformer (ABF) in the system is generally made, categorizing them as radio frequency (RF), local oscillator (LO), or intermediate frequency (IF)/baseband (BB) beamforming. As phased array systems grow in complexity and scalability, integrated circuits' design becomes a critical aspect [39]. Consequently, RF beamforming architectures have become common due to their lower component count. However, the ease of the analog beamforming network, while beneficial for point-to-point communications with low hardware complexity and power consumption, poses challenges in designing multi-beam antenna systems. The coherent combination/splitting of individual signals in the RF domain hinders the reuse of building blocks across independent channels separated in space, imposing space constraints on spatial multiplexing systems. In contrast, analog IF/BB beamformers, with smaller circuit areas and relaxed routing complexity have the potential to handle higher numbers of concurrent independent beams. Nonetheless, multi-beam communication systems using IF/BB domain beamformers face challenges, such as narrower instantaneous bandwidths and the need for coherent LO distribution across subarray beamformer ICs in their design.

Contrasting with analog beamforming approaches, fully digital beamforming techniques have completely shifted beam steering functionalities into the digital back-end. This design requires a simplified RF front-end containing only an amplifier and frequency conversion stage for transmit and receive purposes. In this case each antenna element is linked to a dedicated RF chain followed by analog-digital converters, Fig. 2-1-b. The element-level digital beamformer (DBF) processing provides unparalleled flexibility in synthesizing simultaneous beams, allowing for modification, duplication, and combination of digital signals without compromising signal quality. Additionally, DBF facilitates the use of frequency-dependent amplitude tapering and phase shifting, incorporating corrections for hardware impairments through channel-level

equalization, I/Q correction, and static LO phase offsets. This approach becomes increasingly attractive for wideband multi-beam systems, avoiding the need for analog true-time delay beamformers. However, irrespective of the digital architecture, the implementation effort of the signal processing back-end escalates significantly with an increase in the number of antenna elements and the instantaneous channel bandwidth, respectively. Despite these challenges, analog beamformers are still considered a more practical solution for large-scale phased array systems across various applications from a performance and economic standpoint.

Compared to analog and digital beamformers, hybrid beam steering techniques offer a potential trade-off between system complexity and performance. Hybrid beamformers incorporate joint analog and digital processing, and their architecture depends on the

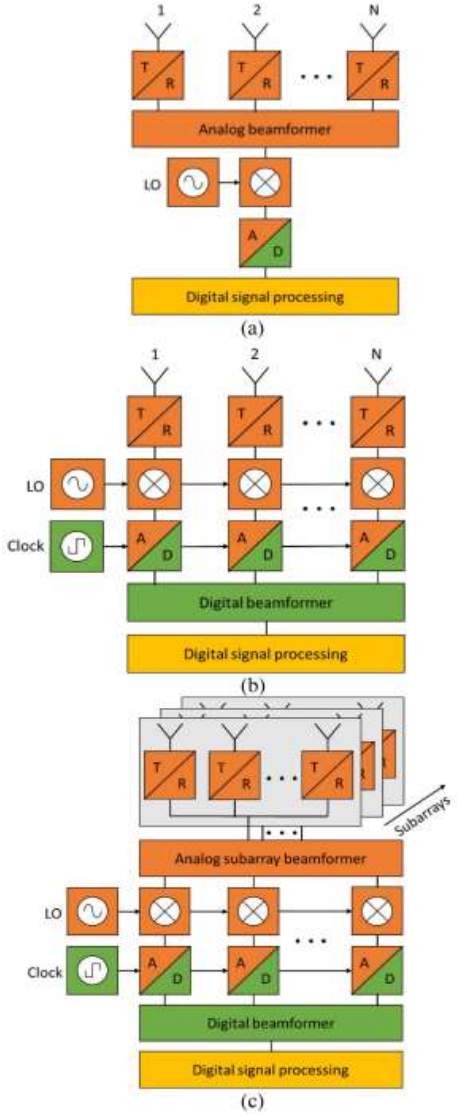

Figure 2-1 Schematic view of beamforming architecture a) analog beamforming, b) digital beamforming and, c) hybrid beamforming [40].

properties of the propagation channel. Subarray hybrid beamforming (HBF) architecture, as depicted in Fig. 2-1-c, is widely used due to its simplicity. In this topology, the antenna array is divided into subarrays, with input and output signals processed digitally, while the signals at the element level are manipulated in the analog domain. This setup allows the number of antenna elements to greatly exceed the number of RF chains, representing the maximum number of independent beams supported by the hybrid beamformer. Spatial multiplexing is achieved using the analog subarrays to synthesize overlapping sector patterns, producing a set of pencil beams in the digital signal processor. However, hybrid analog/digital beamforming architectures are not extensively deployed in multi-beam antenna systems for mobile SatCom terminals, especially those requiring both tracking and satellite-to-satellite handovers to maintain connectivity. One limiting factor is the sectorization problem of subarray HBF, restricting the angular range in which a set of simultaneous beams can be generated due to the focusing effect of the sector patterns. Although wider sector patterns can enhance the angular spread of spatial multiplexing systems, this comes at the expense of lower antenna gain and reduced suppression of grating lobes. On the other hand, fully connected HBF configurations can overcome these limitations, as each RF chain is fully connected to all available antenna elements. However, this comes with substantially higher hardware and computational complexity in return. Moreover, the fully connected HBF type achieves higher array gain, narrow beamwidth, and better spectral efficiency than the subarray HBF topology, supporting MIMO beamforming. Despite these advantages, they cannot be fully exploited in SatCom scenarios with highly decorrelated channels. The true benefits of fully connected HBFs become evident in terrestrial MU-MIMO applications, where channel capacity for spatially non-collocated users is primarily limited by the signal-to-interference noise ratio (SINR). In contrast to the SatCom sector, hybrid beamformers have been identified as a promising solution for 5G and 6G communication systems, where the overall power consumption is significantly lower compared to their fully digital counterparts.

2.3 RECONFIGURABLE ANTENNAS

2.3.1 Role of reconfigurable antennas in satellite communications

Reconfigurable antennas offer flexibility and adaptability in order to meet the dynamic requirements of various communication scenarios. Here are some aspects of their use in satellite communications:

Adaptive beamforming: reconfigurable antennas enable adaptive beamforming, allowing satellites to dynamically adjust the directionality of their antenna beams. This is particularly beneficial for tracking user terminals, managing interference, and optimizing signal strength. In [40] micro-electromechanical systems (MEMS) switches have been used to realize the radiation pattern reconfiguration of microstrip antenna, which works in Ka-band.

Frequency reconfigurability: satellites often need to operate in different frequency bands to accommodate various communication services. Reconfigurable antennas with frequency-tuning capabilities provide the flexibility to switch between frequency ranges, ensuring compatibility with diverse communication standards. In [41] a frequency reconfigurable antenna for satellite application in S and L band has been proposed.

Polarization control: satellite signals may experience changes in polarization due to atmospheric conditions or other factors. Reconfigurable antennas that can adjust their polarization state help maintain a stable and reliable link by adapting to varying polarization requirements.

Mitigating signal interference: reconfigurable antennas contribute to interference mitigation strategies. By dynamically modifying beam directions and properties, satellites can minimize interference from other satellites or terrestrial sources, improving overall communication quality.

Multi-Mode communication: reconfigurable antennas support multi-mode communication, allowing satellites to switch between different communication protocols or standards. This capability is valuable for accommodating diverse user terminals with varying communication requirements.

Power efficiency: power efficiency is crucial for satellite operations. Reconfigurable antennas can optimize their performance based on the communication needs, leading to more efficient power consumption and extended satellite mission lifetimes.

Inter-Satellite communication: in constellations, where satellites communicate with each other for relay or coordination purposes, reconfigurable antennas aid in establishing and maintaining reliable inter-satellite links. This is vital for data exchange, synchronization, and network management.

2.3.2 Classification of reconfigurable antennas

Classified based on dynamically adjustable operational properties, such as frequency of operation, radiation pattern, polarization, or a combination thereof, reconfigurable antennas can be categorized as follows:

Frequency Reconfigurable Antennas: these antennas employ two mechanisms—electrical and mechanical—for frequency adjustment. The electrical mechanism utilizes discrete tuning through radio frequency switches and continuous tuning via varactor diodes. The mechanical mechanism involves the use of impedance-loading tunable materials like liquid crystals or metasurfaces to achieve frequency reconfiguration.

Pattern Reconfigurable Antennas: utilizing movable or rotatable structures such as metasurfaces or incorporating switchable reactively loaded capacitive elements, these antennas intentionally modify the spherical distribution of the radiation pattern.

Polarization Reconfigurable Antennas: these antennas achieve reconfiguration by switching between different polarizations, such as linear polarization to left-hand circular polarization (LHCP) and right-hand circular polarization (RHCP), employing multi-mode structures or metasurfaces. To mitigate polarization mismatch and losses in portable devices, these antennas necessitate switching between horizontal, vertical, and circular polarizations.

Compound Reconfigurable Antennas: these antennas achieve simultaneous tuning of multiple parameters, such as frequency and radiation pattern, enabling independent reconfiguration of operating frequency, radiation pattern, and polarization. This is typically achieved through a parasitic pixel layer.

2.3.3 Reconfigurable antennas technologies

The different reconfiguration types can be achieved through different technologies and techniques, as illustrated in Fig. 2-2. There are four main categories of reconfiguration techniques: electrical, optical, mechanical, and material [42].

Electrical reconfiguration techniques involve utilizing switches to connect or disconnect antenna components and redistributing currents to modify the radiated fields of the antenna's effective aperture. Integrated technologies such as radio-frequency microelectromechanical systems (RF-MEMS), PIN diodes, varactor diodes, or field-effect transistors (FETs) are employed to redirect the antennas currents. RF-MEMS switch-based antennas achieve reconfiguration through the mechanical movement of the switches. While RF-MEMS switches have a switching speed in the range of 1-200 μsec, which may be considered slow for certain applications, PIN diodes and varactor diodes offer faster switching speeds in the range of 1-100 nsec. Reconfigurable antennas using PIN diodes exhibit dynamic reconfiguration capabilities, surpassing RF-MEMS counterparts. Antennas utilizing varactor diodes achieve tuning by integrating a variable capacitor into the antenna structure, with capacitance variations controlled by adjusting the biasing voltage.

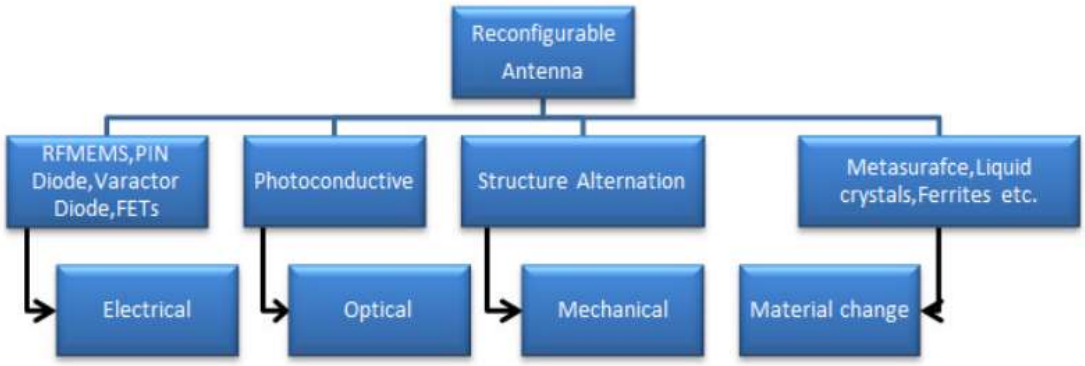

Figure 2-2 Classification of antenna reconfiguration techniques [43].

In contrast to PIN diode-based solutions, which have a limited number of discrete states, designs utilizing varactors provide continuous reconfigurability within a specific range.

Optical reconfiguration techniques rely on the use of photoconductive switching elements. The optical switches integrated into an antenna structure become conductive when exposed to a laser beam generated by integrated laser diodes. Mechanically reconfigurable antennas can be achieved by modifying the structure of the source antenna using actuators, see section 2.2.1. Additionally, reconfigurable antennas can be implemented using smart materials such as metamaterials, ferrites, liquid crystals, and dielectric fluids.

Chapter 3: Electronically Steerable Parasitic Array Radiators (ESPARs)

3.1 ELECTRONICALLY STEERABLE PARASITIC ARRAY RADIATORS

3.1.1 ESPAR concept

Electronically Steerable Parasitic Array Radiators (ESPARs) stand at the forefront of modern antenna technology, revolutionizing the way directional beams are controlled in communication systems. ESPARs distinguish themselves by their unique ability to electronically activate or deactivate individual elements, facilitating dynamic beam steering without the reliance on mechanical adjustments or phase shifters. Unlike traditional phased array antenna that employ phase shifters and true time delays (such as Rotman lens) as crucial beam scanning mechanisms, ESPARs eliminate the drawbacks associated with high losses in phase shifters, particularly above the X-band. The cost implications are substantial, as the expenses related to phase shifters can accumulate to nearly half of the total cost of an electronically scanned phased array. Given these considerations, there is a growing demand for the development of low-cost phased arrays using alternative approaches. ESPAR antennas are considered as attractive adaptive arrays due to their compact size, low cost, and the limited requirements on signal processing.

ESPAR antennas utilize the concept of parasitic elements organized in an array surrounding a central driven element. These parasitic elements are excited through coupling to the driven element and are loaded with tunable capacitances or switches, allowing the manipulation of their current phases. ESPARs' adaptability is crucial in scenarios where mechanical movements might be impractical or too slow. One of the significant advantages of ESPARs is their ability to achieve rapid beam agility while maintaining a compact and lightweight design. Unlike traditional mechanically steered antennas, ESPARs eliminate the need for bulky and heavy mechanical systems for beam adjustment, making them suitable for applications with stringent size and weight constraints such as satellite communications.

3.1.2 PIN diode-based ESPAR

PIN diode-based ESPARs operate by employing PIN diodes as switching elements, allowing for the control of parasitic elements' activation or deactivation. The reconfiguration of PIN diode-based ESPARs occurs through changes in the biasing voltage applied to the PIN diodes, allowing for discrete states of reconfiguration. This discrete reconfigurability makes them suitable for applications where specific patterns or configurations are required. In [43] a 3-element ESPAR is proposed employing three monopole elements. This design incorporates one driven element and two parasitic elements controlled through PIN diodes achieving three different pattern configurations. The number of pattern configurations can be extended by adding more parasitic elements to the antenna geometry. In [44] a low-profile ESPAR with eight parasitic elements is presented. This solution provides eight different beams covering 360 degrees with a resolution of 45 degrees. In [45] and [46], ESPAR design accomplishing twelve directive radiation patterns have been presented. Specifically, in [45] this achievement is realized by utilizing six PIN-loaded slots carved on metallic closed cylinder structure. The slots serve as parasitic elements while a monopole at the center of the cylindrical cavity acts as a driven element. While in [46], a parallel plate waveguide (PPW) section is used, consisting of a printed circuit board with a central parallel plate mode (PPM) launcher, which is surrounded by twelve electronically switchable PPM reflectors. The 13-element ESPAR proposed in [47] is capable of elevation and azimuth beam switching providing eighteen directional radiation patterns, grouped in three distinctive sets having different elevation angles. As can be noted, the use of PIN diodes or switches implies that there exists a finite number of distinct patterns, which is strongly related to the number of parasitic radiators and to the antenna geometry.

3.1.3 Varactor-based ESPAR

The unique feature of varactor-based ESPARs lies in their ability to achieve continuous reconfigurability within a specific range. In this case the parasitic elements are loaded with tunable capacitances (varactor diodes) that can be adjusted by varying their biasing voltage. The varactors are employed to dynamically control the phase of the parasitic elements' currents, allowing for smooth and continuous steering of the antenna's beam. Unlike their PIN diode counterparts, varactor-based ESPARs provide

a seamless transition between different beam configurations, making them suitable for applications where continuous adaptation to changing communication scenarios is essential. The continuous reconfigurability offered by varactor-based ESPARs addresses the need for versatile and adaptable antenna systems in modern communication networks.

The operational concept of reactively loaded antennas has been articulated in [48] and [49] for linear and planar arrays, respectively. To steer the beam to a specific direction, it is essential to determine the appropriate values of the reactive loads. A synthesis approach for estimating the reactive loads value is reported in [50]. The n-element antenna can be seen as a n-port network with n-1 ports terminated with a reactive load $Z_{Ci} = 1/j\omega C_i$. The ratio between the current on the parasitic elements and the current on the driven element can be derived as follows:

$$\begin{bmatrix} \frac{I_1}{I_0} \\ \frac{I_2}{I_0} \\ \vdots \\ \frac{I_n}{I_0} \end{bmatrix} = \begin{bmatrix} Z_{11} + Z_{C1} & Z_{12} & \cdots & Z_{1n} \\ Z_{21} & Z_{22} + Z_{C2} & & Z_{2n} \\ \vdots & & \ddots & \vdots \\ Z_{n1} & & \cdots & Z_{nn} + Z_{Cn} \end{bmatrix}^{-1} x \begin{bmatrix} -Z_{01} \\ -Z_{02} \\ \vdots \\ -Z_{0n} \end{bmatrix} \tag{3.1}$$

where I_0 is the current on the driven element, Z_{0i} and I_i are the port impedance and the current on the parasitic element *i-th*. Once that the currents ratios are determined the array factor of the antenna can be calculated with the following equation:

$$AF = \sum_{i=1}^{n} \frac{I_i}{I_0} e^{-jk \cdot r_i} \tag{3.2}$$

where k is the wavenumber and r_i is the position vector of the *i-th* element. The radiation pattern of the antenna can be estimated by multiplying the array factor in (3.2) with the element pattern, modeled as a $cos^q(\theta)$.

3.1.4 Varactor-based ESPAR: state of art

Examples of ESPAR based on reactively loaded elements can be found for 1-D scanning in [50], [51], [52], [53] showcasing different implementations using various

technologies. These designs leverage the flexibility and tunability provided by varactor diodes to achieve effective and dynamic one-dimensional beam scanning capabilities. An array of three microstrip patch antennas is employed in [50], [51] where two parasitic reactively-loaded patches are placed adjacent the non-radiating edges of the central driven patch. In both cases the beam scanning is realized along the H-plane with a steering range of 40 degrees while having a fractional bandwidth (FBW) around 1%. In particular, in [51], the 3-element ESPAR is used as a subarray in an 2x2 phased array . In this case the beam steering is achieved by the combination of ESPAR capacitive mutual coupling control and microstrip switched delay line phase shifters at the subarray level. To overcome the bandwidth limitations, cavity-backed slot antennas (CBSAs) have been used in [52] with coupling irises between the driven antenna and the parasitic radiators. In this design the beam can be steered along the E-plane from -26 to +20 degrees within an FBW of 4%. Dielectric resonator antennas (DRAs) have been employed in [53] reaching a wider FBW of 4.6% while scanning from -30 to +30 degrees.

An expanded version of [52] has been presented in [54] for 2-D beam scanning. The geometry of the antenna is extended by incorporating four parasitic elements, doubling the previous count of two, thereby enabling scanning along both the E-plane and H-plane. Furthermore, in this work, the single ESPAR has been integrated into a 20-element phased array, comprising four electronically steerable subarrays. The achieved scanning range is 90 degrees on the E-plane and 80 degrees on the H-plane without grating lobes. A noteworthy aspect is that out of the 20-element array, only four necessitate phase shifters, resulting in an 80% reduction in the number of phase shifters compared to a conventional phased array configuration. In [55], a 5-element ESPAR subarrays of DRAs is reported with a scanning range of 86, 66, and 72 degrees along the E-, H-,and D-plane. Perforated DRAs are exploited in [56], where 5-element ESPAR subarrays have been integrated into a large array comprising 240 elements arranged in a triangular lattice.

All existing examples of 2-D scanning varactor-based ESPARs are based on 5 radiating elements, four of which are parasitically coupled. This limitation in the number of parasitic radiators is directly linked to the available beam steering directions.

3.2 C-BAND ESPAR

This work introduces a novel design for 2-D beam scanning microstrip ESPAR antenna operating at 6 GHz with linear polarization. In this arrangement, both the driven and parasitic elements are implemented using standard printed circuit board (PCB) technology, eliminating the need for specialized components to control inter-element coupling. This approach allows for a 3×3 configuration, which, when scaled up to larger arrays, enables the use of a regular lattice with one driven element employed every nine array elements. Furthermore, this regular lattice design facilitates scanning in a conical region around boresight. Moreover, the utilization of conventional PCB technology simplifies the overall configuration of the ESPAR cluster and reduces its manufacturing costs.

3.2.1 One-Dimensional beam scanning ESPAR

Two-element ESPAR

The first step was the design of the 1-D scanning ESPAR, starting from the simplest geometry with two elements, one driven and one parasitic [57]. Fig. 3-1-a shows the ESPAR geometry consisting of a coaxially fed U-slot patch antenna referred to as driven element and a parasitically coupled square patch. The parasitic element, that is mutually coupled to the central driven element, is loaded with a varactor diode. The diode is located on the bottom layer, and it is connected to the parasitic antenna through a metalized via hole. The antenna stack-up (Fig. 3-1-b) consists of two core layers, referred to as D1 and D3, based on the Roger RO4350 substrate which features a relative dielectric constant of 3.66 and dielectric loss tangent of 0.004. The dielectric D3 is used to implement the radiating elements and it has a thickness of 1.524 mm while the layer D1 is used for the feeding lines and to integrate the diodes. A prepreg layer, D2, having a thickness 0.08 mm based on the Panasonic R-1551 material with relative dielectric constant of 4.6 and dielectric loss tangent of 0.015 is used to bond the two cores. The implementation of the radiating elements, ground, and varactors' bias network is achieved through the utilization of the copper layers L1, L2, and L3, respectively. The key design drivers are related to three components: the driven element, the coupling level between the driven and parasitic element, and the reactive loaded parasitic element.

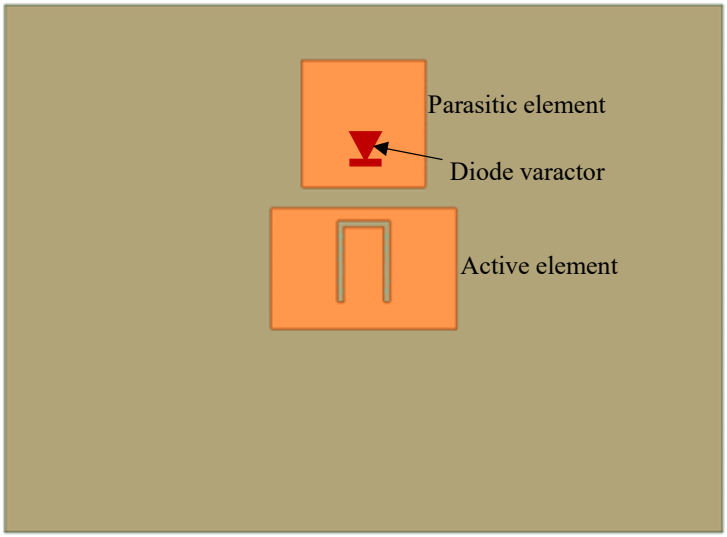

(a)

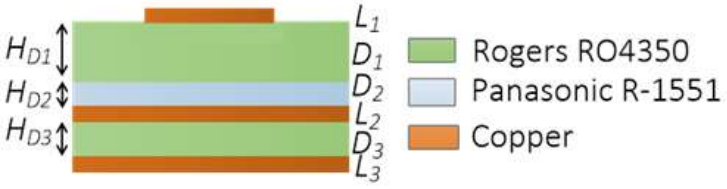

(b)

Figure 3-1 Two-element ESPAR a) geometry and b) stackup.

The driven element, which plays a key role in the ESPAR design, must operate over a wide band in order to compensate the alterations of the reflection coefficient due to the change of the parasitic elements' reactive loads. To address this concern, the configuration of the driven element was based on a U-shaped slot antenna, which has been demonstrated to yield significant bandwidth enhancement compared to conventional patch antennas [58]. However, it should be noted that achieving wide bandwidths typically necessitates the use of thicker substrates. In the present case, substrate selection also plays a crucial role as it influences the coupling between the driven and parasitic radiators. Specifically, a thinner substrate facilitates improved coupling on the H-plane [59]. Consequently, a compromise was necessary, balancing the desired bandwidth and the level of coupling between the driven and parasitic elements.

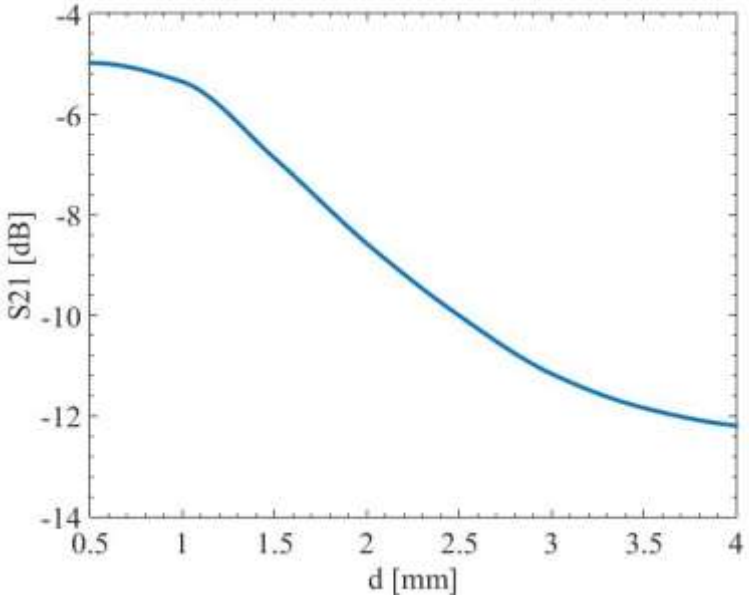

Figure 3-2 Coupling level between driven and parasitic element versus distance.

The coupling level between the driven and parasitic elements is one of the key design parameters. Not only do the steering capabilities of the system heavily rely on the excitation level of the parasitic element, but the final bandwidth is also affected. The coupling between the driven and parasitic element versus the edge-to-edge distance is depicted in Fig. 3-2. An optimum distance of 2 mm has been found out through a simulation optimization, with a coupling level of about -9 dB which provides the best compromise between steering range and FBW.

The beam steering capabilities of the antenna have been evaluated by firstly analyzing the phase variation of the parasitic element. This parasitic patch is validated as an isolated cell excited by an impinging wave having the same polarization of the driven element, Fig. 3-3. A through via connects the varactor cathode to the center of the parasitic patch while the anode is grounded through a blind via between L_2 and L_3. The radius of both vias is equal to 0.7mm while the through via is placed 2 mm apart the patch center and in L_1 it is connected to a 3×3 mm pad. The position of the loading via hole, D_v, can be estimated by using the following equation [60]:

$$D_V = \frac{L_P}{\pi}\sin^{-1}\left(\sqrt{\frac{R_i}{R_e}}\right) \tag{3.1}$$

where R_i is the desired input resistance, 50 Ω, and R_e is the resistance at the edge of the patch. The varactor behaviour has been simulated by using a sheet component with

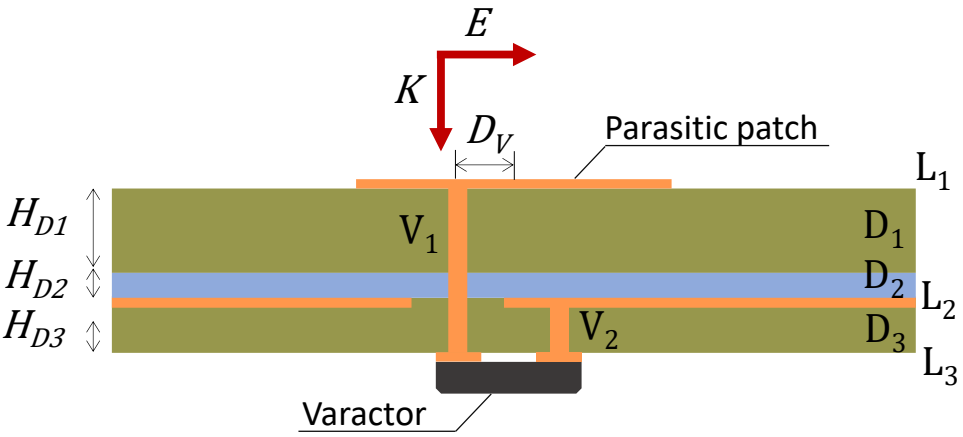

Figure 3-3 Parasitic element simulation setup side view.

Figure 3-4 Equivalent circuit of the varactor diode including the parasitic effects of the package. (L_{Par} = 0.4 nH, and C_{Par} = 0.06 pF)

lumped boundary condition. The lumped condition is given by the equivalent circuit of the varactor including the parasitic effects of the package. It consists of a series RLC circuit including the parasitic inductance and the total capacitance, given by the sum of the junction capacitance and the package parasitic capacitance. The equivalent circuit of the varactor is depicted in Fig. 3-4. The phase of the field scattered by the varactor loaded parasitic cell versus the varactor capacitance is shown in Fig. 3-5. A phase range of 360 degrees is achieved within a tuning range of 550 fF, from 50 to

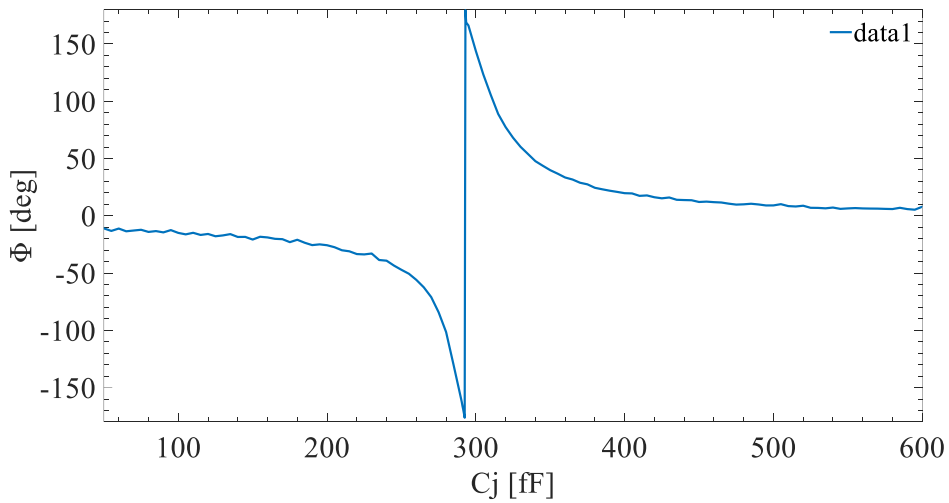

Figure 3-5 Phase of the field scattered by the parasitic element versus the varactor capacitance.

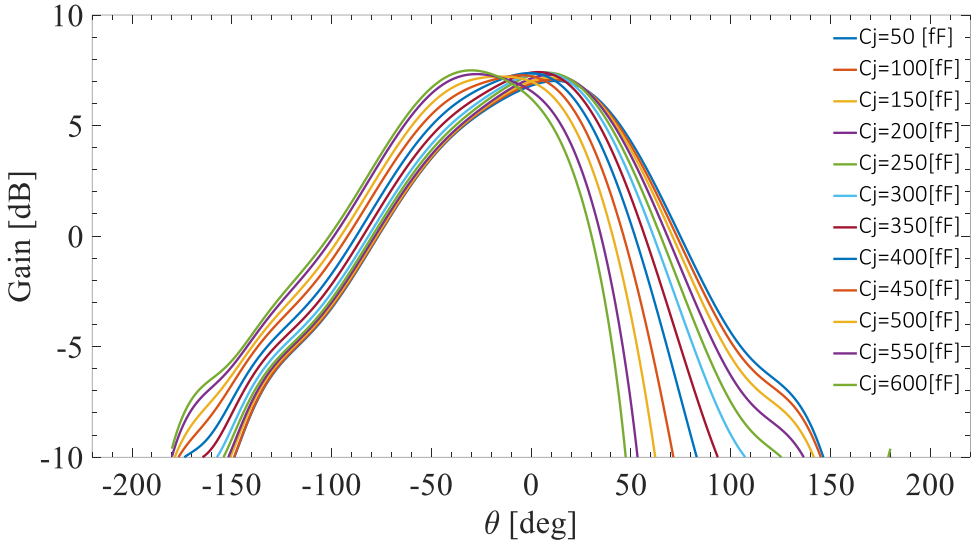

(a)

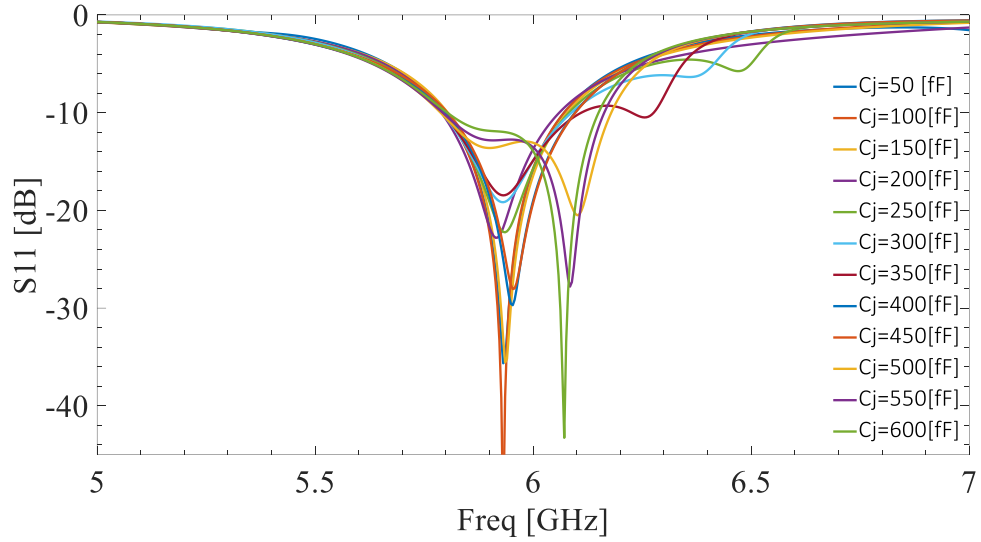

(b)

Figure 3-6 Simulated a) radiation pattern, and b) return loss for different varactor configurations.

600 fF. With one parasitic element the scanning is about 45 degrees, from -29° to +16°, Fig. 3-6-a, while the ESPAR bandwidth ranges from 5.79 to 6.06 GHz corresponding to a fractional bandwidth of 4.5%, Fig. 3-6-b.

Three-element ESPAR

The design shown in Fig. 3-1-a has been extended to 3-element geometry by adding one more parasitic patch placed on the opposite side of the driven element [61]. The ESPAR geometry is depicted in Fig. 3-7 along with all the relevant geometrical parameters, Table 3-1. To achieve symmetrical antenna geometry, ensuring identical

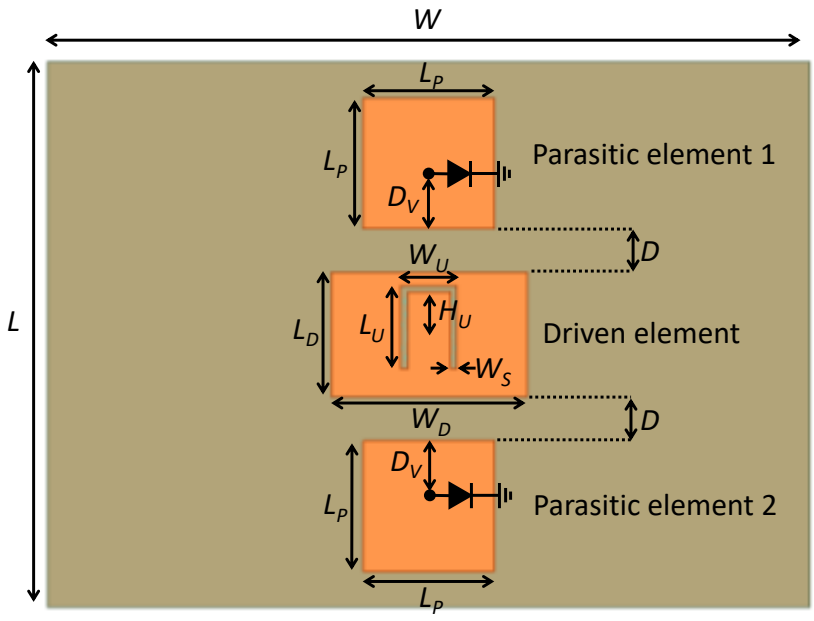

Figure 3-7 Three-element ESPAR geometry.

Table 3-1 Key geometrical parameters' values.

Parameters	Value (mm)	Parameters	Value (mm)
L	50	W_S	0.6
L_D	11.47	D	2
L_P	12	D_V	4
L_U	7.67	H_U	3.95
W	70	H_{D1}	1.524
W_D	18	H_{D2}	0.08
W_U	5.1	H_{D3}	0.254

control of the two elements, the position of the varactors is mirrored relative to the position of the active element. To validate the 3-element ESPAR design a prototyped has been realized and experimentally validated, Fig. 3-8. The Macom MGV125-08-0805-2 varactor diode has been used to achieve the cluster reconfigurability. Its nominal junction capacitance varies between 0.6 pF and 0.055 pF with a reverse biasing from 2 V to 22 V. The simulated and measured steering range are 77 degrees and 81 degrees, respectively. The Co-Pol and Cross-Pol E-plane radiation pattern is depicted in Fig. 3-9 for eight different varactors configurations. As can be seen the cluster pointing direction can be continuously controlled from -51 to +30 degrees; the scanning range asymmetry observed can be attribute to an uneven coupling level between the driven element and the parasitic elements. This is primarily caused by the presence of a U-slot etched on the driven element. The measured cross-polar field

(a)

(b)

Figure 3-8 Three-element ESPAR a) prototype top-view and b) mounted in the receiving must of the anechoic chamber.

remains below -15 dB across the entire steering range. Fig. 3-10 shows a comparison between the simulated and measured return loss. The measured fractional bandwidth, which is approximately 1.5%, is centered around 6 GHz. The measurement results indicate that the cluster exhibits a peak gain of 8.64 dBi in the boresight configuration. However, as the pattern is steered towards the extremes of the steering range, the peak gain decreases to 7 dBi. This trend is illustrated in Fig. 3-11.

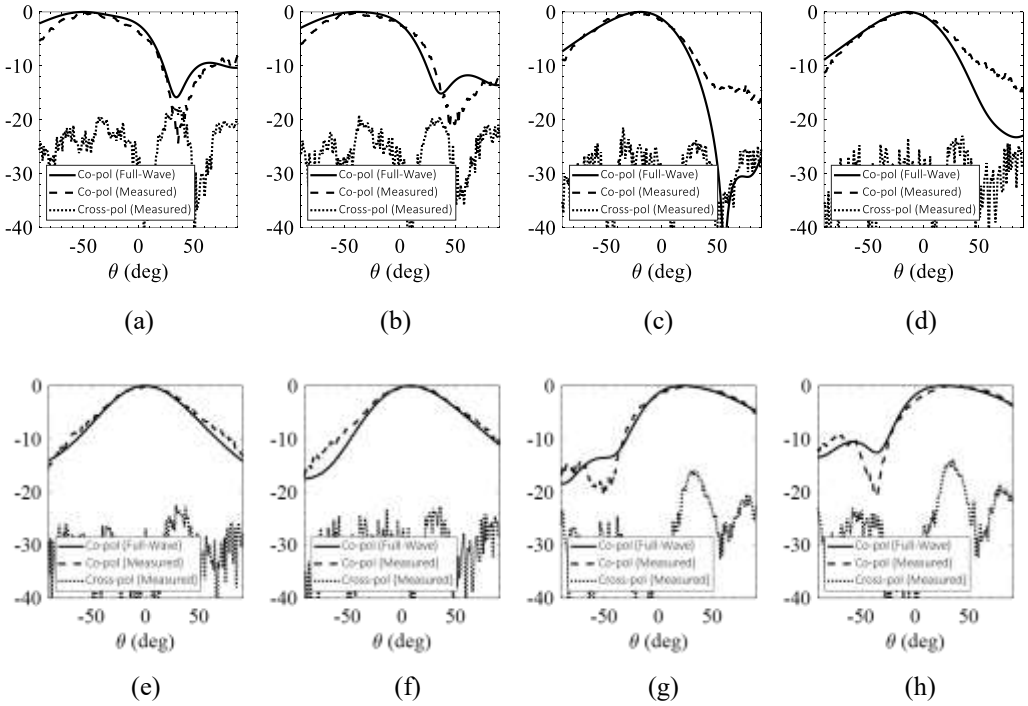

Figure 3-9 Full-wave and measured E-plane radiation pattern (dB) for different varactors' configurations a) C1=0.6 pF (2V) and C2=0.055 pF (22V), b) C1=0.55 pF (2.8V) and C2=0.1 pF (20V), c) C1=0.45 pF (3.6V) and C2=0.3 pF (6.4V), d) C1=0.41 pF (4V) and C2=0.37 pF (4.6V), e) C1=0.39 pF (4.3V) and C2=0.41 pF

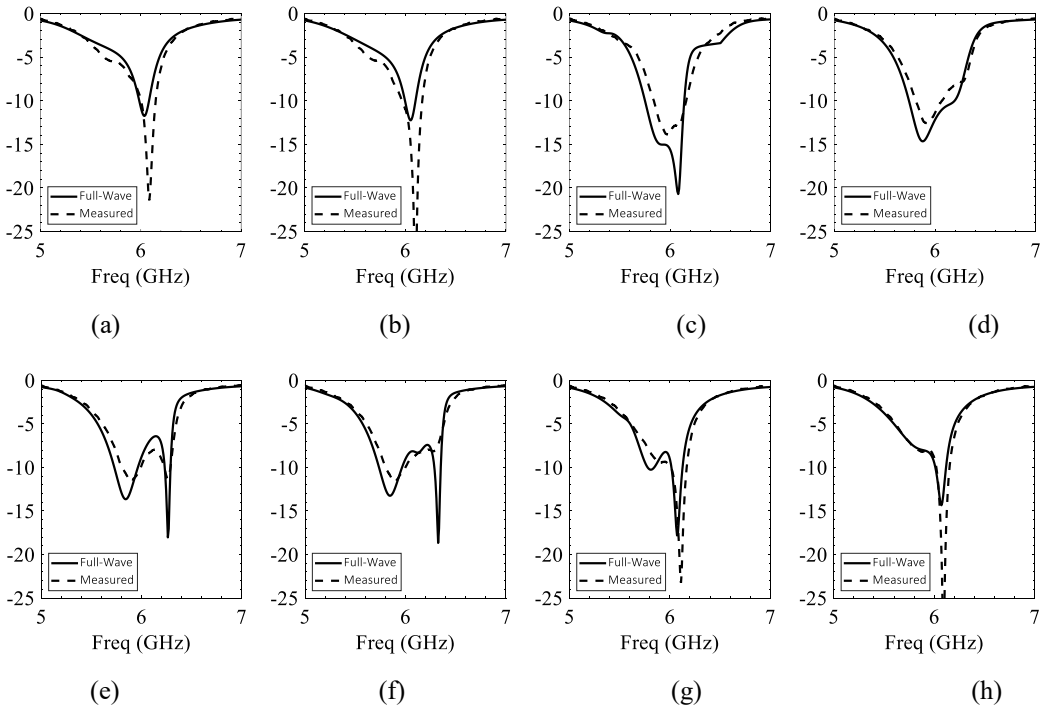

Figure 3-10 Full-wave and measured return loss (dB) for the pattern configurations shown in Fig. 3-9.

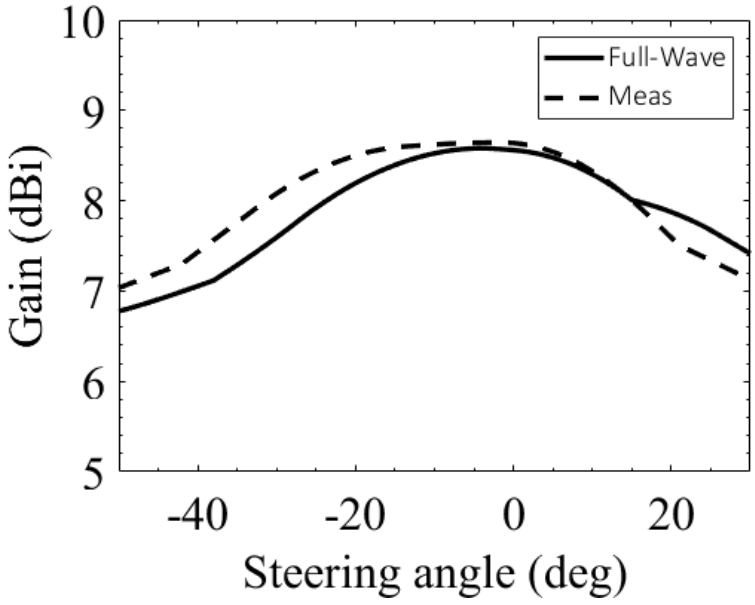

Figure 3-11 Full-wave and measured peak gain versus steering angle.

The 3-element ESPAR was simulated in a linear large array configuration comprising six clusters. As depicted in Fig. 3-12, a comparison was made between a clustered array, a 0.5λ spaced array, and a 0.85λ spaced array (where the driven element spacing is).

The proposed hybrid cluster-based solution allows for a beam steering range along the E-plane of 160 degrees, ranging from -80 to +80 degrees without generating grating lobes. It is noteworthy that only the driven elements require RF phase control (phase shifter), resulting in a 66% reduction in the number of phase shifters.

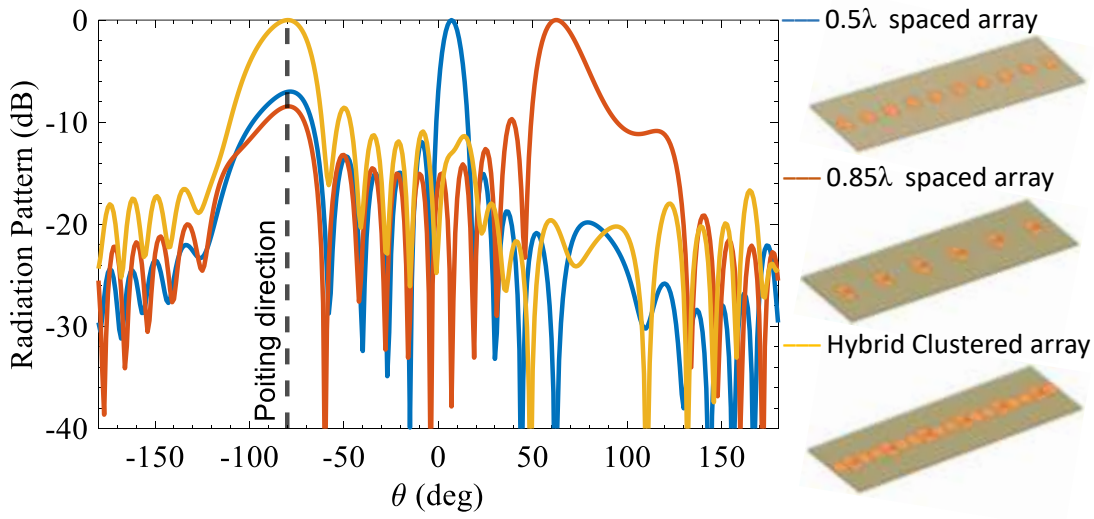

Figure 3-12 Radiation pattern comparison among a 0.5λ-spaced array, 0.85λ-spaced array, and the proposed hybrid clustered array when steering the beam to -80 degrees.

3.2.2 Conical beam scanning ESPAR

The final ESPAR geometry has been presented in [62]. It consists of nine microstrip patch antenna (MPA) elements arranged in a 3×3 lattice. Compared to the existing 2-D ESPAR designs, based on a geometry with 5 elements, in this solution four more parasitic elements, located along the two diagonal planes, are added. This allows the control of the phase gradient along further azimuthal planes, thus, extending the beam scanning capabilities to a conical region. The geometry of the antenna is depicted in Fig. 3-13 together with all the relevant geometrical parameters' values, Table 3-2. The figure 3-14-a depicts the top layer of the PCB, which includes the 3x3 array with the central driven element surrounded by 8 parasitic elements, while figure 3-14-b, corresponding to the bottom layer of the circuit, was used to implement the biasing networks of the varactors. The full-wave simulated and measured return loss corresponding to scan angles of 0°, +30° in E-plane, +37° in H-plane, and +25° in D-plane are presented in Fig. 3-14, along with images of the realized prototype. With respect to simulations, a small upshift is observed. The active impedance variations

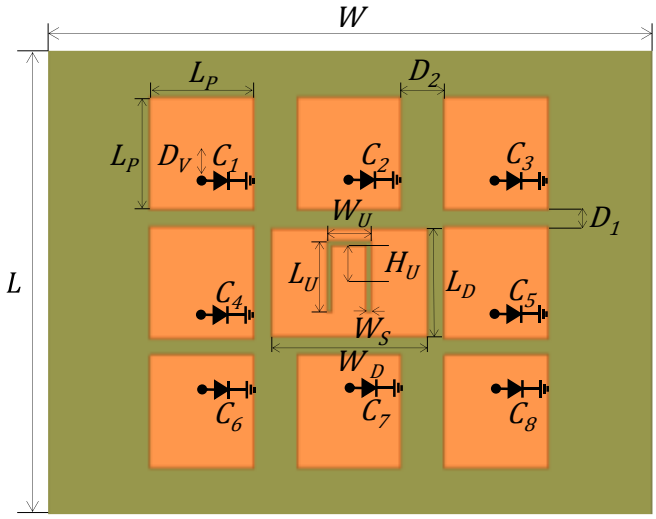

Figure 3-13 Nine-element ESPAR geometry

Table 3-2 Key geometrical parameters of the proposed antenna

Parameter	Value (mm)	Parameter	Value (mm)
L	50	L_U	7.67
W	70	W_U	5.1
H_{D1}	1.524	H_U	3.95
H_{D2}	0.08	D_1	2
H_{D3}	0.254	D_2	5
L_P	12	D_V	2
L_D	11.47	W_S	0.6
W_D	18		

due to the different beam steering configurations determines a reduction of the operational bandwidth as it is observed from the reflection coefficient at the driven element which remains below -10 dB from 6.02 to 6.13 GHz, corresponding to 1.8 % of fractional bandwidth.

Figures 3-15, 3-16 and 3-17 illustrate various radiation pattern configurations corresponding to the E-, H-, and D-plane, respectively. The comparative analysis between the simulated and measured results demonstrates a notable level of agreement. In particular, for the E-plane, the scanning capability spans approximately 75 degrees, ranging from -45 to +30 degrees. On the H-plane, beam steering is attainable within the range of -37 to +37 degrees, while on the D-plane, the steering range extends from -36 to +25 degrees. Due to the symmetry of the array lattice the results can be extended to the other azimuthal planes. The asymmetry in the steering range on E- and D-plane is due to the uneven coupling levels between the driven element and the parasitic

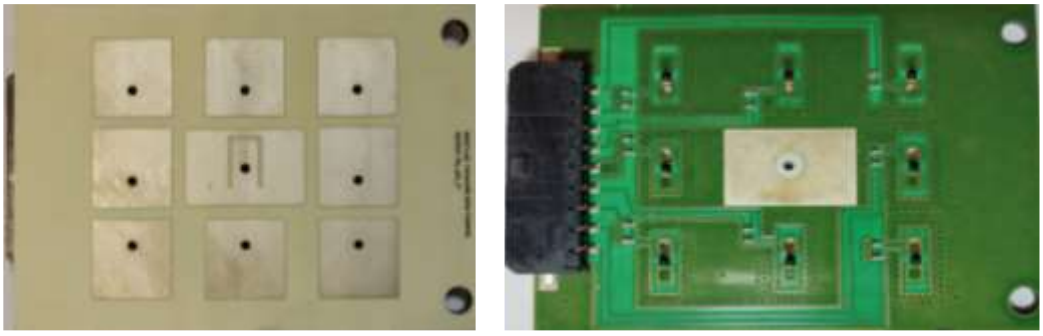

(a) (b)

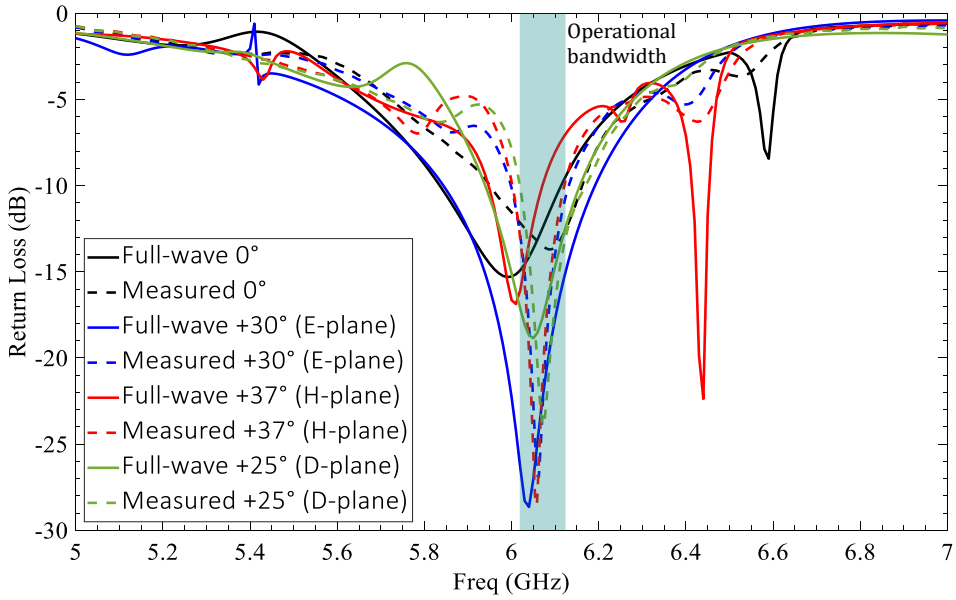

Figure 3-14 Nine-element ESPAR prototype: a) top view, b) bottom view, and c) full-wave and measured return loss for different antenna configurations.

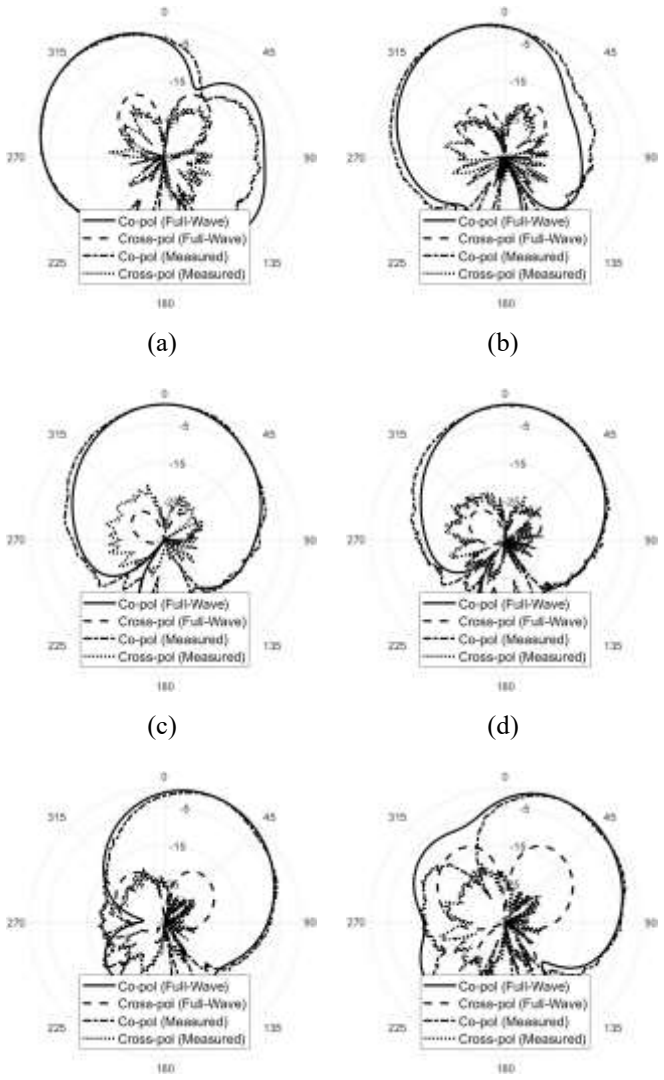

Figure 3-15 Full-wave and measured co- and cross-pol E-plane radiation pattern at 6.05 GHz for different antenna configurations.

elements along the E-plane, stemming from the inclusion of the U-slot in the driven element. During the scanning process on the E-, H-, and D-plane, the cross-polarization levels were found to be below -14 dB, -15 dB, and -10 dB, respectively. Furthermore, the measured side lobe levels (SLL) during scanning on the E , H , and D plane were observed to be below -11 dB, -8 dB, and -7 dB, respectively.

The measured antenna gain exhibits a peak value of 8.2 dBi when the beam is steered to -20° on E-plane. A minimum gain of 6.5 dBi is measured when scanning to ±37° on the H-plane. Fig. 3-18 shows the simulated and measured gain at 6.05 GHz versus the steering angle. Compared to other 2-D design examples, reported in Table 3-3, the proposed configuration is the only cluster based on 9 radiating cells implemented using simple and low-cost PCB stack-up. At variance of the other techniques, based on DRA

or CBA, the operating bandwidth is increased by customizing the design of the driven element which, for the reported example, was implemented using a U-slot patch antenna. This solution led to an operational bandwidth of 1.8% with an aperture efficiency of 38 %. The experimental results showed a continuous scanning range of 75 degrees on E-plane, whereas on H-plane and D-plane, the scanning capabilities extend approximately to 74 degrees and 60 degrees, respectively.

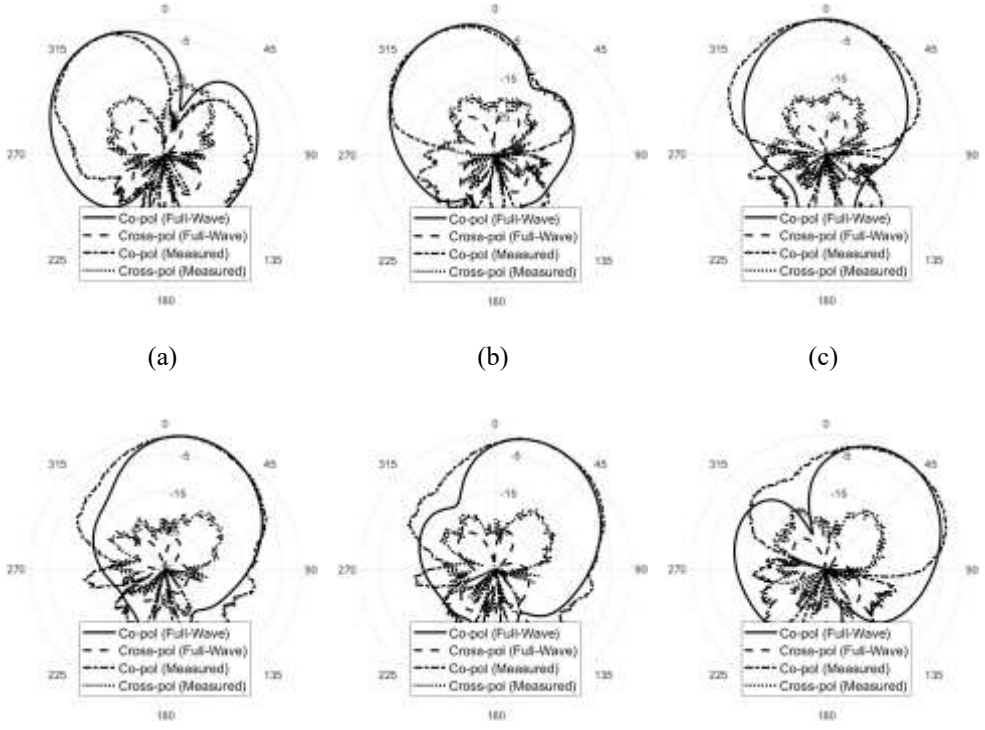

(a) (b) (c)

(d) (e) (f)

Figure 3-16 Full-wave and measured co- and cross-pol H-plane radiation pattern at 6.05 GHz for different antenna configurations.

Table 3-3 Comparison of 2-D beam scanning ESPAR antenna.

	[10]	[11]	[12]	[13]	This work
Radiating element	CBSA	DRA	DRA	DRA	MPA
Number of radiating elements	5	5	5	5	9
FBW (%)	6.4	< 1	-	3.97	1.8
Phase shifter reduction (%)	80	80	80	80	89
Aperture efficiency (%)	32	58	20.4	15	38
Number of azimuthal scanning planes	4	4	4	4	8
Steering range (deg)	-	86	-	44	75

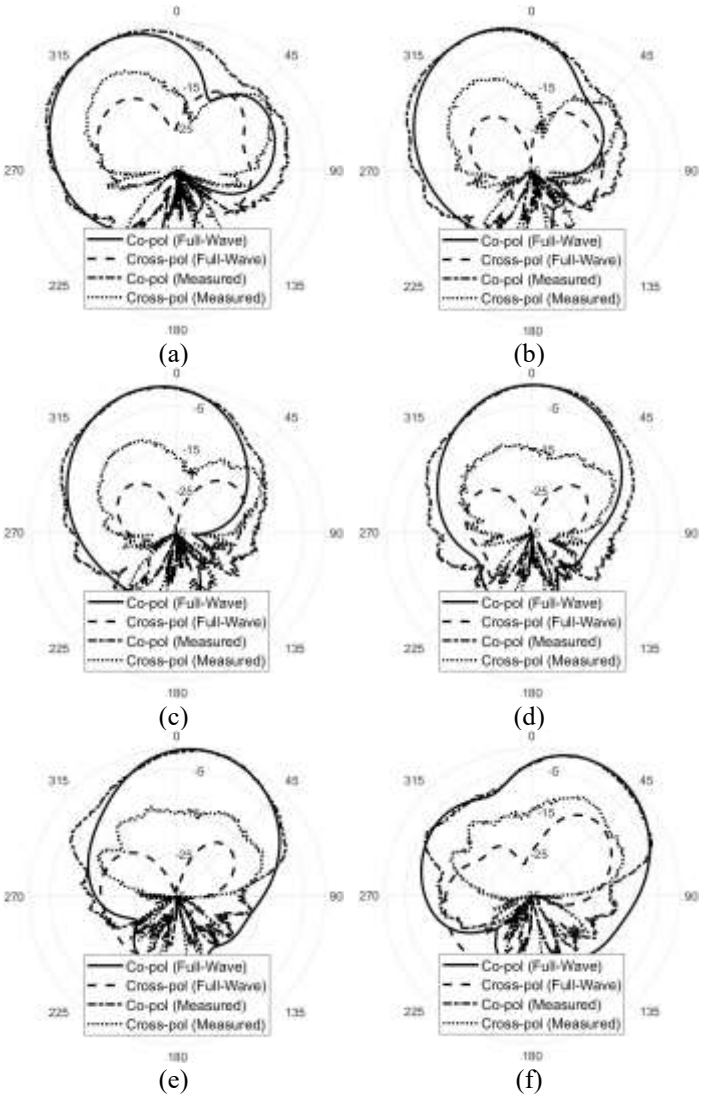

Figure 3-17 Full-wave and measured co- and cross-pol D-plane radiation pattern at 6.05 GHz for different antenna configurations.

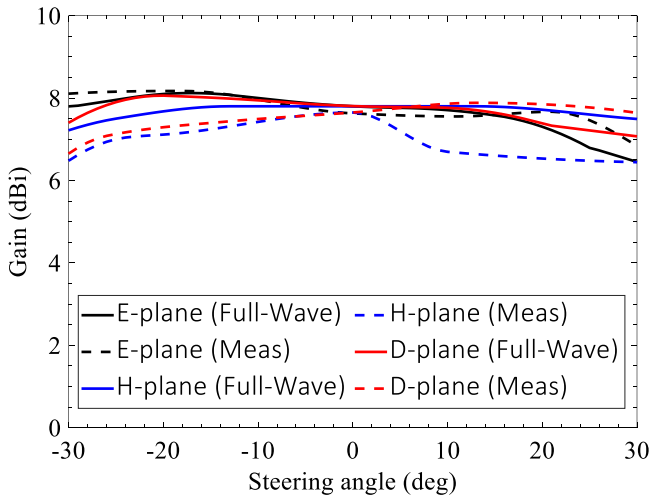

Figure 3-18 Full-wave and measured gain at 6.05 GHz versus the steering angle for E-, H-, and D-plane scanning.

3.3 K-BAND ESPAR

In recent years, the Ku and Ka bands have played a crucial role in the advancement of satellite communications. A comprehensive analysis of the LEO user segment in the Ku and Ka bands is presented in [20]. In this context, a key objective is to reduce the cost and complexity of the antenna system without compromising overall performance. Electronically steerable parasitic array radiators (ESPARs) emerge as viable solutions since they enable a significant reduction in the number of phase shifters and simplify the beamforming network.

In this thesis, two different examples of microstrip ESPAR design at K-band are presented [63]. The proposed designs consist of a 3-element cluster based on microstrip patch antennas operating with linear and circular polarization, respectively. The two ESPAR consist of one driven element and two parasitic elements, employing the same working principle as the C-band ESPAR showed in the previous section.

3.3.1 Linearly polarized 1-D scanning ESPAR

The geometry of the linearly polarized cluster is depicted in Fig. 3-19 along with some relevant geometrical parameters' values, Table 3-4. It consists of three square patch

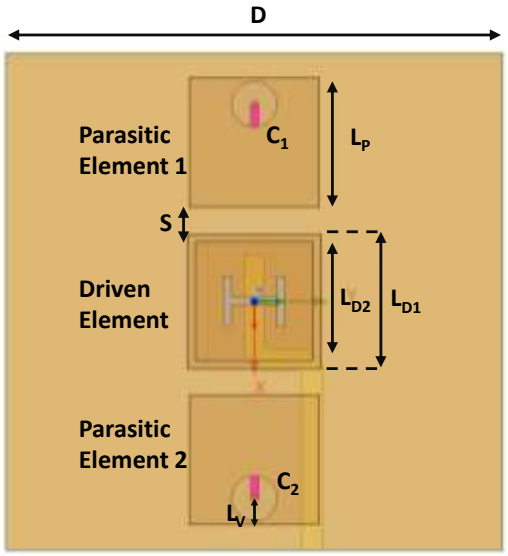

Figure 3-19 Linearly polarized cluster geometry.

Table 3-4 Linearly polarized cluster most relevant geometrical parameters values.

Parameter	Value (mm)	Parameter	Value (mm)
D	13	L_P	3.4
L_{D1}	3.5	L_{D2}	3.1
S	0.9	L_V	0.7

antennas, one driven and two parasitic placed along the two radiating edges of the driven patch. Each parasitic element is loaded with a varactor placed on the external radiating edge of the patches. The driven element is implemented through an aperture coupled stacked patch in order to have a wider bandwidth. The geometry showed is Fig. 3-19 allows the beam steering along the E-plane (1-D scanning). The antenna

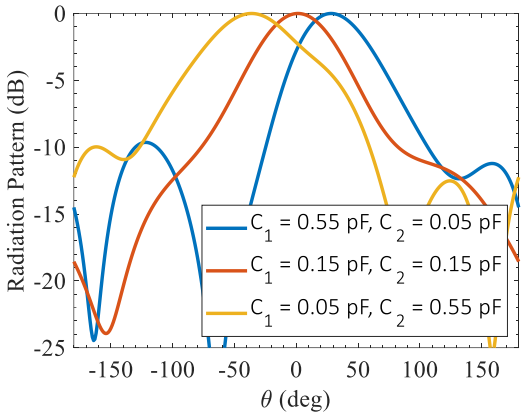

(a)

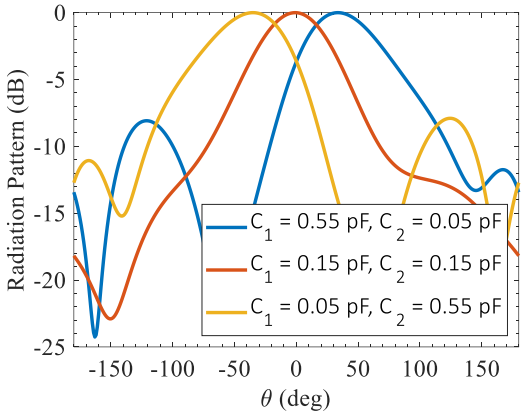

(b)

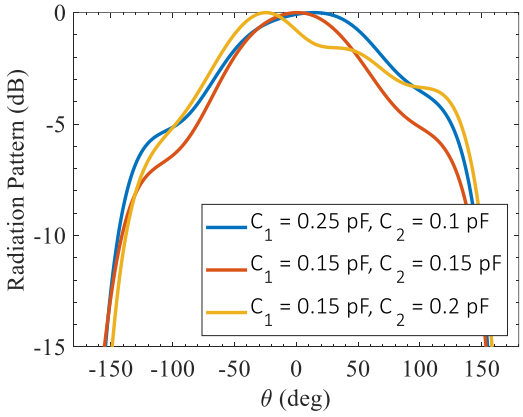

(c)

Figure 3-20 Cluster E-plane pattern for different varactor configurations at a) 19 GHz, b) 20 GHz and c) 21 GHz.

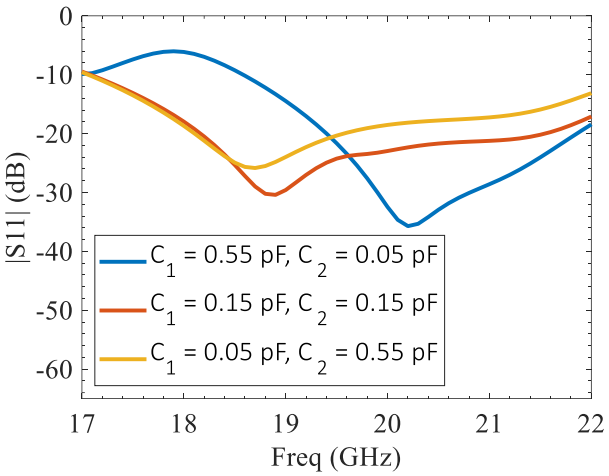

Figure 3-21 Cluster return loss for the reported beam configurations.

stack-up consists of three dielectric slabs, from top to bottom, one 1.524 mm Rogers RT/duroid 5880 substrate and two Rogers RO4350 dielectric slabs having a thickness of 0.508 mm and 0.254mm, respectively. Fig. 3-20 shows the cluster E-plane pattern for different varactors' configurations at 19, 20, and 21 GHz. At 19 GHz the simulated steering range is about 60 degrees, ranging from -35° to +25°. At 20 GHz the beam can be directed from -35° to +35°, while at 21 GHz the steering range is about 40 degrees. The simulated peak gain at 20 GHz is 7.5 dB corresponding to an aperture efficiency of 60%. The simulated return loss is shown in Fig. 3-21, the fractional bandwidth (FBW) is about 20% ranging from 18.5 GHz to 22.5 GHz.

3.3.2 Circularly polarized 1-D scanning ESPAR

The proposed circularly polarized microstrip ESPAR makes use of three hexagonal patch antennas. The driven patch is realized through a stacked aperture coupled patch antenna while the two parasitic elements are implemented with two patches, Fig. 3-22. The two parasitic patches are placed on the same layer of the patch directly coupled to the slot (active patch). Like the linearly polarized design this geometry allows 1-D beam steering along the E-plane. The design of a circularly polarized ESPAR is more challenging respect to the linearly polarized one because of the intrinsic difficulty to control the parasitic element current components. To attain an axial ratio (AR) below 3 dB during scanning operations, it is imperative that the two components of the parasitic elements' current, I_x and I_y, exhibit the same reactive loads. For this reason, each parasitic patch is loaded with four varactors placed along the patch axes. Compared to the linearly polarized cluster more varactors are needed, however, the four varactors of each parasitic element are controlled with the same bias voltage. This

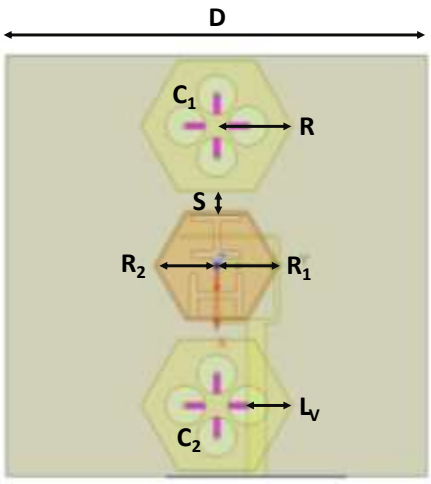

Figure 3-22 Circularly polarized cluster geometry.

Table 3-5 Circularly polarized cluster most relevant geometrical parameters.

Parameter	Value (mm)	Parameter	Value (mm)
D	12.8	R	2.3
R_1	1.9	R_2	1.8
S	0.7	L_V	1.05

means that the complexity of the biasing network is almost unchanged. The simulated E-plane pattern and axial ratio at 19 GHz and 20 GHz are reported in Fig. 3-24 and Fig. 3-25, respectively, for different varactor configurations. At 20 GHz the steering range is about 54 degrees, from -27° to +27°, within an axial ratio less than 1.9 dB. At 19 GHz the pattern can be steered from -19° to +19° while having an axial ratio less than 2.3 dB. The simulated return loss is shown in Fig. 3-23. A fractional bandwidth of about 6% has been achieved ranging from 19 GHz to 20.25 GHz.

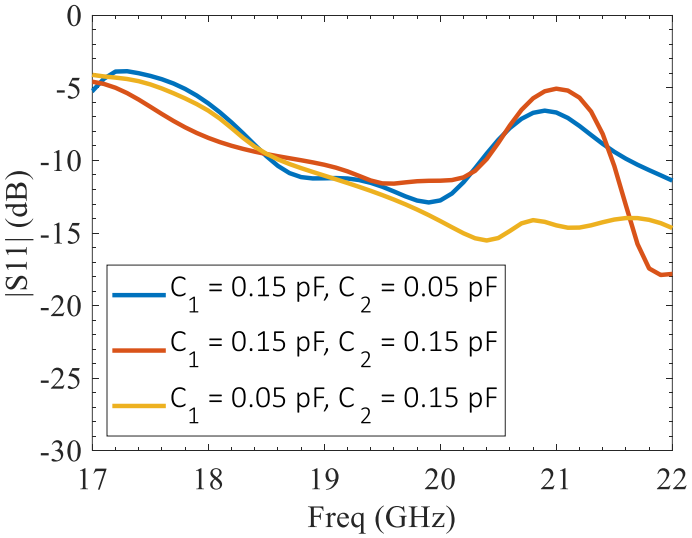

Figure 3-23 Simulated return loss for the reported beam configuration.

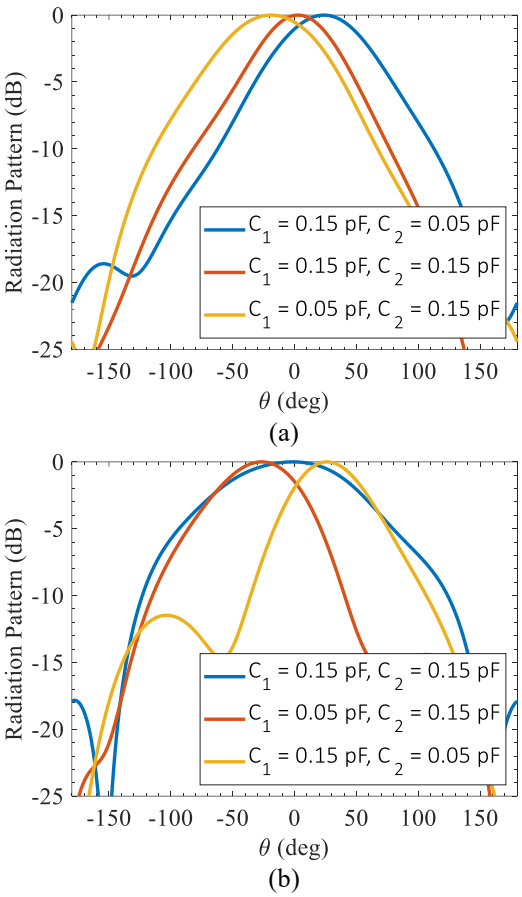

Figure 3-24 Circularly polarized cluster pattern at a) 19 GHz and b) 20 GHz.

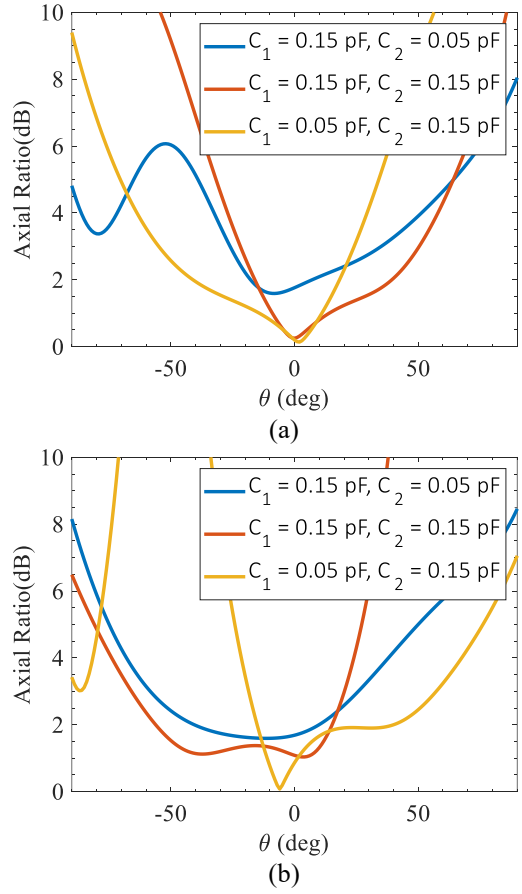

Figure 3-25 Simulated axial ration at a) 19 GHz, and b) 20 GHz.

3.3.3 Linearly polarized 2-D scanning ESPAR

The linear polarized K-band reported in the previous paragraph has been extend to a 2-D beam scanning configurations by incorporating two more parasitic elements [64]. Moreover, the five-element ESPAR has been incorporated into a large array architecture to demonstrate the tangible capabilities of this approach.

The geometry of the proposed ESPAR subarray, designed to work at 20 GHz with linear polarization, is reported in Fig. 3-26 with the most relevant geometrical parameters value, Table 3-6. It comprises five distinct radiators arranged in a cross-shaped disposition. The central element is implemented through a stacked aperture coupled microstrip square patch antenna and it acts as a driven element. Four varactor-loaded parasitic square patch antennas are used as parasitic elements allowing the beam steering along both E- and H-plane. The full-wave simulated subarray's pattern at 20 GHz for different varactors' configurations is reported in Fig. 3-27.

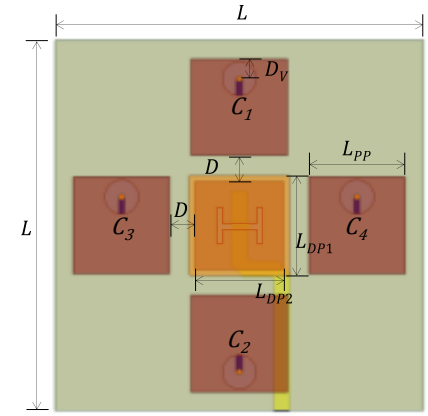

(a)

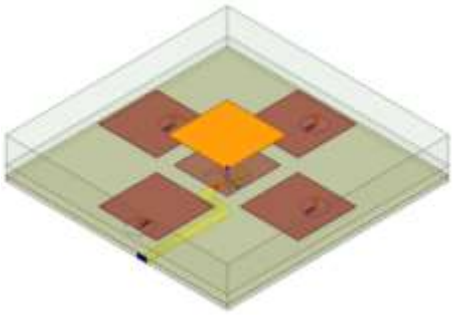

(b)

Figure 3-26 Subarray geometry a) top view, and b) isometric view.

Table 3-6 Most relevant geometrical parameters' values

Parameter	Value (mm)	Parameter	Value (mm)
L	13	L_{DP2}	3.1
L_{PP}	3.4	D	0.9
L_{DP1}	3.5	D_V	0.7

A continuous steering range of 50 degrees, from -25° to +25°, has been observed while scanning on E-plane. The H-plane steering range, instead, goes from -40° to +40°. At 19.25 GHz, the scanning range on the E-plane is 55 degrees, while on the H-plane, it is 65 degrees (refer to Fig. 3-28). At 20.75 GHz, the beam can be steered within a range of 30 degrees on the E-plane and 40 degrees on the H-plane, Fig. 3-30. The overall simulated cross-pol level is below -15 dB. Figure 3-29 shows the full-wave simulated return loss for the beam configurations reported in Fig. 3-27. A fractional bandwidth (FBW) of about 13% has been observed while scanning on E- and H-plane, ranging from 18.5 GHz to 21 GHz. The simulated subarray's peak gain is 7.85 dBi corresponding to an aperture efficiency of about 65%.

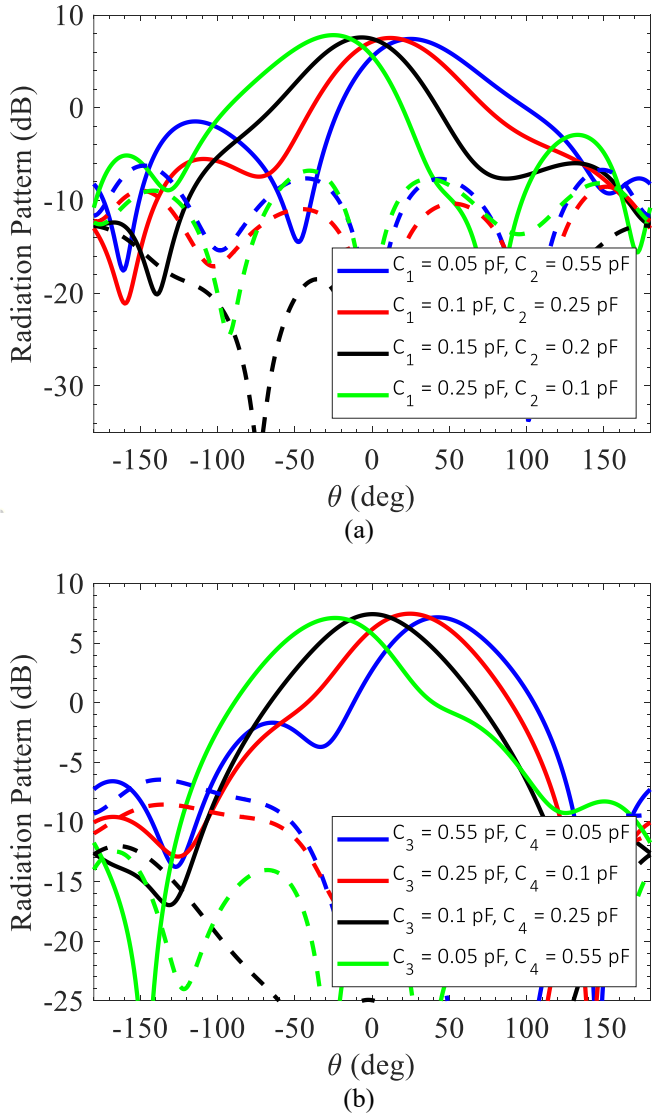

Figure 3-27 Subarray co- and cross-pol unnormalized a) E-plane pattern and b) H-plane pattern at 20 GHz. During E-plane scanning, the capacitances C3 and C4 are fixed to 0.15 pF, whereas for H-plane scanning, C1 and C2 are held constant at 0.15 pF.

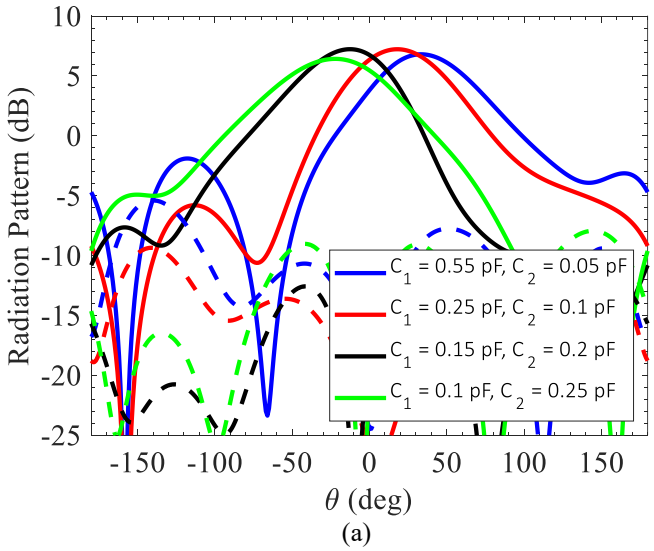

Figure 3-28 Subarray co- and cross-pol unnormalized a) E-plane pattern and b) H-plane pattern at 19.25 GHz. During E-plane scanning, capacitances C3 and C4 are fixed to 0.15 pF, whereas for H-plane scanning, C1 and C2 are held constant at 0.15 pF.

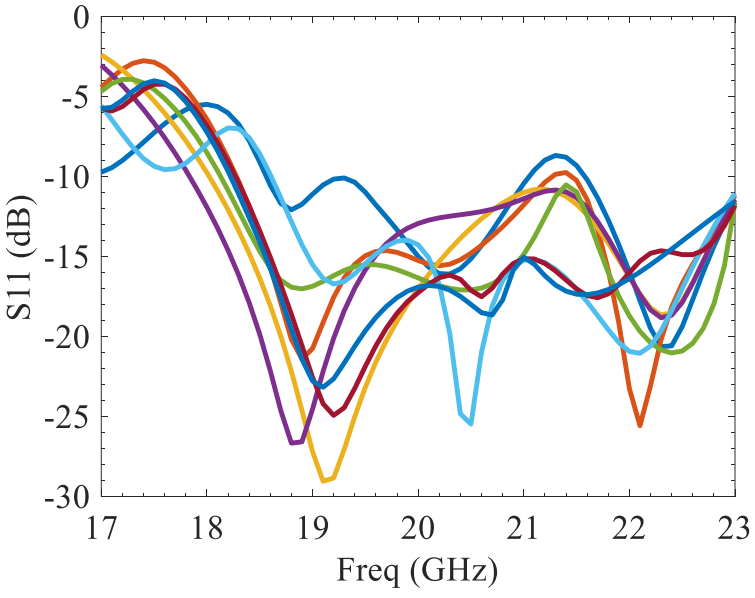

Figure 3-29 Simulated subarray return loss for different varactors' configurations.

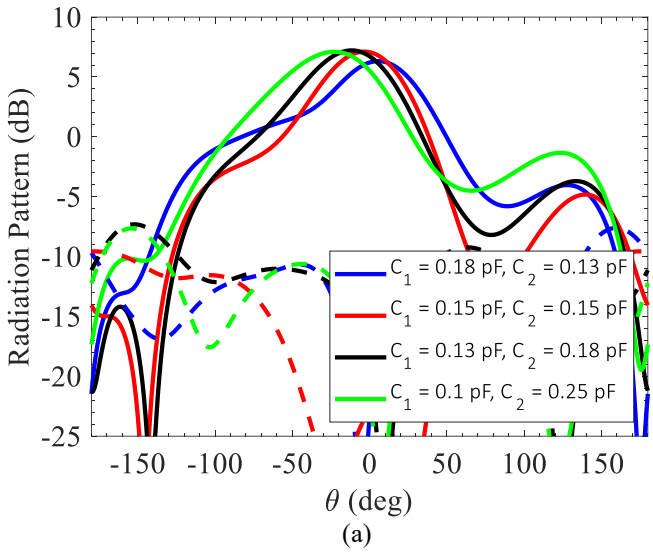

(a)

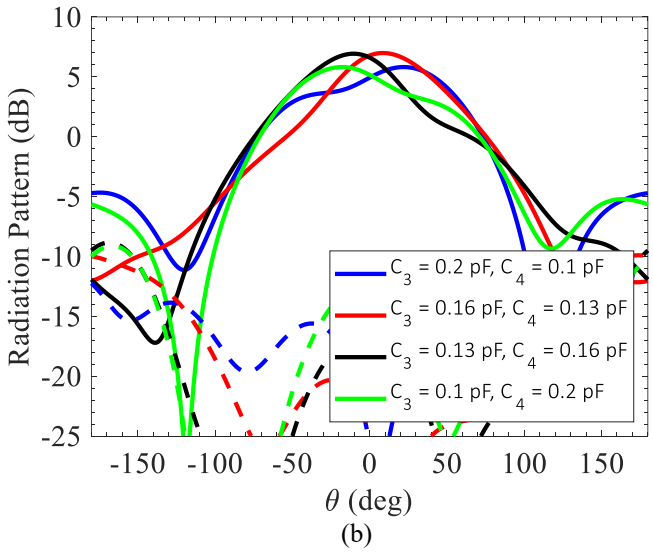

(b)

Figure 3-30 Subarray co- and cross-pol unnormalized a) E-plane pattern and b) H-plane pattern at 20.75 GHz. During E-plane scanning, capacitances C3 and C4 are fixed to 0.15 pF, whereas for H-plane scanning, C1 and C2 are held constant at 0.15 pF.

3.3.4 Large array concept and simulation

To demonstrate the true capabilities of the ESPAR-based array, the subarray described in Section 3.3.3 has been incorporated into a large array design. The basic concept of large planar array based on ESPAR is depicted in Fig. 3-31-a. When incorporating the subarray into the large array, it is essential to ensure that the subarray's pattern beam is pointed to the desired scanning direction. Consequently, the driven elements must be equipped with the necessary phasing to orient the beam of the large array in the same direction as the subarray. The phase relationship with the reactive loads will

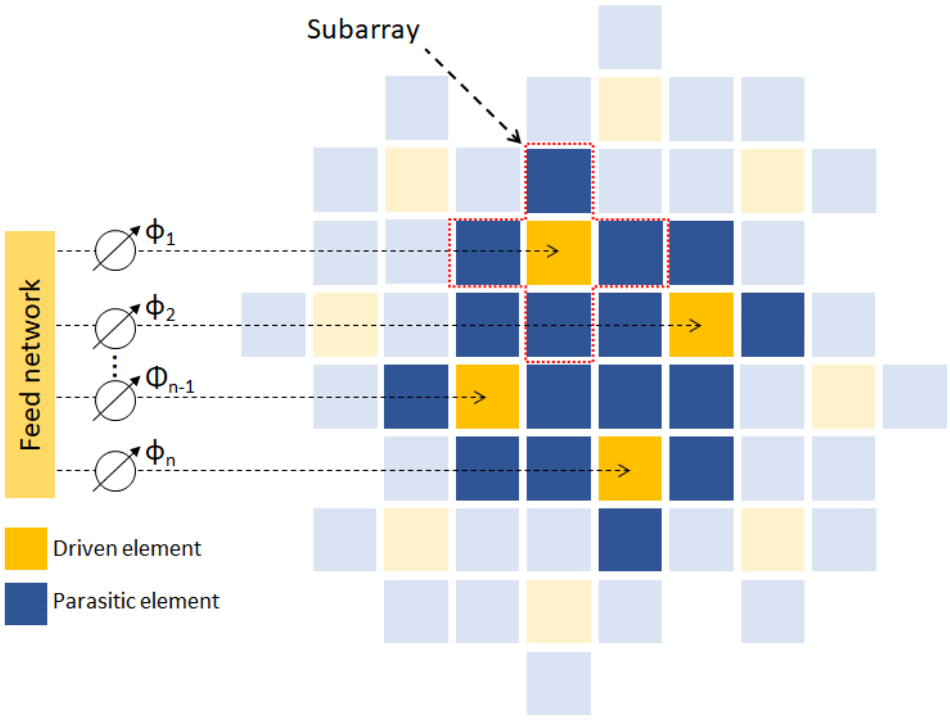

(a)

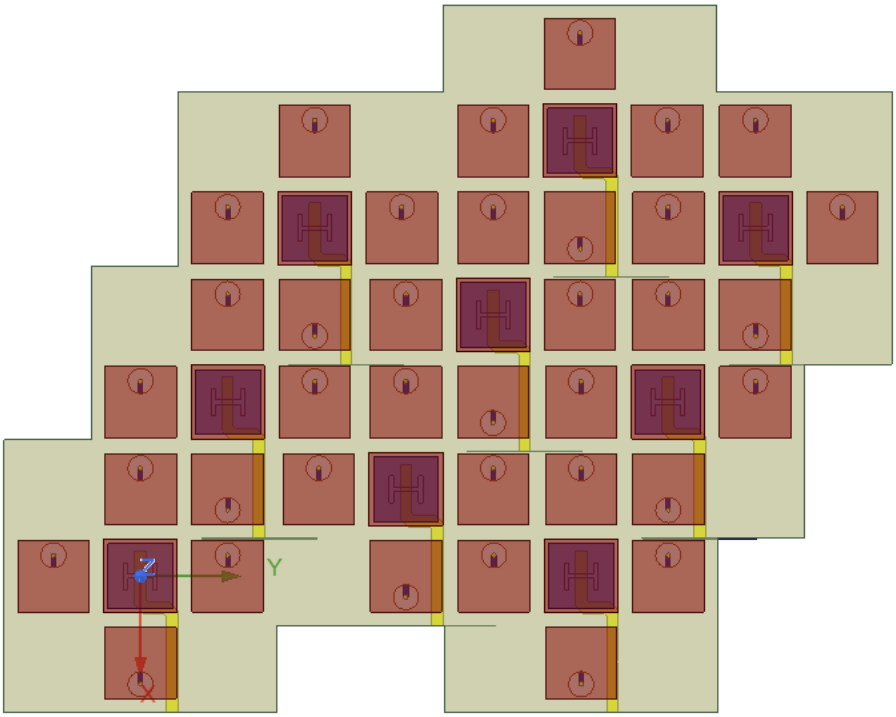

(b)

Figure 3-31 Large array based on interleaved 5-element subarrays: a) concept, and b) simulation setup.

remain consistent in relation to the driven element. Only the driven elements require phase shifters. It is also interesting to observe that the grating lobes level of the large array can be decreased by controlling the reactance of the parasitic elements. The cross-shaped subarrays are arranged in an interleaved triangular lattice which consists

of 9 elements. This subarray arrangement provides a higher efficiency and an extended scanning range [55]. A large array of nine interleaved subarrays has been simulated, each subarray's driven element is fed independently. Thus, no feeding network has been included in the design of the large array. Figure 3-32 shows the full-wave simulated pattern for the boresight and steered configurations. The maximum scanning angle achieved with the 9-element array is 70 degrees on the E-plane and 73 degrees on the H-plane. In boresight the cross-pol level is below 23 dB while in the maximum scanning configuration is below 19 dB. The simulated boresight gain is about 14 dB corresponding to an aperture efficiency of 43%. The simulated gain when scanning to -70 degrees is about 11 dB. The use of an interleaved triangular lattice also results in

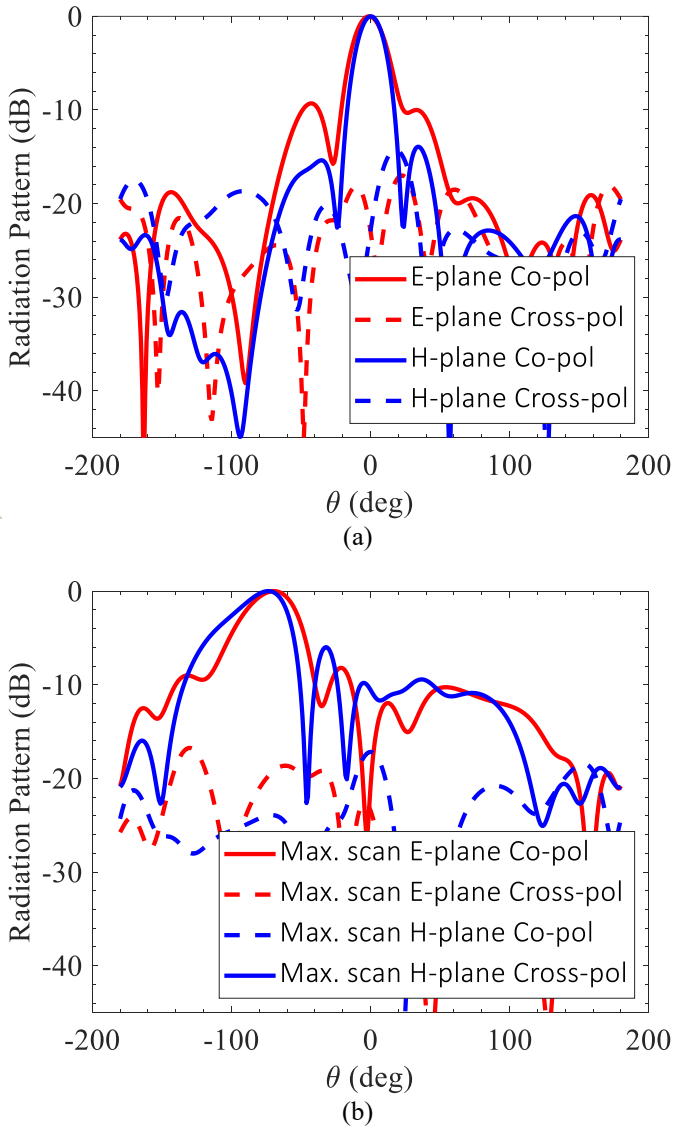

Figure 3-32 Boresight a), and b) steered E-plane and H-plane large array patterns.

a higher isolation between the subarrays. As depicted in Fig. 3-33, the isolation between the driven element located at the center of the large array, port 5, and the other driven elements is about -16 dB at 20 GHz.

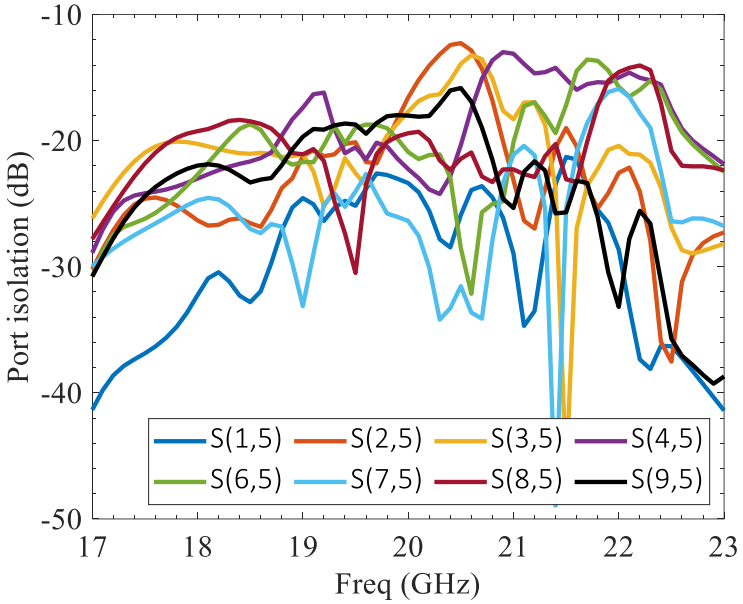

Figure 3-33 Isolation between the subarray n° 5 and the other subarrays.

Chapter 4: Transmitarray antennas

4.1 TRANSMITARRAY ANTENNA CONCEPT

Transmitarray antennas represent an innovative and versatile class of antennas that have garnered significant attention in the field of wireless communications and satellite systems in the last decades. This technology combines the favourable features of optic theory and antenna array techniques, leading to a low profile conformal design with high radiation efficiency and versatile radiation performance [65]. All these features make transmitarray particularly appealing for applications where size, weight, and mechanical complexity are critical factors. As shown in Fig. 4-1 a transmitarray antenna consists of an illuminating feed source and a flat transmitting surface. The feed position and pattern must be properly calculated to have the maximum aperture efficiency, which is the result of a compromise between the illumination and spillover efficiency. The basic principle behind transmitarray antennas involves the use of a flat surface with an array of sub-wavelength elements that can be individually controlled to manipulate the phase of the transmitted electromagnetic waves. This control over the phase enables precise steering of the antenna beam without the need for physically reorienting the entire structure.

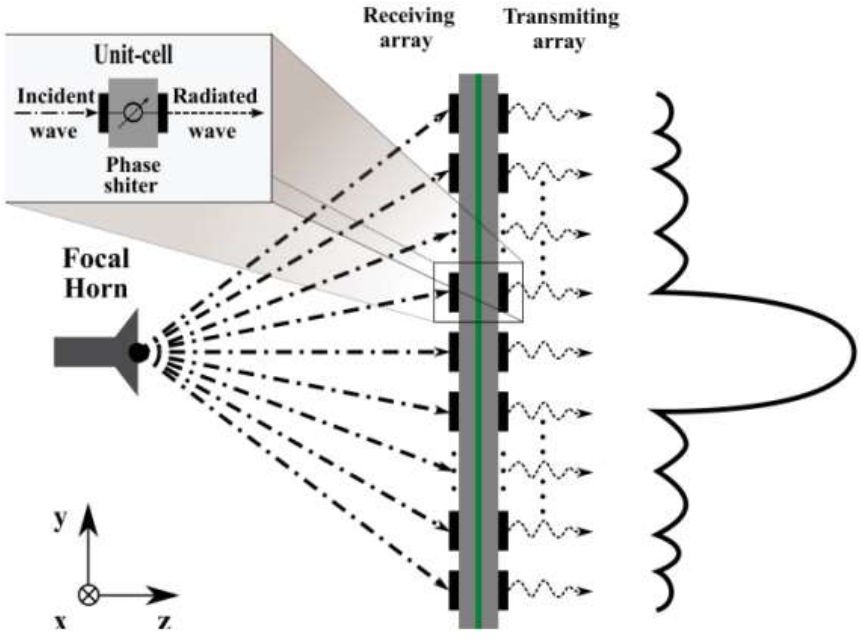

Figure 4-1 Transmitarray architecture [66].

4.1.1 Phase distribution on transmitarray aperture

In the design of a transmitarray the antenna elements are assumed to be situated in the far-field region of the feed source, typically positioned along the symmetry axis of the transmitarray surface. Under this assumption, the electromagnetic field reaching each transmitarray element at a specific angle can be locally treated as a plane wave. The phase of the incident wave is proportional to the distance from the phase center of the feed source to each element. The transmission phase of each transmitarray element is properly set to compensate the spatial phase delay from the feed to the transmitarray aperture, this allows to direct the beam in the desired direction. The transmission phase ψ_i for the i^{th} element is given by the following formula [66]:

$$\psi_i = k\,(R_i - \vec{r}_i \cdot \hat{r}_0) + \psi_0 \tag{4.1}$$

where k is the propagation constant in free space, R_i is the distance between the phase center of the focal source and the i^{th} element, $\vec{r}_i$ is the position vector of the i^{th} element and $\hat{r}_0$ is the beam direction. The parameter ψ_0 is a constant phase that indicates that a relative transmission phase rather than the absolute one is required for the design of the transmitarray [65]. Figure 4-2 shows an example of phase distribution for a 14x14 elements rectangular aperture transmitarray with a focal length to diameter ratio *F/D* = 0.65. After establishing the necessary transmission phase for each element across the transmitarray aperture, the corresponding element dimensions are derived by

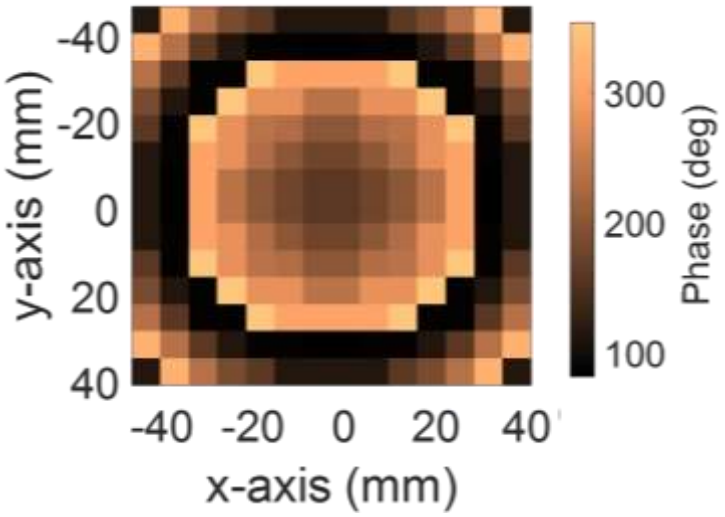

Figure 4-2 Example of the required phase distribution in a square transmitarray aperture [68].

referencing the transmission phase versus element dimension curve. This curve is typically obtained through a comprehensive electromagnetic wave analysis of the unit cell.

4.1.2 Unit-cell analysis

The transmitarray unit-cell plays a pivotal role in the overall functionality of the transmitarray antenna. Serving as the fundamental building block, the unit-cell is responsible for manipulating the incident electromagnetic wave into a desired phase and amplitude distribution across the antenna aperture. Through careful design and analysis, the unit-cell determines the required transmission phase for effective beamforming. The unit-cell's characteristics, including its geometry and electromagnetic properties, are essential factors in establishing the overall performance of the transmitarray antenna. The transmitarray unit-cell is usually analysed and simulated in a periodic environment to take into account the interactions between adjacent unit-cells. An example of transmitarray unit-cell simulation setup is

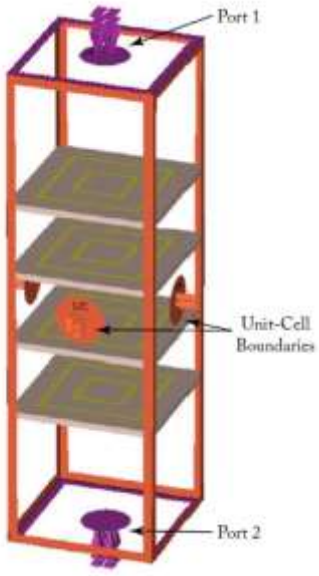

Figure 4-3 Simulation setup of a transmitarray unit-cell [65].

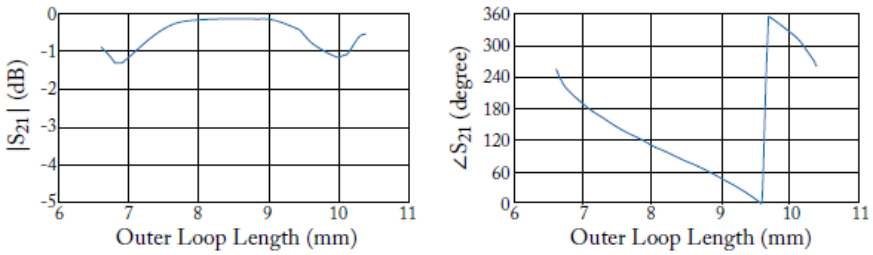

Figure 4-4 Unit-cell transmission coefficient.

depicted in Fig. 4-3. The phase of the transmitted wave is controlled by varying the geometrical dimension of the unit-cell while keeping the transmission losses (TL) as low as possible. The transmission coefficient of the unit-cell depicted in Fig. 4-3 is reported in Fig. 4-4, as shown the unit-cell exhibits a phase range of 360 degrees within a maximum insertion loss of 1.3 dB.

4.1.3 Comparison with other high gain antenna technologies

Transmitarrays, characterized by their planar structures with individually controlled elements, offer distinct advantages over conventional high-gain antennas such as parabolic reflectors and phased arrays. Unlike parabolic reflectors, transmitarrays eliminate the need for bulky mechanical components, thereby reducing the overall weight and complexity of the system. Both phased array and transmitarray are planar and compact solutions with the feature to allow individual control of the elements. The most significant difference between phased array and transmitarray is the feeding mechanism: the planar phased array relies on a feeding network, whereas the transmitarray utilizes a space feeding source. As well known, feed networks are lossy structures and complex to design, this limits the field of application of phased array especially in scenarios involving large aperture or high frequencies. Moreover, transmitarrays provide the capability for beam shaping and steering without the phase quantization limitations associated with phased arrays. This attribute imparts flexibility and adaptability to transmitarrays, making them particularly appealing for applications requiring dynamic beam control. Despite these advantages, transmitarrays face challenges, including losses associated with the unit cells and beam scanning limitations. In comparison to phased arrays, transmitarrays often exhibit reduced scanning ranges, necessitating careful consideration of the specific application requirements. As research in this field progresses, the comparative analysis of transmitarray antennas against other high-gain technologies contributes valuable insights into the design considerations and trade-offs inherent in the pursuit of advanced antenna systems.

4.2 TRANSMITARRAY ANTENNA DESIGN TECHNIQUES

Various methodologies are employed in the design of transmitarray antennas. Three main approaches can be distinguished:

1) receiver-transmitter approach;
2) metamaterial/transformation techniques;
3) frequency selective surfaces (FSS).

4.2.1 Receiver-transmitter approach

In the receiver-transmitter approach the transmitarray unit-cell consists of two radiating elements, one acting as a receiver and one acting as a transmitter. The receiver and transmitter elements are interconnected through via holes and transmission lines. The phase of the transmitted wave can be manipulated through varying the geometry of either the receiving or transmitting element or the coupling between them. Figure 4-5 shows two examples of receiver-transmitter based transmitarray unit-cell reported in [67] and [68] respectively, in both cases the phase control is realized by rotating the transmitting element.

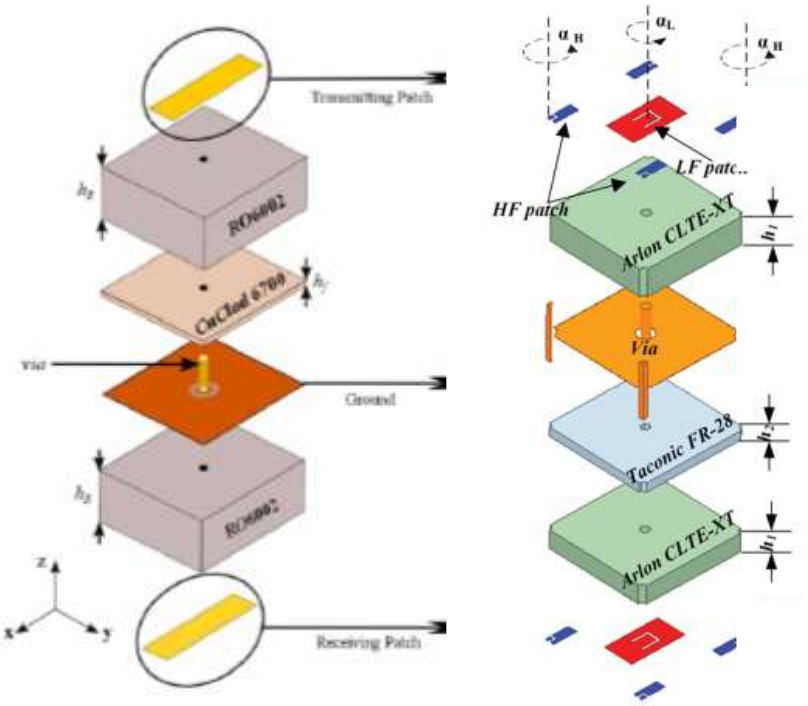

Figure 4-5 Examples of receiver-transmitter transmitarray unit-cells [67], [68].

4.2.2 Metamaterial/transformation approach

The metamaterial/transformation technique represents an innovative approach that leverages metamaterial principles and transformative strategies to achieve the control over electromagnetic wave propagation. By incorporating metamaterial elements into the transmitarray structure, unique electromagnetic properties can be engineered, enabling precise control of phase and amplitude at a subwavelength scale. Additionally, transformation techniques, such as coordinate transformations or conformal mapping, are employed to mold the physical structure of the transmitarray in ways that facilitate desired wavefront manipulations. This combined approach allows for the creation of transmitarrays with unconventional shapes and functionalities, surpassing the limitations of traditional designs. Examples of this approach are reported in [69], [70], [71], [72] where the element phase is controlled by varying the effective substrate permittivity and permeability.

4.2.3 Frequency selective surfaces (FSS)

Frequency Selective Surfaces (FSS) have become integral components in the design and optimization of transmitarrays, contributing significantly to the manipulation of electromagnetic waves for enhanced performance. These surfaces are engineered arrays of subwavelength elements that exhibit selective frequency-dependent responses, enabling precise control over the transmission, reflection, and absorption of electromagnetic waves. In the context of transmitarray design, FSS plays a pivotal role in tailoring the spectral characteristics of the antenna structure, allowing engineers to sculpt the desired beam patterns and control the phase and amplitude of the transmitted waves. The incorporation of FSS into transmitarrays facilitates the creation of antennas with improved efficiency, reduced sidelobes, and enhanced beam-shaping capabilities. The versatility of FSS enables its application across a spectrum of frequencies, making it suitable for a variety of communication and sensing systems. Ongoing research in FSS for transmitarray design explores innovative materials, reconfigurable FSS structures, and advanced computational modeling techniques, promising further advancements and expanding the horizons of this technology in the evolving landscape of antenna engineering.

Multilayer frequency selective surfaces (M-FSS)

In the transmitarray antennas based on FSS architecture the phase compensation cannot be achieved by only one layer. Therefore, multiple FSS can be stacked together to extend the capabilities of the antenna, Fig. 4-6. The multi-layer frequency selective surfaces (M-FSS) arrangement enhances the transmitarray ability to precisely manipulate the phase of transmitted waves, allowing for more flexible control and improved overall performance. In [73] a study about the transmission phase limit of multi-layer frequency selective surfaces has been carried out. It is demonstrated that the phase range of a M-FSS depends on several parameters: the number of layers, separation between the layers and, the substrate between the layers.

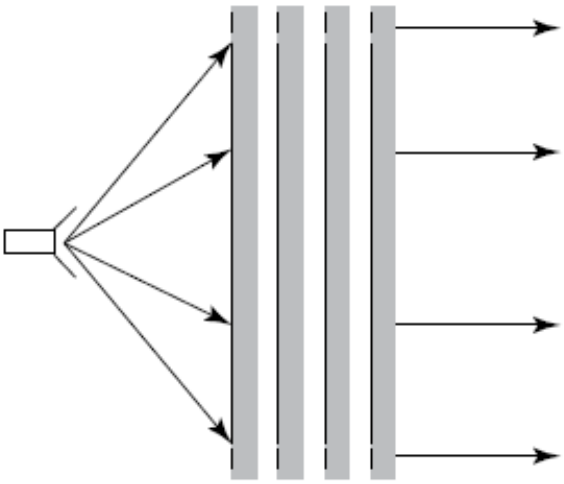

Figure 4-6 M-FSS based transmitarray structure [65].

Single-layer FSS

A single layer frequency selective surface with a conducting element can be seen as a two-port device [74]. Considering the layer illuminated on both sides, it is possible to express its scattering matrix as follows:

$$\begin{bmatrix} \frac{E_1^-}{E_2^-} \end{bmatrix} = \begin{bmatrix} S_{11} & S_{12} \\ S_{21} & S_{22} \end{bmatrix} \begin{bmatrix} \frac{E_1^+}{E_2^+} \end{bmatrix} \tag{4.2}$$

where $E_1^{\pm}$ and $E_2^{\pm}$ are the incident and reflected plane waves at the left and right sides of the terminal plane, respectively. The scattering matrix of the layer is represented with $[S]$. If the FSS layer is symmetric, reciprocal, and lossless, the phase difference

between the reflected and transmitted waves of the conducting layer is $\pi/2$ [73], Moreover, if the higher harmonics of the FSS layer are relatively small so that they can be neglected, the relation between the transmission and reflection coefficient is:

$$S_{21} = 1 + S_{11} \tag{4.3}$$

this allows to express the relation between the transmission magnitude and transmission phase as follows:

$$|S_{21}| = \cos(\angle S_{21}) \tag{4.4}$$

A more insightful comprehension of this relationship can be achieved by representing it in a polar diagram, Fig. 4-7. On the polar diagram, the transmission coefficient is represented as a circle, the dashed green and red circles represent the -1 dB and -3 dB transmission magnitude limits. The solid blue circle instead represents the transmission coefficient magnitude versus the transmission coefficient phase. As can be deducted from the plot the maximum phase range that can be achieved with a single layer FSS is 54 and 90 degrees within 1 dB and 3 dB of transmission losses, respectively. Numerical demonstrations of single layer and multi-layer FSS transmission phase limits can be found in [73].

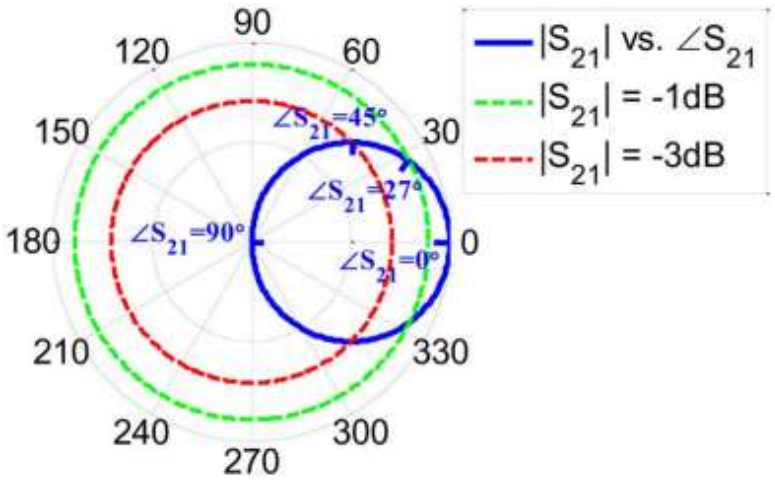

Figure 4-7 Transmission coefficient amplitude and phase of a single layer FSS [75].

Double-layer FSS

A double-layer FSS can be seen as comprising two conducting elements separated by a substrate. If the two conducting layers are identical their transmission phases are the same. The transmission coefficient response of the double-layer FSS can be calculated as a cascade of two single-layer FSS:

$$s_{11}^{C} = \frac{s_{11}^{2} s_{12}^{1} s_{21}^{1}}{1 - s_{11}^{2} s_{22}^{1}} + s_{11}^{1} \tag{4.5}$$

$$s_{12}^{C} = s_{21}^{C} = \frac{s_{21}^{1} s_{21}^{2}}{1 - s_{11}^{2} s_{22}^{1}} + s_{11}^{1} \tag{4.5}$$

$$s_{22}^{C} = \frac{s_{22}^{1} s_{12}^{2} s_{21}^{2}}{1 - s_{11}^{2} s_{22}^{1}} + s_{22}^{1} \tag{4.5}$$

where $[S^1]$ is the scattering matrix of the first layer, $[S^2]$ is the scattering matrix of the second layer and, $[S^C]$ is the scattering matrix of the cascaded two layers. The scattering matrix of the double-layer FSS can be so computed by repeatedly cascading the S-parameters of the conducting layer and the S-parameters of the separation substrate defined as follows:

$$s_{11} = s_{22} = \frac{\Gamma\left(1 - e^{-j2\beta L_d}\right)}{1 - \Gamma^2 e^{-j2\beta L_d}} \tag{4.6}$$

$$s_{12} = s_{21} = \frac{\left(1 - \Gamma^2\right) e^{-j2\beta L_d}}{1 - \Gamma^2 e^{-j2\beta L_d}} \tag{4.7}$$

where for normal plane wave incidence

$$\Gamma = \frac{1 - \sqrt{\varepsilon_r}}{1 + \sqrt{\varepsilon_r}} \tag{4.8}$$

$$\beta = \frac{2\pi\sqrt{\varepsilon_r}}{\lambda_0} \tag{4.9}$$

The scattering matrix of the separation substrate is a function of the dielectric permittivity ε_r and the substrate thickness L_d, while the scattering matrix of the

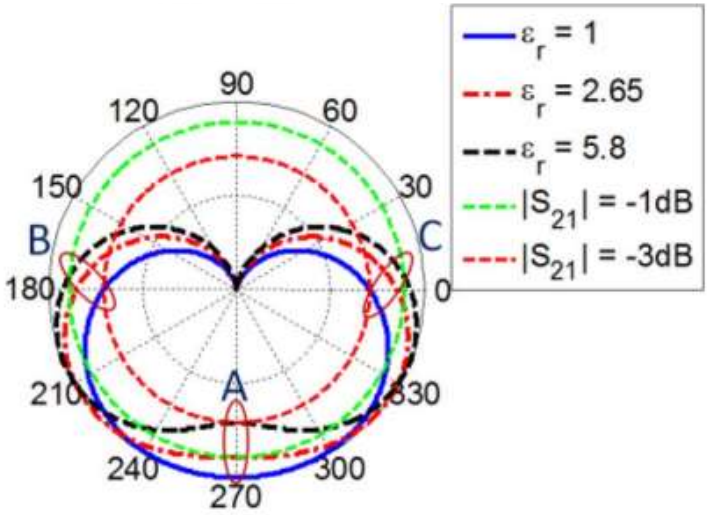

Figure 4-8 Transmission coefficient amplitude and phase of a double-layer FSS for different dielectric permittivity and fixed dielectric thickness of $\beta L_d = 90°$ [75].

conducting layers is a function of the transmission coefficient phase. Figure 4-8 shows the transmission coefficient magnitude and phase for a double-layer FSS for different substrate permittivity while fixing the dielectric electrical thickness to $\beta L_d = 90°$. Figure 4-9 illustrates the transmission coefficients for various substrate thicknesses while maintaining a constant permittivity. Examining Fig. 4-8 reveals that increasing the substrate permittivity while maintaining a constant electrical thickness amplifies the transmission coefficient magnitude within specific phase ranges (around points B and C), yet diminishes it within another phase range (around point A). The same behaviour is obtained while varying the substrate thickness and fixing the permittivity, Fig. 4-9. The maximum transmission phase range that can be obtained from a double

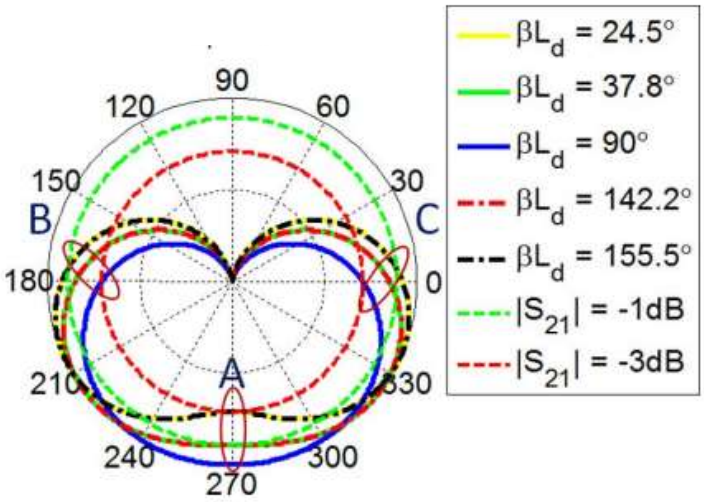

Figure 4-9 Transmission coefficient amplitude and phase of a double-layer FSS for different dielectric thicknesses and fixed dielectric permittivity ε_r=1 [75].

layer configuration within 1 dB and 3 dB of transmission losses are 170 and 228.5 degrees, respectively. Two conducting layers are still not enough for the design of a transmitarray, where a phase range of 360 degrees is needed.

Triple-layer FSS

The scattering parameters of a triple-layer configuration ca be computed by concatenating two additional sections, integrating the dielectric substrate and the third conductor layer into the double-layer setup. All conducting layers are assumed to be identical, as are the dielectric layers. Figure 4-10 shows the transmission coefficient for the triple-layer configuration achieved by manipulating the transmission coefficient phase of the three conductor layers. With a fixed substrate electrical length of 90 degrees and a permittivity equal to 1, the maximum phase range within 1 dB and 3 dB of transmission losses is 266 and 317 degrees. Achieving a complete phase range of 360 degrees with transmission losses within 3 dB requires a substrate with a minimum permittivity of 2.5. More layers can be added to the FSS to increase further the phase range and avoid higher order mode coupling between the layers. In [75] a quad-layer FSS transmitarray has been reported showing impressive performance, a phase range of 360 degrees has been achieved within 1 dB of transmission losses. In this design, the four conducting layers are separated through air gaps mitigating transmission losses. However, it results in a bulkier structure, characterized by a total thickness of $0.75\lambda_0$.

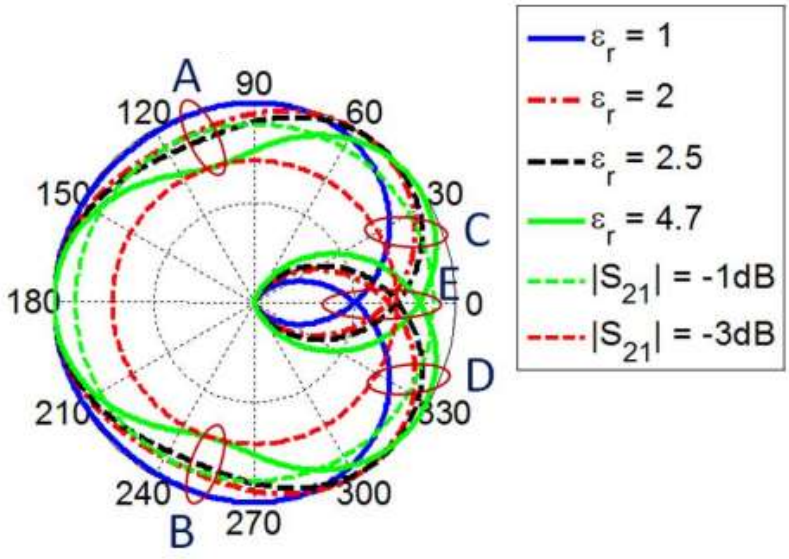

Figure 4-10 Triple-layer FSS transmission coefficient response for different substrate permittivity [75].

4.3 DUAL-BAND TRANSMITARRAY ANTENNAS

K/Ka-band satellite communications are based on bidirectional links covering the range of 17.7-21.2 GHz for downlink (DL) and 27-31 GHz for uplink (UL), leading to an increase in research for the investigation of new solutions for dual-band antenna systems. In line with this trend, various antenna designs have been proposed in literature over the past few years, including several examples of dual-band Reflectarray (RA) and Transmitarray (TA) antennas. RA and TA gained popularity due to their advantages over traditional array antennas and reflectors. They can provide high gain without the need for complex feeding networks or bulky structures, and their manufacturing process is cost-effective. Compared to RA, where the feed is in front of the antenna aperture, TA antennas offer higher efficiency avoiding feeding blockage losses. Research studies on TA are rapidly evolving, especially in view of their possible application for K/Ka SatCom systems where they can play a crucial role in ground terminals and in other nodes of the non-terrestrial-network. Similarly to what happens in reflectarray antennas, the most relevant challenge faced by dual-band TA is the creation of unit cells that can independently control their transmission phase in both frequency bands while maintaining the lowest possible insertion loss. Dual-band TA antennas are typically implemented using interleaved radiating elements, each of which is designed to manipulate wave propagation in one of the operating bands. In the context of K/Ka SatCom antenna systems, the radiators must also be dual-polarized to support circular or dual-linear polarization. In the next section a state of the art of dual-band transmitarray antenna is provided.

4.3.1 Dual-band transmitarray antenna: state of the art

The prevalent methods for designing dual-band transmitarray antennas include the multi-layer frequency selective surface (M-FSS) approach and the receiver-transmitter architecture approach. Dual-band transmitarray designs based on M-FSS are reported in [35], [76], [77], [78], [79], [80], [81]. In [76] and [79] a triple-layer dual-polarized M-FSS based on slot radiating elements separated by air gaps is used to achieve an unit-cell phase range of 300 degrees within 3 dB of transmission losses. The maximum aperture efficiency reached is 10% and 38%, respectively. In [77], metallic loops are employed instead of slots, yielding a phase range of 300 degrees within 2 dB of

transmission losses, instead of 3 dB. This results in an enhanced maximum efficiency of 46%. A dual-band orthogonally polarized M-FSS is presented in [80] with three conducting layers of printed dipoles reaching a phase range of 360 degrees. As demonstrated in the previous section, incorporating additional layers results in broader phase ranges and lower transmission losses. In [81] four conducting layers separated through airgaps are employed obtaining a maximum aperture efficiency of 53% for linearly polarized TA. A five-layer M-FSS is introduced in [78], the conducting elements are printed on a dielectric substrate separated by airgaps. A phase range of about 360 degrees is obtained within 3dB of transmission losses, the maximum aperture efficiency is 34%. In [35] a general method to reduce the complexity of dual-band transmit array design is demonstrated by using a seven-layer M-FSS. The key benefit of employing Multi-layer Frequency Selective Surfaces (M-FSS) in transmitarray antenna design lies in the capability to attain an extensive phase range with minimal transmission losses, leading to enhanced antenna efficiency. However, a notable drawback associated with M-FSS-based transmitarray antennas is the augmented thickness, manufacturing costs, and reliability concerns due to a heterogeneous stack-up, which can be as thick as 0.55 to 1 wavelength (λ_0).

In all the aforementioned M-FSS based transmitarray, the conducting layers are separated by airgaps or thick dielectric substrates. In contrast, the transmitter-receiver transmitarray architecture approach offers a low-cost and compact solution, which eliminates the requirement for air gaps or thick substrates. It employs an array of receiving elements that are interconnected with another array of transmitting elements, all realized on a single printed circuit board (PCB). This results in a more compact design compared to the M-FSS approach but, on the other hand, it requires vertical interconnections, and it has not been proved yet for dual-band dual-polarized configurations. For example, in [82] a K/Ka single bit transmitarray is proposed using orthogonal polarizations in the two bands. This configuration operates as a dual-linearly polarized TA, and it requires five metal layers with metallized via holes. In order to reduce to three the number of metal layers, another example of the same configuration is reported in [67] where an interleaved arrangement is employed. Besides being both examples dual-linearly polarized, their efficiency is limited mainly because of the one-bit phase range resolution. Moreover, for many applications such as satellite communications, they need to be combined with LP-to-CP polarization converter [83]. Receiver-transmitter architectures with 360 degrees phase range are

reported in [84] and [68] for orthogonally and circularly polarized dual-band transmitarray in Ku/K band. Despite offering an improved aperture efficiency of 32 and 55%, the effectiveness of these configuration has only been proved under conditions where the difference between the two operating bands is limited to 2 and 6 GHz.

4.4 LOW PROFILE DUAL-BAND DUAL-POLARIZED TRANSMITARRAY BASED ON M-FSS

In this thesis, a novel multi-layer frequency selective surface (M-FSS) cell topology is introduced for the dual-band dual-polarized operation at frequencies of 20 GHz and 30 GHz [85]. This cell topology is found to possess additional and unique advantages over the existing solutions in the field as it is the firstly reported dual-band dual-polarized M-FSS which does not require air gaps or thick substrates. Yet it preserves the independency of control at the two frequency bands. Each TA cell is designed as a dual-band passband filter, and it is integrated onto a single printed circuit board with a total thickness of $0.24\lambda_0$, where λ_0 is the free space wavelength at 30 GHz. The validation demonstrator was designed to cover the K/Ka band SatCom frequencies. The proposed concept is based on an interleaved lattice employing slot loaded stacked patch antennas coupled through crossed slots. Thanks to this solution, the phase of the transmitted field can be controlled within a 300 degrees phase range.

4.4.1 Single-band single-polarized M-FSS TA unit-cell

The generalized model of the single-band single-polarization M-FSS TA cell is reported in Fig. 4-11. The configuration is structured as a cascade of *N* metal layers, interleaved by *N-1* dielectrics that have identical characteristics and thickness. Specifically, the dielectric thickness is equal to *d* while the relative permittivity and loss tangent are equal to 3.66 and 0.004, respectively. The metal layers with an odd index in the proposed design (L_1 L_3, ...) contain a patch antenna. The layers with even index ($L_2, L_4, \dots$) serve as ground planes where a rectangular slot is etched to provide coupling between two adjacent patches. The multilayer structure acts as a pass-band filter where each patch is a resonator. Extending the approach proposed in [86], the M-

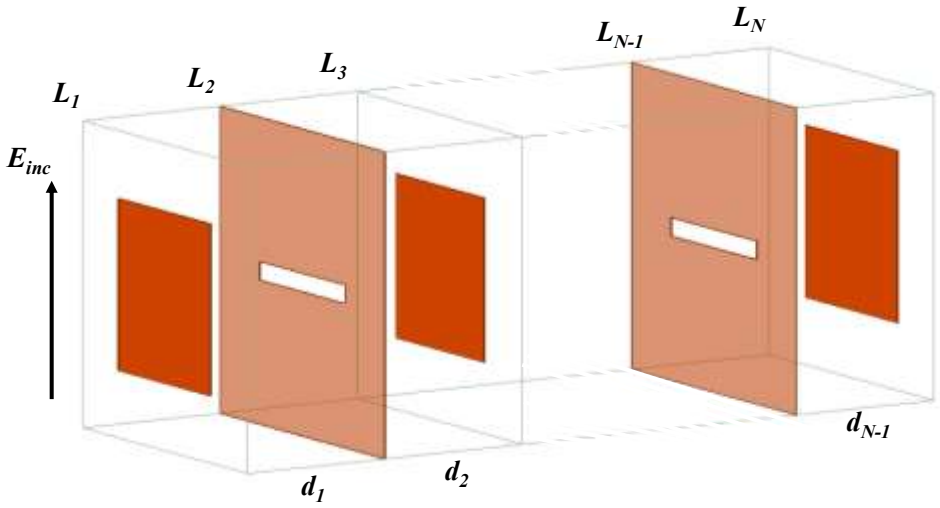

Figure 4-11 N-layers single-band single-pol TA unit-cell configuration.

FSS unit cell can be analyzed using the simplified equivalent circuit reported in Fig. 4-12-a where dielectric and conductor losses are not taken into account. Each patch can be modelled as an L-C tank whereas the slots are represented through a coupling capacitor, C_S. This circuit thus behaves as a capacitive coupled bandpass filter [87]. In a first assumption, the values of the lumped components remain identical for all layers. The application of an equivalent circuit was initially undertaken to determine the relationship between the number of layers and the transmission phase range. Beginning with the elementary configuration comprised of two resonant elements (N=3), the analysis was extended up to four resonators (N=7). The lumped circuit values were estimated following the approach given in [87] under the assumption of a Chebyshev response with a 2 dB ripple and a 6 GHz bandwidth. Table 4-1 provides the circuit component values for N=3, 5, and 7, while Fig. 4-12-b displays the transmission coefficient amplitude and phase. It is noteworthy that the transmission coefficient phase response within the transmission bandwidth increases from 200 to 470 degrees. As expounded in [88], the phase range is associated with the final system bandwidth. Hence, the application at hand warrants a configuration with *N*=5 to meet the desired requirements. Upon determination of the desired number of layers, an analysis of the

Table 4-1 Equivalent circuit parameters values for different architectures.

N° Layers	C_P (fF)	L_P (nH)	C_S (fF)
3	122	0.4	32
5	131	0.38	23
7	122	0.38	25*

*In the 7-layers architecture the series capacitance between the layers L_3 and L_5 is 19 fF.

proposed circuit is conducted to assess its viability for TA applications. Specifically, the focus is on ascertaining how the transmitted field phase can be manipulated. Various techniques can be employed to control the phase. The predominant approach, as documented in the literature, involves varying the resonator response thought the variation of its resonant frequency (i.e. L_P or C_P). As reported in Fig. 4-13-a, a change of C_P while having L_P=0.38 nH and C_S=22 fF provides a phase range of about 270 degrees while the pass band remains approximately the same. An alternative method is to maintain the resonator fixed and to change the coupling capacitor only, C_S. In this case, Fig. 4-13-b, the achieved phase range is 220 degrees, and the pass-band profile is altered. The effect of a combination of both techniques is reported in Fig. 4-13-c where a phase range of 320 degrees is obtained.

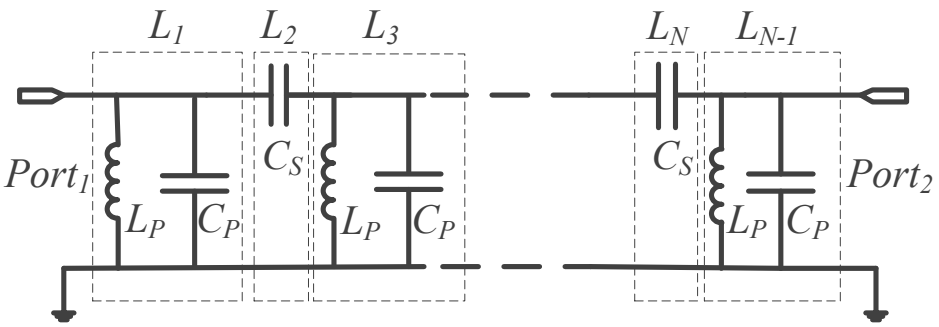

(a)

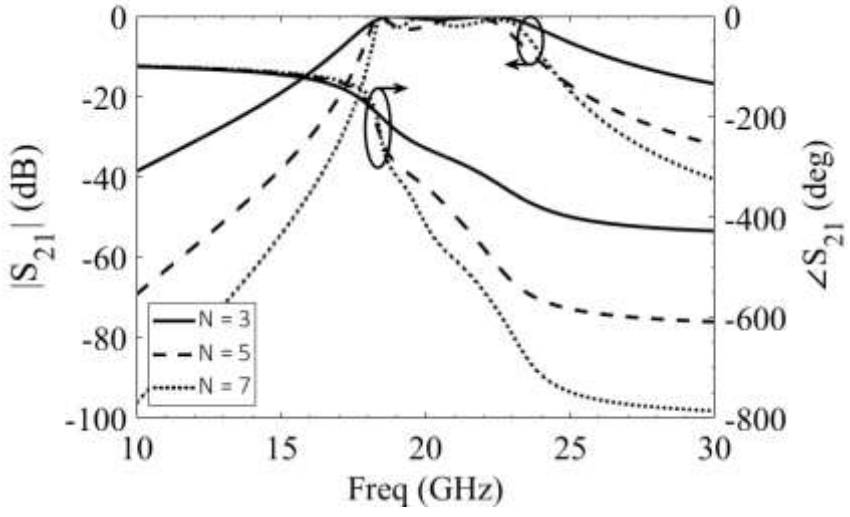

(b)

Figure 4-12 Equivalent circuit model of an N-layers unit-cell: a) equivalent circuit; b) transmission coefficient response for different number of layers.

Although the implementation of the circuit Fig. 4-12-a can be accomplished directly using the geometry reported in Fig. 4-11, an alternative approach based on square patches loaded with a rectangular slot (Fig. 4-14) was favoured, given the aim of expanding the model into a dual-band dual-polarized cell. As reported in [89], the introduction of a rectangular slot having width W_S and length L_{PS} onto a patch antenna

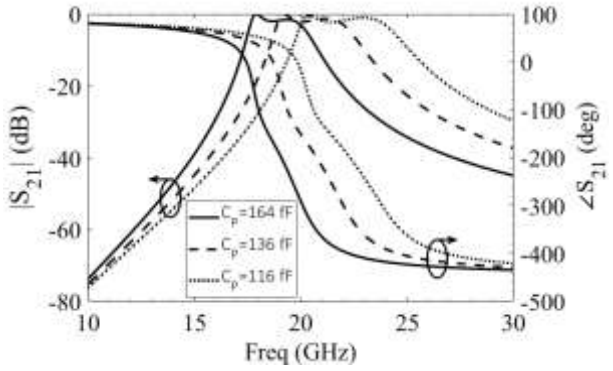

(a)

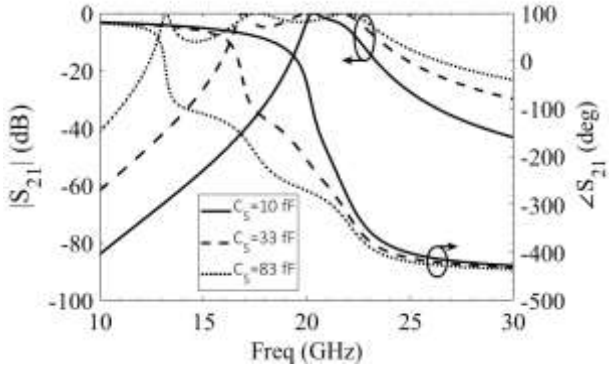

(b)

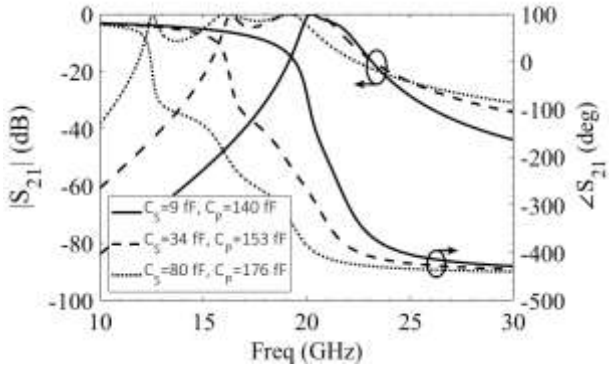

(c)

Figure 4-13 Transmission coefficient response varying the resonator frequency by manipulating C_P while having L_P=0.38 nH and C_S=22 fF a), transmission coefficient response varying the coupling capacitor, C_S, while having C_P=136 fF and L_P=0.38 nH b), transmission coefficient response achieved by varying both the coupling and the resonators capacitor (i.e. C_P and C_S) while having L_P =0.38 nH.

results in a capacitive load (affecting C_P) which allows to tune its resonant frequency by only manipulating the slot's geometry. As it will be shown, this approach allows to keep fixed the patch length, L, whilst enabling an effective implementation of the dual-band dual-polarized TA cell by using an interleaved arrangement. The circuit of Fig. 4-12-a can be converted into the geometry of Fig. 4-14 using different procedures. The proposed design methodology involves the following steps which were carried out using the full-wave simulator Ansys HFSS [90]. Once the dielectric characteristics are defined, the first step is defining the geometrical parameters of the slot-loaded square patch. Analytical relationships between the patch's geometry and its corresponding circuit can be obtained from [89], serving as a preliminary reference for the full-wave simulation. Among the different combinations of patch and slot length, the ideal arrangement should be determined based on the capability to attain the maximum phase range by manipulating solely the slots' length, namely L_{PS} and L_S. Besides, there are various approaches available for determining the geometry of the coupling slot. The interactions of the different elements of the M-FSS TA cell create mutual dependences which can be simplified by fixing some geometrical relations.

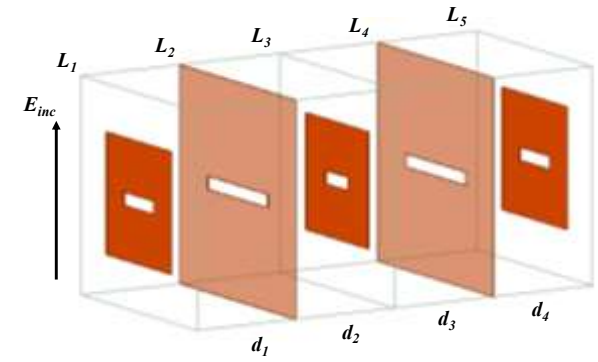

(a)

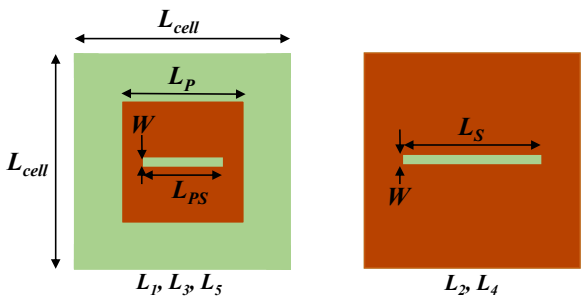

(b)

Figure 4-14 Single-band single-pol TA unit-cell configuration with N=5. Rectangular slots are etched on the patches to have an additional tuning element: a) 3-D geometry; b) top view and geometrical parameters.

To keep the control of the transmitted phase as simple as possible, the slots etched on the patch surface and the coupling slots are related as follows: the length of the slots loading the patches is set to be half of the length of the coupling slot, that is $L_{PS} = L_S/2$. As a result, each single-band linearly polarized M-FSS TA cell, Fig. 4-14-a, is regulated by a single parameter, governing its transmitted phase through alterations in both resonator frequency and coupling intensity. It is worth noticing that the resonators of the circuital model in Fig. 4-12-a are all identical. To emulate this behaviour in the M-FSS TA cell, the length of the patches located in the inner layers should undergo a slight tuning to make them resonate at the same frequency, despite the differences in the effective dielectric permittivity across the different layers.

Following the outlined design approach, a M-FSS TA cell was designed with N=5 having a center band frequency of 20 GHz. The PCB stackup comprises five metals layers and four identical dielectric substrates of 0.508 mm Rogers RO4350 with a relative permittivity of 3.66 and dielectric loss tangent of 0.004. Table 4-2 displays the relevant geometrical parameters of the single-band single-pol TA unit-cell. The variations of the transmission coefficient in amplitude and phase versus the slot length are reported in Fig. 4-15. Figure 4-16 presents a comparison between the equivalent circuit and full-wave simulated transmission coefficient. The latter approach was

Table 4-2 Key geometrical parameters of the single-band single-pol ta unit-cell.

Parameters	Value (mm)	Variables	Range (mm)
L_{CELL}	5.8	L_S	1.5-4
W	0.35	L_{PS}	0.75-2
H_D	0.508		
L_P	3.25*		

*For the patches of the inner layer (L3) L_{P20}=3.15

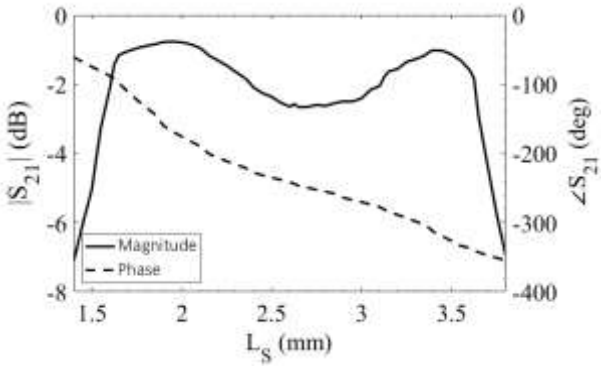

Figure 4-15 Full-wave simulations in infinite array of the M-FSS TA cell: transmission coefficient amplitude and phase with respect to slot length, L_S.

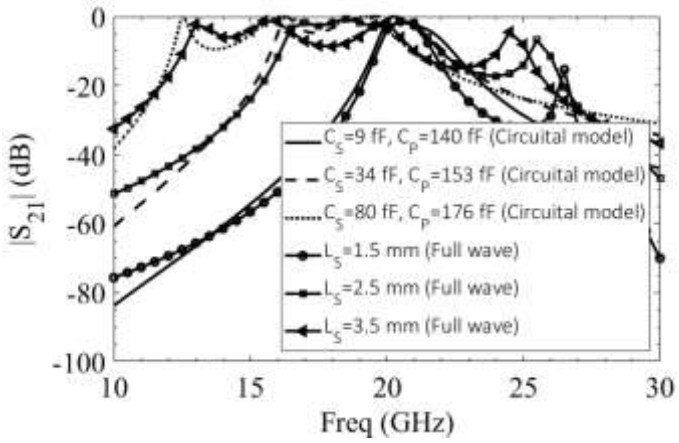

(a)

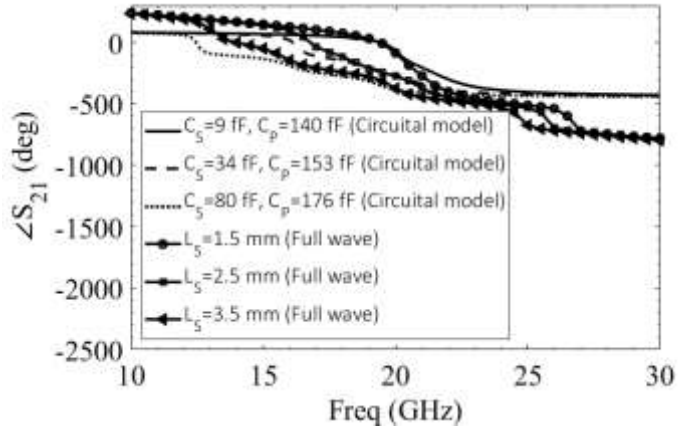

(b)

Figure 4-16 Comparison between the circuital model transmission coefficient response and simulated for three different slot lengths, a) magnitude and b) phase.

implemented in an infinite array setting. Simulated results are reported for three distinct configurations, representing the nominal configuration as well as the two extremes of the L_S range. Results reveal a good agreement between the two simulation techniques. Nonetheless, a key distinction between them pertains to the full-wave simulation's identification of a resonance at about 25 GHz. This behaviour, resulting from the periodicity effect [91], it is not captured by the equivalent circuit approach and it increases the phase range. The simulation results indicate a phase range of 300 degrees with transmission losses not exceeding 3 dB. Hence, the full-wave simulated phase range is in line with the ones predicted by the circuital model.

4.4.2 Dual-band dual-polarized M-FSS TA unit-cell

The single-band single polarized M-FSS TA cell geometry has been extended to achieve dual-band dual-polarized operation. To generate dual-polarization cross-

shaped slots are employed in place of the rectangular slots both for to load the patch and for coupling. As reported in [92], this technique gives an isolation between the vertical and horizontal polarization of about 30 dB. Such a level of isolation is adequate to control the two polarizations independently. In the present work, the transmitted field phase is equal for both polarizations, resulting in symmetrical slots.

Thanks to the good selectivity of the M-FSS TA cell presented in the previous section, concurrent operation across two distinct frequency bands can be obtained by interleaving the lower frequency cell with the higher frequency one. For the application at hand, the 20 GHz (DL) TA cell can be interleaved with four 30 GHz (UL) ones having the same configuration. Given the high frequency separation between the two bands, it is not difficult to optimize the patch geometry to have an isolation higher than 35 dB between the two bands. An advantage of the present design is that modifications to the patch outer perimeter are not required in order to

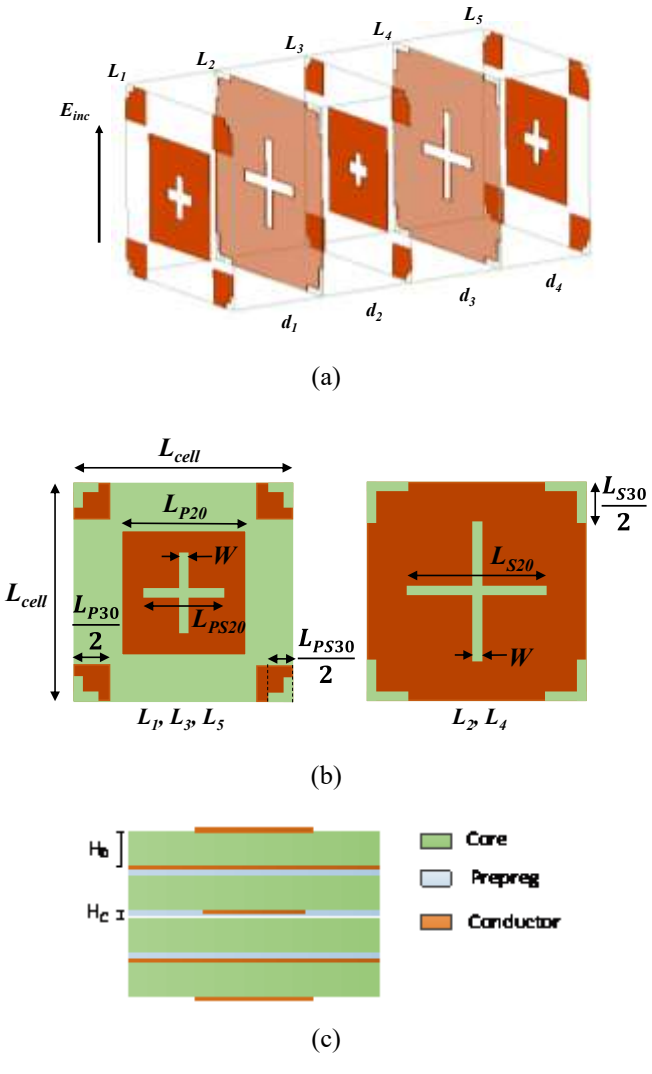

Figure 4-17 Dual-band transmitarray unit-cell architecture a), geometrical parameters b), and stackup c).

manipulate transmitted phase. As a result, cross-frequency coupling remains relatively stable during phase adjustment, thereby facilitating independent design of the TA cell for each frequency band. Figure 4-17 illustrates the dual-band dual-polarized configuration, while Table 4-3 presents all pertinent dimensions. The corresponding equivalent circuit is depicted in Fig. 4-18-a alongside the transmission coefficient response simulated using the circuital model and the full-wave analysis. The phase range within a 3 dB and 3.5 dB insertion loss is about 280 and 300 degrees, respectively. The amplitude and phase characteristics of the TA unit-cell as functions of the phase control parameters at 20 GHz and 30 GHz are presented in Fig. 4-19. The maximum phase error is 6 and 20 degrees at 20 and 30 GHz, respectively. The amplitude variations remain below 0.7 dB at both bands. Thereby, the two frequencies operate independently, as changes to L_{PS30} minimally impact the phase response at 20 GHz, while modifications to L_{PS20} similarly exert negligible influence on the cell response at 30 GHz. In transmitarray design, it is also essential to account for the sensitivity of unit-cell amplitude and phase to changes in the angle of incidence. Figure 4-20 depicts the transmission coefficient response for a range of angles of incidence. The transmission response of the unit-cell exhibits a degree of robustness up to an angle of incidence of 30 degrees. Alterations to the angle of incidence do not significantly affect the phase response at either 20 or 30 GHz. However, at 20 GHz, an attenuation in magnitude response occurs with increasing angle of incidence for L_{S20} values approximately 2.7 mm. At 30 GHz, a more pronounced sensitivity to the angle of incidence is observed at the extremes of L_{S30} range, resulting in a maximum reduction of approximately 2 dB. This heightened sensitivity, coupled with substrate and prepreg losses, accounts for the disparity in transmitarray efficiency between the 20 and 30 GHz frequency bands.

Table 4-3 Key geometrical parameters of the dual-band dual-pol ta unit-cell.

Parameters	Value (mm)	Variables	Range (mm)
L_{CELL}	5.8	L_{S20}	1.5-4
W	0.35	L_{S30}	1-2.1
H_D	0.508	L_{PS20}	0.75-2
H_P	0.1	L_{PS30}	0.5-1.05
L_{P20}	3.25*		
L_{P30}	2.1*		

*For the patches of the inner layer (L3) L_{P20}=3.15 mm and L_{P30}=1.9 mm.

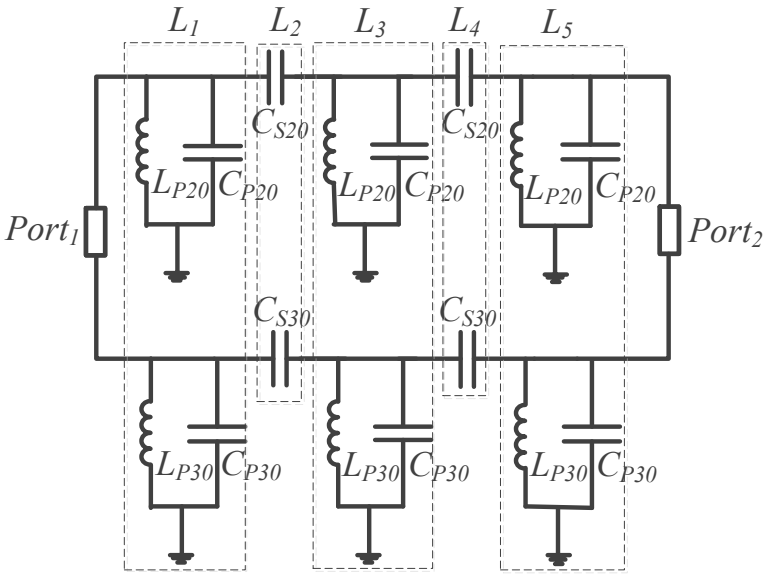

(a)

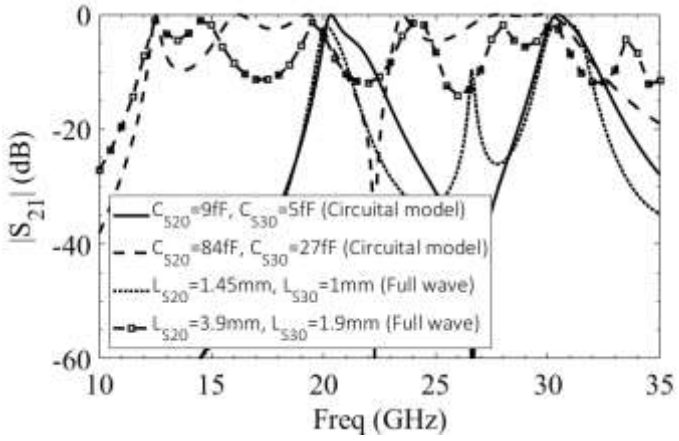

(b)

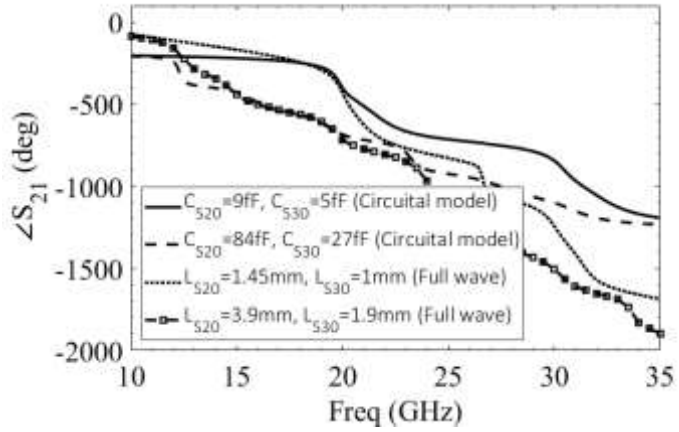

(c)

Figure 4-18 Dual-band unit-cell equivalent circuit model a), and transmission coefficient response: amplitude b) and phase c). (CR20=135 fF, LR20=0.38 nH, CR30=104 fF, LR30=0.23 nH)

To validate the dual-band dual-polarized M-FSS TA cell proposed in the previous section, a 421-element prototype was designed, prototyped and experimentally characterized. Each TA consists of two subarrays: an UL array comprising 196 elements arranged in a 14-by-14 square lattice, and a DL array containing 225 elements organized in a 15-by-15 square matrix, Fig. 4-21. The total physical dimensions of each prototype measure 87 mm × 87 mm, with a 10-mm extension along the edges to provide mechanical support. The prototype stack-up is reported in Fig. 4-17-c. Each dielectric layer includes a Rogers RO4350 slab having thickness 0.508 mm and a I-TERA MT 3313 prepreg layer which thickness is equal to 0.1 mm. A dual-polarized quad-ridged horn, RFecho ODPA-180400-20mm, covering both K and Ka bands is used to illuminate the TA. The E-plane HPBW of the feed at 20 GHz is 38.5 degrees while on H-plane is 50 degrees; at 30 GHz the HPBW is 27 and 37 degrees on E-plane

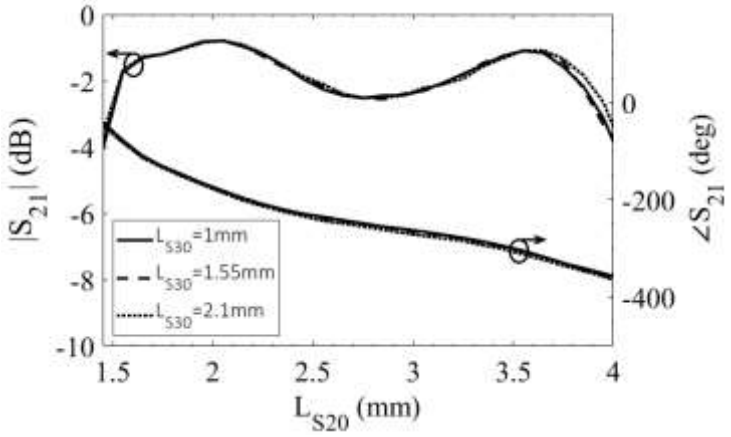

(a)

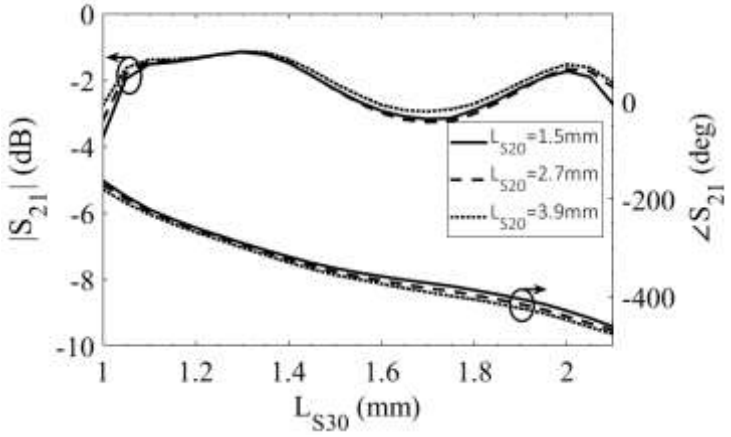

(b)

Figure 4-19 Simulated transmission response of the dual-band dual-polarized TA cell with respect to the phase control parameters at: a) 20 GHz; b) 30 GHz.

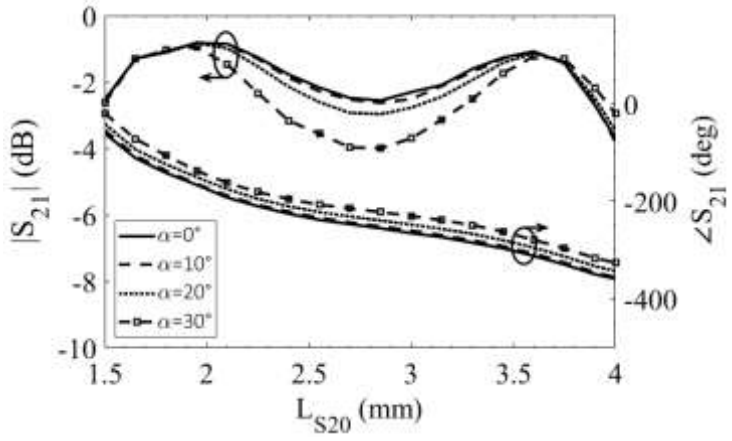

(a)

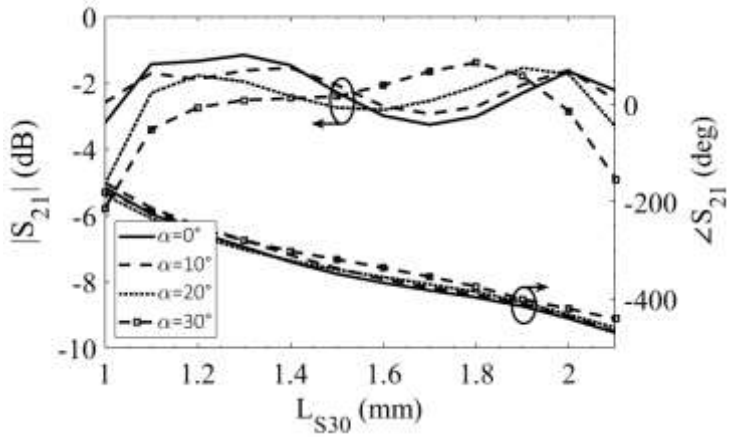

(b)

Figure 4-20 Unit-cell transmission coefficient response for different angles of incidence at 20 a) and b) 30 GHz.

and H-plane, respectively. The focal distance was optimized to attain an optimal balance between spill-over loss and illumination efficiency for both frequency bands. The TA design and optimization was performed using an in-house simulation tool developed following the approach described in [93]. An optimal focal distance of 80 mm was determined to yield the most favorable results, corresponding to a F/D ratio of 0.65. Such a selection resulted in an illumination level below -10 dB and −13 dB at the edges and corners of the TA, respectively. To calculate properly the focal distance the analytical method shown in [94] has been used. In this case, the pattern of each element has been modeled by a $cos(\theta)$ while the pattern of the feed has been modeled by $cos^{qE}(\theta)$ and $cos^{qH}(\theta)$ for E-plane and H-plane, respectively. At 20 GHz *qE=6* and *qH*=3 instead at 30 GHz *qE=10* and *qH=6*. Besides, a full-wave analysis [90] of the TA was also performed including the actual geometry of the dual-polarized feed.

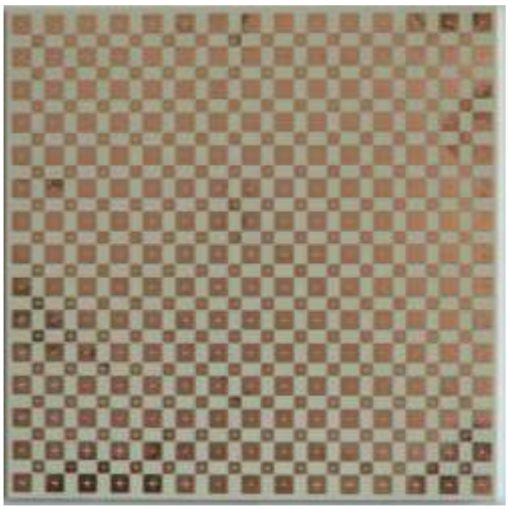

Figure 4-21 Top view of the dual-band dual-polarized M-FSS TA prototype.

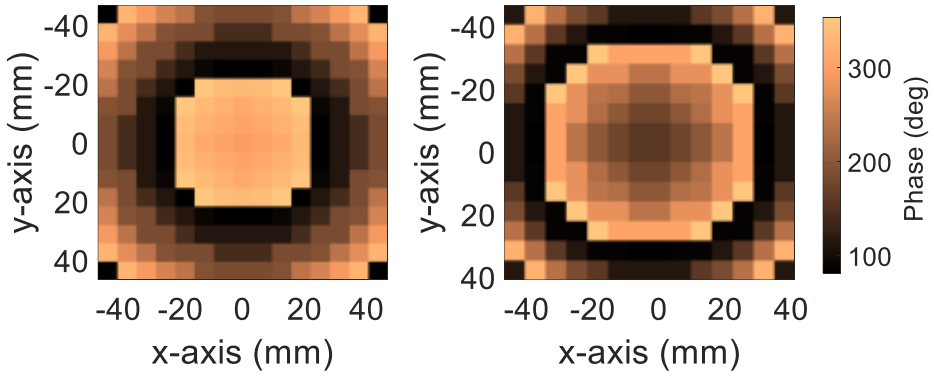

Figure 4-22 Phase distribution on the TA elements:a) DL array, and b) UL array.

The TA prototype was designed to have both beams pointing in the broadside direction. The phase distribution of each TA cell for the UL and DL frequencies is reported in Fig. 4-22.

The TA radiation performance in both UL and DL bands was measured in the anechoic chamber of the MAIC LAB at the University of Calabria, Fig. 4-23. Fig. 4-24 and 4-25 show the co- and cross-polar far field E-plane and H-plane radiation pattern at 20 and 30 GHz, respectively. Measured results are compared with full-wave and analytical simulations showing a good agreement. The results reveal that the measured side-lobe levels at 20 GHz are approximately -14 dB on the E-plane and -10 dB on the H-plane, while at 30 GHz, their levels are roughly equivalent to -14 dB and -13.5 dB on the E-plane and H-plane, respectively. The measured cross-polar field remains below -25 dB in both the DL and UL band. It has been also verified that lower side lobe levels, similar to the ones predicted by the analytical model, could be achieved by using two single-band feeds. The simulated and measured gain vs frequency is

Figure 4-23 Dual-band dual-polarized M-FSS TA prototype mounted in the receiving mast of the anechoic chamber available at the MAIC-LAB, at the University of Calabria, Italy.

shown is Fig. 4-26. The measured peak gain in the DL band is 20.64 dBi corresponding to an aperture efficiency of 27%. The -1 dB gain bandwidth is 1 GHz (5% at the center frequency). A peak gain of 22.8 dBi has been obtained in the UL band showing an

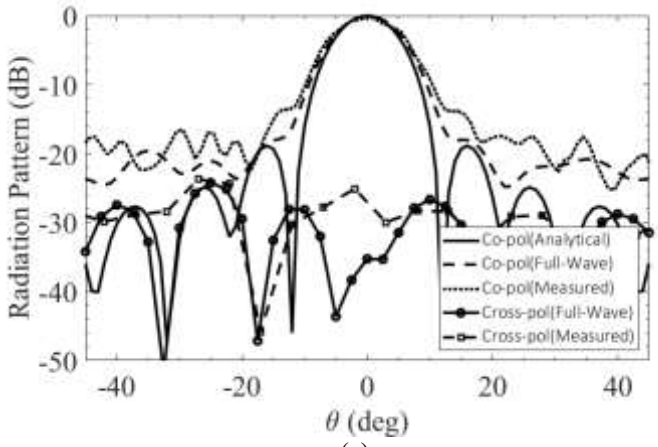

(a)

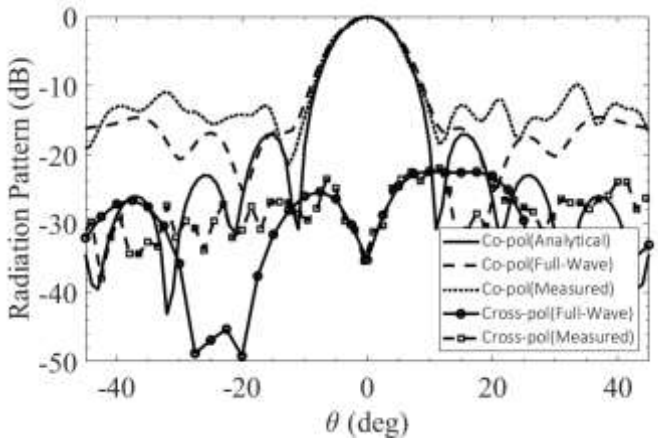

(b)

Figure 4-24 Simulated and measured co- and cross-polar far field E-plane (a) and H-plane (b) radiation pattern at 20 GHz.

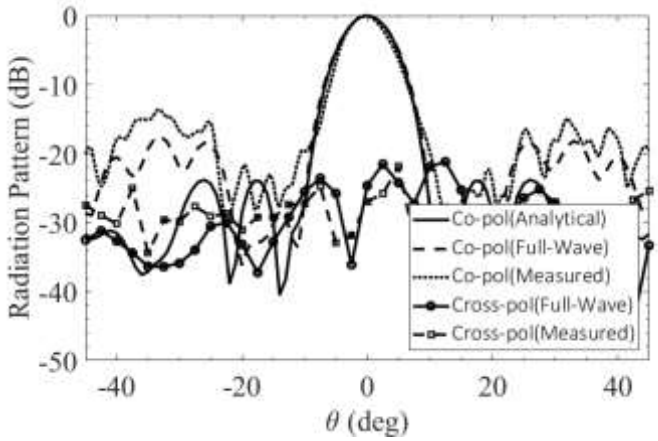

(a)

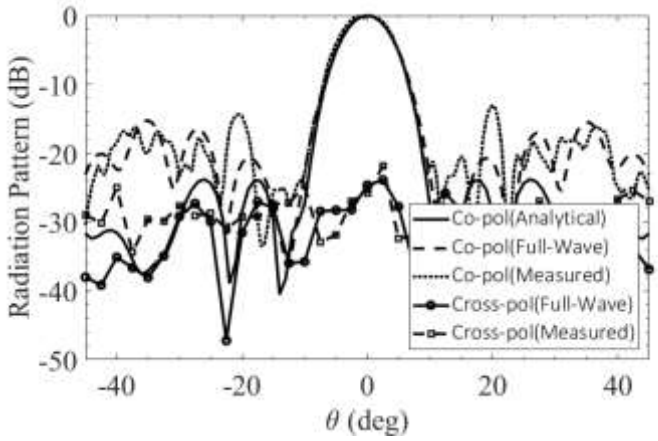

(b)

Figure 4-25 Simulated and measured co- and cross-polar far field E-plane (a) and H-plane (b) radiation pattern at 30 GHz.

aperture efficiency of 23%. A -1 dB gain bandwidth of 4.5% is achieved corresponding to 1.35 GHz. It is worth noticing that the maximum discrepancy between the measured and simulated gain is approximately 0.7 dB in both bands.

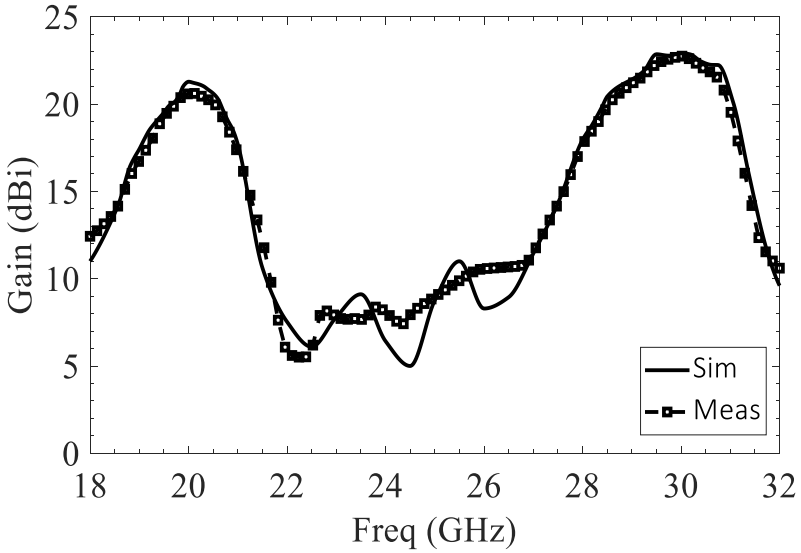

Figure 4-26 Simulated and measured gain vs frequency.

The performance of the proposed design is compared with other TA configurations in Table 4-4. Limiting the comparison with other dual-band dual-polarized TAs, namely [76], [77], [78], [79], the proposed configuration has a significantly thinner profile, by at least 50%. The efficiency is also improved when compared to [76], which operates in the same band. Other TA designs reported in Table 4-4, namely [82] and [67], exhibit a comparable profile but are dual-linearly polarized and have lower aperture efficiency due to their 1-bit phase resolution. In contrast, the example in [68] can be only utilized for circular polarization and covers a different frequency range. Thus, among the aforementioned works, the proposed antenna offers the best compromise between overall thickness and aperture efficiency for dual-band dual-polarized transmitarrays at K/Ka-band.

Table 4-4 Comparison between the proposed antenna and other works.

Ref.	Center Freq. (GHz)	Overall Thickness	Pol.	Aperture Efficiency (%)	Gain BW (%)	
					-1 dB	-3 dB
[76]	20/30	0.68λ_0	CP	10/6	-	10/7
[77]	12.5/14.25	0.55λ_0	Dual Pol	38/46	-	4.2/ 6.3
[78]	13.5/22	0.66λ_0	Dual Pol	34/27	6/6	-
[79]	11/12.5	0.5λ_0	Dual Pol	38/34	6.8/ 5.4	-
[82]	19.8/29.1	0.25λ_0	Dual LP	25.1/20	-	19.8/12
[67]	20/30	0.17λ_0	Dual LP	21.2/20.1	10.7/ 8.3	11.3/ 11.4
[68]	12/14.2	0.075 λ_0	CP	32.2/28.9	-	7.5/7
This work	20/30	0.24 λ_0	Dual Pol	27/23	5/4.5	8.8/ 8.3

Chapter 5: Conclusions and future works

This doctoral research has contributed novel insights and designs in the field of non-terrestrial networks (NTN) and satellite communications. Two different approaches were taken into account in the attempt to simplify the architecture of arrays and phased arrays that are key building blocks in NTN systems.

Two designs were introduced, namely a 2D electronically steerable parasitic array radiator (ESPAR) and a dual-band transmitarray antenna. Both design solutions have demonstrated promising performance in terms of beam scanning and dual-band operation. Both design implementations leveraged a common approach, utilizing both an analytical model and a structured design methodology. Validation was performed through an in-depth experimental assessment. Results were well received in the scientific community and they were presented at main conferences of the field and in the main technical journals.

As a next step, the focus for future work will involve the development of circularly polarized clustered phased array consisting of ESPAR subarray systems optimized for K-band frequencies. This expansion aims to enhance the versatility and adaptability of ESPAR antennas, catering to specific frequency requirements and application scenarios. Additionally, the research will delve into the refinement and implementation of high-gain dual-band transmitarray antennas. This avenue holds potential for addressing the demand for efficient, cost-effective, and low-profile antenna solutions in satellite communications. These future endeavors aim to contribute further to the advancement of antenna technologies, offering solutions that are not only innovative but also tailored to meet the evolving needs of next-generation wireless communication systems.

Bibliography

[1] R. L. Haupt, *Wireless communications systems: an introduction*. Hoboken, NJ: John Wiley & Sons, Inc, 2020.

[2] T. S. Rappaport, *Wireless communications: principles and practice*, 2. ed., 18. printing. in Prentice Hall communications engineering and emerging technologies series. Upper Saddle River, NJ: Prentice Hall, 2009.

[3] A. F. Molisch, *Wireless communications*, 2nd ed. Chichester, West Sussex, U.K: Wiley : IEEE, 2011.

[4] E. Yaacoub e M.-S. Alouini, «A Key 6G Challenge and Opportunity—Connecting the Base of the Pyramid: A Survey on Rural Connectivity», *Proc. IEEE*, vol. 108, fasc. 4, pp. 533–582, apr. 2020, doi: 10.1109/JPROC.2020.2976703.

[5] M. Mozaffari, A. Taleb Zadeh Kasgari, W. Saad, M. Bennis, e M. Debbah, «Beyond 5G With UAVs: Foundations of a 3D Wireless Cellular Network», *IEEE Trans. Wireless Commun.*, vol. 18, fasc. 1, pp. 357–372, gen. 2019, doi: 10.1109/TWC.2018.2879940.

[6] M. K. Bahare *et al.*, «The 6G Architecture Landscape - European perspective», feb. 2023, doi: 10.5281/ZENODO.7313232.

[7] G. Araniti, A. Iera, S. Pizzi, e F. Rinaldi, «Toward 6G Non-Terrestrial Networks», *IEEE Network*, vol. 36, fasc. 1, pp. 113–120, gen. 2022, doi: 10.1109/MNET.011.2100191.

[8] M. Giordani e M. Zorzi, «Satellite Communication at Millimeter Waves: a Key Enabler of the 6G Era», in *2020 International Conference on Computing, Networking and Communications (ICNC)*, Big Island, HI, USA: IEEE, feb. 2020, pp. 383–388. doi: 10.1109/ICNC47757.2020.9049651.

[9] M. Giordani e M. Zorzi, «Non-Terrestrial Networks in the 6G Era: Challenges and Opportunities», *IEEE Network*, vol. 35, fasc. 2, pp. 244–251, mar. 2021, doi: 10.1109/MNET.011.2000493.

[10] J. Rendon Schneir e Y. Xiong, «Cost analysis of network sharing in FTTH/PONs», *IEEE Commun. Mag.*, vol. 52, fasc. 8, pp. 126–134, ago. 2014, doi: 10.1109/MCOM.2014.6871680.

[11] K. T. Li, C. A. Hofmann, H. Reder, e A. Knopp, «A Techno-Economic Assessment and Tradespace Exploration of Low Earth Orbit Mega-Constellations», *IEEE Commun. Mag.*, vol. 61, fasc. 2, pp. 24–30, feb. 2023, doi: 10.1109/MCOM.001.2200312.

[12] M. Handley, «Delay is Not an Option: Low Latency Routing in Space», in *Proceedings of the 17th ACM Workshop on Hot Topics in Networks*, Redmond WA USA: ACM, nov. 2018, pp. 85–91. doi: 10.1145/3286062.3286075.

[13] M. Handley, «Using ground relays for low-latency wide-area routing in megaconstellations», in *Proceedings of the 18th ACM Workshop on Hot Topics in Networks*, Princeton NJ USA: ACM, nov. 2019, pp. 125–132. doi: 10.1145/3365609.3365859.

[14] A. Guidotti *et al.*, «Satellite-enabled LTE systems in LEO constellations», in *2017 IEEE International Conference on Communications Workshops (ICC Workshops)*, Paris, France: IEEE, mag. 2017, pp. 876–881. doi: 10.1109/ICCW.2017.7962769.

[15] A. Guidotti *et al.*, «Architectures and Key Technical Challenges for 5G Systems Incorporating Satellites», *IEEE Trans. Veh. Technol.*, vol. 68, fasc. 3, pp. 2624–2639, mar. 2019, doi: 10.1109/TVT.2019.2895263.
[16] F. Rinaldi *et al.*, «Non-Terrestrial Networks in 5G & Beyond: A Survey», *IEEE Access*, vol. 8, pp. 165178–165200, 2020, doi: 10.1109/ACCESS.2020.3022981.
[17] I. Del Portillo, B. G. Cameron, e E. F. Crawley, «A technical comparison of three low earth orbit satellite constellation systems to provide global broadband», *Acta Astronautica*, vol. 159, pp. 123–135, giu. 2019, doi: 10.1016/j.actaastro.2019.03.040.
[18] M. Mathis, J. Semke, J. Mahdavi, e T. Ott, «The macroscopic behavior of the TCP congestion avoidance algorithm», *SIGCOMM Comput. Commun. Rev.*, vol. 27, fasc. 3, pp. 67–82, lug. 1997, doi: 10.1145/263932.264023.
[19] M. R. Palattella, S. Scanzio, e S. C. Ergen, A c. di, *Ad-hoc, mobile, and wireless networks: 18th International Conference on Ad-Hoc Networks and Wireless, ADHOC-NOW 2019, Luxembourg, Luxembourg, October 1–3, 2019: proceedings*. in Lecture notes in computer science, no. 11803. Cham: Springer, 2019.
[20] G. Amendola *et al.*, «Low-Earth Orbit User Segment in the Ku and Ka-Band: An Overview of Antennas and RF Front-End Technologies», *IEEE Microwave*, vol. 24, fasc. 2, pp. 32–48, feb. 2023, doi: 10.1109/MMM.2022.3217961.
[21] «Multi-purpose terminal: Airbone stabilized VSAT system, [online] Available: https://orbit-cs.com/wp-content/uploads/2021/08/Orbit-MPT-DS-v0.03.pdf.»
[22] «G-18L Ku-/Ka-band antenna: Hybrid satellite antenna for mobility, [online] Available: https://www.viasat.com/content/dam/us-site/antenna-systems/documents/1229461_G-18L_KuKa_Datasheet_006_web.pdf.»
[23] «KuKarray-2L antenna: Hybrid Ka-band/Ku-band satellite antenna for mobility, [online] Available: https://www.viasat.com/content/dam/us-site/antenna-systems/documents/1229461_KuKarray2L_Datasheet_005_web.pdf.»
[24] «F. Tiezzi, S. Vaccaro, D. Llorens, C. Dominguez and M. Fajardo, "Ku-band hybrid phased array antennas for mobile satellite communication systems," 2013 7th European Conference on Antennas and Propagation (EuCAP), Gothenburg, Sweden, 2013, pp. 1605-1608.»,
[25] G. Han, B. Du, W. Wu, e B. Yang, «A Novel Hybrid Phased Array Antenna for Satellite Communication on-the-Move in Ku-band», *IEEE Trans. Antennas Propagat.*, vol. 63, fasc. 4, pp. 1375–1383, apr. 2015, doi: 10.1109/TAP.2015.2389951.
[26] «R. Vincenti Gatti, L. Marcaccioli, E. Sbarra, and R. Sorrentino, "Flat array antenna for Ku-band mobile satellite terminals," in Proc. 5th Eur. Conf. Antennas Propag. (EUCAP), 2011, pp. 2618–2622»,
[27] T. Strober, S. Tubau, E. Girard, H. Legay, G. Goussetis, e M. Ettorre, «Shaped Parallel-Plate Lens for Mechanical Wide-Angle Beam Steering», *IEEE Trans. Antennas Propagat.*, vol. 69, fasc. 12, pp. 8158–8169, dic. 2021, doi: 10.1109/TAP.2021.3090789.
[28] M. Smierzchalski *et al.*, «A Novel Dual-Polarized Continuous Transverse Stub Antenna Based on Corrugated Waveguides—Part I: Principle of Operation and Design», *IEEE Trans. Antennas Propagat.*, vol. 69, fasc. 3, pp. 1302–1312, mar. 2021, doi: 10.1109/TAP.2020.3028236.

[29] M. Smierzchalski *et al.*, «A Novel Dual-Polarized Continuous Transverse Stub Antenna Based on Corrugated Waveguides—Part II: Experimental Demonstration», *IEEE Trans. Antennas Propagat.*, vol. 69, fasc. 3, pp. 1313–1323, mar. 2021, doi: 10.1109/TAP.2020.3037809.
[30] N. T. Nguyen, R. Sauleau, M. Ettorre, e L. Le Coq, «Focal Array Fed Dielectric Lenses: An Attractive Solution for Beam Reconfiguration at Millimeter Waves», *IEEE Trans. Antennas Propagat.*, vol. 59, fasc. 6, pp. 2152–2159, giu. 2011, doi: 10.1109/TAP.2011.2144550.
[31] J. B. Pendry, D. Schurig, e D. R. Smith, «Controlling Electromagnetic Fields», *Science*, vol. 312, fasc. 5781, pp. 1780–1782, giu. 2006, doi: 10.1126/science.1125907.
[32] «"ThinAir® Ku3030: Ku-band SATCOM antenna for global in flight broadband." ThinKom. Accessed: May 2020. [Online]. Avail able: https://www.thinkom.com/wp-content/uploads/2018/09/ ku3030-datasheet_9_18_web.pdf».
[33] «"ThinAir® Ka2517: Ka-band SATCOM antenna for global broad band." ThinKom. Accessed: May 2021. [Online]. Available: https:// www.thinkom.com/wp-content/uploads/2022/03/thinair-ka2517 -datasheet.pdf».
[34] N. Gagnon e A. Petosa, «Using Rotatable Planar Phase Shifting Surfaces to Steer a High-Gain Beam», *IEEE Trans. Antennas Propagat.*, vol. 61, fasc. 6, pp. 3086–3092, giu. 2013, doi: 10.1109/TAP.2013.2253298.
[35] S. A. Matos *et al.*, «High Gain Dual-Band Beam-Steering Transmit Array for Satcom Terminals at Ka-Band», *IEEE Trans. Antennas Propagat.*, vol. 65, fasc. 7, pp. 3528–3539, lug. 2017, doi: 10.1109/TAP.2017.2702658.
[36] B. Yang, Z. Yu, R. Zhang, J. Zhou, e W. Hong, «Local Oscillator Phase Shifting and Harmonic Mixing-Based High-Precision Phased Array for 5G Millimeter-Wave Communications», *IEEE Trans. Microwave Theory Techn.*, vol. 67, fasc. 7, pp. 3162–3173, lug. 2019, doi: 10.1109/TMTT.2019.2899598.
[37] M. Sayginer e G. M. Rebeiz, «An Eight-Element 2–16-GHz Programmable Phased Array Receiver With One, Two, or Four Simultaneous Beams in SiGe BiCMOS», *IEEE Trans. Microwave Theory Techn.*, vol. 64, fasc. 12, pp. 4585–4597, dic. 2016, doi: 10.1109/TMTT.2016.2620144.
[38] S. Payami *et al.*, «Developing the First mmWave Fully-Connected Hybrid Beamformer With a Large Antenna Array», *IEEE Access*, vol. 8, pp. 141282–141291, 2020, doi: 10.1109/ACCESS.2020.3013539.
[39] B. Sadhu, X. Gu, e A. Valdes-Garcia, «The More (Antennas), the Merrier: A Survey of Silicon-Based mm-Wave Phased Arrays Using Multi-IC Scaling», *IEEE Microwave*, vol. 20, fasc. 12, pp. 32–50, dic. 2019, doi: 10.1109/MMM.2019.2941632.
[40] Z. Deng, J. Gan, H. Wei, H. Gong, e X. Guo, «KA-BAND RADIATION PATTERN RECONFIGURABLE ANTENNA BASED ON MICROSTRIP MEMS SWITCHES», *PIER Letters*, vol. 59, pp. 93–99, 2016, doi: 10.2528/PIERL16011201.
[41] M. Sun, Z. Zhang, F. Zhang, e A. Chen, «L/S Multiband Frequency-Reconfigurable Antenna for Satellite Applications», *Antennas Wirel. Propag. Lett.*, vol. 18, fasc. 12, pp. 2617–2621, dic. 2019, doi: 10.1109/LAWP.2019.2945624.
[42] H. Chandra Mohanta, A. Z. Kouzani, e S. K. Mandal, «Reconfigurable Antennas and Their Applications», *ujeee*, vol. 6, fasc. 4, pp. 239–258, ott. 2019, doi: 10.13189/ujeee.2019.060406.

[43] L. Marantis, D. Rongas, A. Paraskevopoulos, C. Oikonomopoulos-Zachos, e A. Kanatas, «Pattern reconfigurable ESPAR antenna for vehicle-to-vehicle communications», *IET Microwaves, Antennas & Propagation*, vol. 12, fasc. 3, pp. 280–286, feb. 2018, doi: 10.1049/iet-map.2017.0209.
[44] M. Burtowy, M. Rzymowski, e L. Kulas, «Low-Profile ESPAR Antenna for RSS-Based DoA Estimation in IoT Applications», *IEEE Access*, vol. 7, pp. 17403–17411, 2019, doi: 10.1109/ACCESS.2019.2895740.
[45] L. Santamaria, F. Ferrero, R. Staraj, e L. Lizzi, «Slot-Based Pattern Reconfigurable ESPAR Antenna for IoT Applications», *IEEE Trans. Antennas Propagat.*, vol. 69, fasc. 7, pp. 3635–3644, lug. 2021, doi: 10.1109/TAP.2020.3044399.
[46] T. Bertuch, R. Joseph, e K. Herbertz, «Size-Limited Q-Band Circular Switched Parasitic Array Antenna With Small Elevation Beamwidth», *IEEE Trans. Antennas Propagat.*, vol. 63, fasc. 11, pp. 4749–4758, nov. 2015, doi: 10.1109/TAP.2015.2477516.
[47] M. Rzymowski e L. Kulas, «Two-Row ESPAR Antenna With Simple Elevation and Azimuth Beam Switching», *Antennas Wirel. Propag. Lett.*, vol. 20, fasc. 9, pp. 1745–1749, set. 2021, doi: 10.1109/LAWP.2021.3095394.
[48] «Harrington, R. F., and J. R. Mautz. “Reactively loaded directive arrays.” Office of Naval Research and Syracuse University (1974).».
[49] R. Harrington, «Reactively controlled directive arrays», *IEEE Trans. Antennas Propagat.*, vol. 26, fasc. 3, pp. 390–395, mag. 1978, doi: 10.1109/TAP.1978.1141852.
[50] Y. Yusuf e Xun Gong, «A Low-Cost Patch Antenna Phased Array With Analog Beam Steering Using Mutual Coupling and Reactive Loading», *Antennas Wirel. Propag. Lett.*, vol. 7, pp. 81–84, 2008, doi: 10.1109/LAWP.2008.916689.
[51] J. J. Luther, S. Ebadi, e X. Gong, «A Low-Cost 2x2 Planar Array of Three-Element Microstrip Electrically Steerable Parasitic Array Radiator (ESPAR) Subcells», *IEEE Trans. Microwave Theory Techn.*, vol. 62, fasc. 10, pp. 2325–2336, ott. 2014, doi: 10.1109/TMTT.2014.2345335.
[52] W. Ouyang e X. Gong, «An Electronically Steerable Parasitic Array Radiator (ESPAR) Using Cavity-Backed Slot Antennas», *Antennas Wirel. Propag. Lett.*, vol. 18, fasc. 4, pp. 757–761, apr. 2019, doi: 10.1109/LAWP.2019.2902037.
[53] M. Ranjbar Nikkhah, J. Rashed-Mohassel, e A. A. Kishk, «Compact Low-Cost Phased Array of Dielectric Resonator Antenna Using Parasitic Elements and Capacitor Loading», *IEEE Trans. Antennas Propagat.*, vol. 61, fasc. 4, pp. 2318–2321, apr. 2013, doi: 10.1109/TAP.2012.2237535.
[54] W. Ouyang e X. Gong, «A 20-Element Cavity-Backed Slot Electronically Steerable Parasitic Array Radiator (ESPAR) With 2-D Beamsteering and Minimized Beam Squint», *Antennas Wirel. Propag. Lett.*, vol. 19, fasc. 8, pp. 1420–1424, ago. 2020, doi: 10.1109/LAWP.2020.3004595.
[55] M. Ranjbar Nikkhah, P. Loghmannia, J. Rashed-Mohassel, e A. A. Kishk, «Theory of ESPAR Design With Their Implementation in Large Arrays», *IEEE Trans. Antennas Propagat.*, vol. 62, fasc. 6, pp. 3359–3364, giu. 2014, doi: 10.1109/TAP.2014.2309958.
[56] R. Movahedinia, M. R. Chaharmir, A. R. Sebak, M. Ranjbar Nikkhah, e A. A. Kishk, «Realization of Large Dielectric Resonator Antenna ESPAR», *IEEE Trans. Antennas Propagat.*, vol. 65, fasc. 7, pp. 3744–3749, lug. 2017, doi: 10.1109/TAP.2017.2705024.

[57] R. De Marco, L. Boccia, E. Arnieri, e G. Amendola, «Phased arrays based on hybrid clusters», in *2022 Microwave Mediterranean Symposium (MMS)*, Pizzo Calabro, Italy: IEEE, mag. 2022, pp. 1–4. doi: 10.1109/MMS55062.2022.9825606.
[58] K.-F. Lee e T. Huynh, «Single-layer single-patch wideband microstrip antenna», *Electronics Letters*, vol. 31, fasc. 16, pp. 1310–1312, ago. 1995, doi: 10.1049/el:19950950.
[59] R. Jedlicka, M. Poe, e K. Carver, «Measured mutual coupling between microstrip antennas», *IEEE Trans. Antennas Propagat.*, vol. 29, fasc. 1, pp. 147–149, gen. 1981, doi: 10.1109/TAP.1981.1142529.
[60] T. A. Milligan, *Modern antenna design*, Second edition. Hoboken, N.J.: IEEE Press : Wiley-Interscience, 2005.
[61] R. De Marco, E. Arnieri, G. Amendola, e L. Boccia, «A Hybrid Radiating Element for 1-D Scanning Clustered Phased Array», *EuMW2023*, doi: in press.
[62] R. De Marco, E. Arnieri, G. Amendola, e L. Boccia, «Microstrip ESPAR Antenna with Conical Beam Scanning», *AWPL*, doi: in review.
[63] R. De Marco, E. Arnieri, G. Amendola, e L. Boccia, «Electronically Steerable Parasitic Array Radiators (ESPAR) for Efficient Phased Array Design», in *2023 IEEE International Workshop on Technologies for Defense and Security (TechDefense)*, Rome, Italy: IEEE, nov. 2023, pp. 373–377. doi: 10.1109/TechDefense59795.2023.10380915.
[64] «R. De Marco, A. Bordbar, F. Greco, C. Mustacchio, S. Zahran, G. Amendola, E. Arnieri, and L. Boccia , "K-band Microstrip ESPAR Antenna Integrated into Large Array ," accepted for presentation in 18th European Conference on Antennas and Propagation (EuCAP), Glasgow, Scotland, 2023.»,
[65] A. H. Abdelrahman, F. Yang, A. Z. Elsherbeni, e P. Nayeri, *Analysis and Design of Transmitarray Antennas*. in Synthesis Lectures on Antennas. Cham: Springer International Publishing, 2017. doi: 10.1007/978-3-031-01541-0.
[66] J. Huang e J. A. Encinar, *Reflectarray Antennas*. in IEEE Press Series on Electromagnetic Wave Theory. Wiley, 2007. [Online]. Disponibile su: https://books.google.it/books?id=JNwYCzFt8Z0C
[67] K. T. Pham, R. Sauleau, E. Fourn, F. Diaby, A. Clemente, e L. Dussopt, «Dual-Band Transmitarrays With Dual-Linear Polarization at Ka-Band», *IEEE Trans. Antennas Propagat.*, vol. 65, fasc. 12, pp. 7009–7018, dic. 2017, doi: 10.1109/TAP.2017.2762011.
[68] Y.-M. Cai *et al.*, «Dual-Band Circularly Polarized Transmitarray With Single Linearly Polarized Feed», *IEEE Trans. Antennas Propagat.*, vol. 68, fasc. 6, pp. 5015–5020, giu. 2020, doi: 10.1109/TAP.2019.2963594.
[69] S. Kamada, N. Michishita, e Y. Yamada, «Metamaterial lens antenna using dielectric resonators for wide angle beam scanning», in *2010 IEEE Antennas and Propagation Society International Symposium*, Toronto, ON: IEEE, lug. 2010, pp. 1–4. doi: 10.1109/APS.2010.5561780.
[70] Q. Cheng, H. F. Ma, e T. J. Cui, «Broadband planar Luneburg lens based on complementary metamaterials», *Appl. Phys. Lett.*, vol. 95, fasc. 18, p. 181901, nov. 2009, doi: 10.1063/1.3257375.
[71] Y. Zhang, R. Mittra, e W. Hong, «On the Synthesis of a Flat Lens using a Wideband Low-Reflection Gradient-Index Metamaterial», *Journal of Electromagnetic Waves and Applications*, vol. 25, fasc. 16, pp. 2178–2187, gen. 2011, doi: 10.1163/156939311798147015.

[72] M. Li e N. Behdad, «Ultra-wideband, true-time-delay, metamaterial-based microwave lenses», in *Proceedings of the 2012 IEEE International Symposium on Antennas and Propagation*, Chicago, IL, USA: IEEE, lug. 2012, pp. 1–2. doi: 10.1109/APS.2012.6349044.

[73] A. H. Abdelrahman, A. Z. Elsherbeni, e F. Yang, «Transmission Phase Limit of Multilayer Frequency-Selective Surfaces for Transmitarray Designs», *IEEE Trans. Antennas Propagat.*, vol. 62, fasc. 2, pp. 690–697, feb. 2014, doi: 10.1109/TAP.2013.2289313.

[74] S. Datthanasombat, A. Prata, L. R. Arnaro, J. A. Harrell, S. Spitz, e J. Perret, «Layered lens antennas», in *IEEE Antennas and Propagation Society International Symposium. 2001 Digest. Held in conjunction with: USNC/URSI National Radio Science Meeting (Cat. No.01CH37229)*, Boston, MA, USA: IEEE, 2001, pp. 777–780. doi: 10.1109/APS.2001.959839.

[75] A. H. Abdelrahman, A. Z. Elsherbeni, e Fan Yang, «Transmitarray Antenna Design Using Cross-Slot Elements With No Dielectric Substrate», *Antennas Wirel. Propag. Lett.*, vol. 13, pp. 177–180, 2014, doi: 10.1109/LAWP.2014.2298851.

[76] H. Hasani, J. S. Silva, S. Capdevila, M. Garcia-Vigueras, e J. R. Mosig, «Dual-Band Circularly Polarized Transmitarray Antenna for Satellite Communications at (20, 30) GHz», *IEEE Trans. Antennas Propagat.*, vol. 67, fasc. 8, pp. 5325–5333, ago. 2019, doi: 10.1109/TAP.2019.2912495.

[77] A. Aziz, F. Yang, S. Xu, M. Li, e H.-T. Chen, «A High-Gain Dual-Band and Dual-Polarized Transmitarray Using Novel Loop Elements», *Antennas Wirel. Propag. Lett.*, vol. 18, fasc. 6, pp. 1213–1217, giu. 2019, doi: 10.1109/LAWP.2019.2912645.

[78] S. Yang, Z. Yan, X. Li, e M. Cai, «DUAL-BAND DUAL-POLARIZED transmitarray with independent control of polarization at each band», *Int J RF Mic Comp-Aid Eng*, vol. 32, fasc. 2, feb. 2022, doi: 10.1002/mmce.22957.

[79] M. O. Bagheri, H. R. Hassani, e B. Rahmati, «Dual-band, dual-polarised metallic slot transmitarray antenna», *IET Microwaves, Antennas & Propagation*, vol. 11, fasc. 3, pp. 402–409, feb. 2017, doi: 10.1049/iet-map.2016.0159.

[80] A. Aziz, F. Yang, S. Xu, e M. Li, «An Efficient Dual-Band Orthogonally Polarized Transmitarray Design Using Three-Dipole Elements», *Antennas Wirel. Propag. Lett.*, vol. 17, fasc. 2, pp. 319–322, feb. 2018, doi: 10.1109/LAWP.2017.2788412.

[81] R. Y. Wu, Y. B. Li, W. Wu, C. B. Shi, e T. J. Cui, «High-Gain Dual-Band Transmitarray», *IEEE Trans. Antennas Propagat.*, vol. 65, fasc. 7, pp. 3481–3488, lug. 2017, doi: 10.1109/TAP.2017.2705074.

[82] R. Madi, A. Clemente, e R. Sauleau, «Dual-Band Dual-Linearly Polarized Transmitarray at Ka-Band», in *2020 50th European Microwave Conference (EuMC)*, Utrecht, Netherlands: IEEE, gen. 2021, pp. 340–343. doi: 10.23919/EuMC48046.2021.9337962.

[83] P. Naseri, S. A. Matos, J. R. Costa, C. A. Fernandes, e N. J. G. Fonseca, «Dual-Band Dual-Linear-to-Circular Polarization Converter in Transmission Mode Application to K/Ka -Band Satellite Communications», *IEEE Trans. Antennas Propagat.*, vol. 66, fasc. 12, pp. 7128–7137, dic. 2018, doi: 10.1109/TAP.2018.2874680.

[84] M. Cai, Z. Yan, F. Fan, S. Yang, e X. Li, «Double-Layer Ku/K Dual-Band Orthogonally Polarized High-Efficiency Transmitarray Antenna», *IEEE Access*, vol. 9, pp. 89143–89149, 2021, doi: 10.1109/ACCESS.2021.3089489.
[85] R. De Marco, E. Arnieri, F. Greco, A. Bordbar, G. Amendola, e L. Boccia, «Low-Profile Dual-Band Dual-Polarized Transmitarray Antenna Based on Multilayer Frequency Selective Surfaces», *IEEE Trans. Antennas Propagat.*, vol. 71, fasc. 9, pp. 7354–7362, set. 2023, doi: 10.1109/TAP.2023.3296257.
[86] R. Pous e D. M. Pozar, «A frequency-selective surface using aperture-coupled microstrip patches», *IEEE Trans. Antennas Propagat.*, vol. 39, fasc. 12, pp. 1763–1769, dic. 1991, doi: 10.1109/8.121598.
[87] S. B. Cohn, «Direct-Coupled-Resonator Filters», *Proceedings of the IRE*, vol. 45, fasc. 2, pp. 187–196, feb. 1957, doi: 10.1109/JRPROC.1957.278389.
[88] L. Boccia, I. Russo, G. Amendola, e G. Di Massa, «Multilayer Antenna-Filter Antenna for Beam-Steering Transmit-Array Applications», *IEEE Transactions on Microwave Theory and Techniques*, vol. 60, fasc. 7, pp. 2287–2300, lug. 2012, doi: 10.1109/TMTT.2012.2195673.
[89] Shivnarayan e B. R. Vishvakarma, «Analysis of slot loaded microstrip patch antenna», in *IEEE Antennas and Propagation Society Symposium, 2004.*, Monterey, CA, USA: IEEE, 2004, pp. 2420-2423 Vol.3. doi: 10.1109/APS.2004.1331861.
[90] Ansys HFSS, v. 2019. [Online]. Disponibile su: v 2019
[91] R. Luebbers e B. Munk, «Some effects of dielectric loading on periodic slot arrays», *IEEE Trans. Antennas Propagat.*, vol. 26, fasc. 4, pp. 536–542, lug. 1978, doi: 10.1109/TAP.1978.1141887.
[92] C. H. Tsao, Y. M. Hwang, F. Kilburg, e F. Dietrich, «Aperture-coupled patch antennas with wide-bandwidth and dual-polarization capabilities», in *International Symposium, Antennas and Propagation 1988 IEEE AP-S*, giu. 1988, pp. 936–939 vol.3. doi: 10.1109/APS.1988.94241.
[93] A. Clemente, L. Dussopt, R. Sauleau, P. Potier, e P. Pouliguen, «Focal Distance Reduction of Transmit-Array Antennas Using Multiple Feeds», *Antennas Wirel. Propag. Lett.*, vol. 11, pp. 1311–1314, 2012, doi: 10.1109/LAWP.2012.2227105.
[94] M. ŻŻebrowski, «Illumination and Spillover Efficiency Calculations for Rectangular Reflectarray Antennas». Consultato: 28 novembre 2022. [Online]. Disponibile su: http://highfrequencyelectronics.com/Dec12/1212_HFE_reflectarray.pdf

Publications

- R. De Marco, L. Boccia, E. Arnieri, e G. Amendola, «Phased arrays based on hybrid clusters», in *2022 Microwave Mediterranean Symposium (MMS)*, Pizzo Calabro, Italy: IEEE, mag. 2022, pp. 1–4. doi: 10.1109/MMS55062.2022.9825606.
- E. Arnieri, R. De Marco, F. Greco, L. Boccia and G. Amendola, "A Dual-Band Dual-Linear Polarization Transmitarray Unit Cell for Ka-Band Applications," 2022 IEEE International Symposium on Antennas and Propagation and USNC-URSI Radio Science Meeting (AP-S/URSI), Denver, CO, USA, 2022, pp. 2046-2047, doi: 10.1109/AP-S/USNC-URSI47032.2022.9886191.
- R. De Marco, L. Boccia, G. Amendola, E. Arnieri, F. Greco and A. Bordbar, "Low Profile Dual-Band Dual-Polarized Transmitarray Antenna for Satellite Communications," 2023 17th European Conference on Antennas and Propagation (EuCAP), Florence, Italy, 2023, pp. 1-4, doi: 10.23919/EuCAP57121.2023.10133627.
- R. De Marco, E. Arnieri, F. Greco, A. Bordbar, G. Amendola and L. Boccia, "Low-Profile Dual-Band Dual-Polarized Transmitarray Antenna Based on Multilayer Frequency Selective Surfaces," in IEEE Transactions on Antennas and Propagation, vol. 71, no. 9, pp. 7354-7362, Sept. 2023, doi: 10.1109/TAP.2023.3296257.
- M. Mercuri, E. Arnieri, R. De Marco, P. Veltri, F. Crupi and L. Boccia, "Reconfigurable Intelligent Surface-Aided Indoor Radar Monitoring: A Feasibility Study," in IEEE Journal of Electromagnetics, RF and Microwaves in Medicine and Biology, vol. 7, no. 4, pp. 354-364, Dec. 2023, doi: 10.1109/JERM.2023.3298730.
- R. D. Marco, E. Arnieri, G. Amendola and L. Boccia, "A Hybrid Radiating Element for 1-D Scanning Clustered Phased Array," 2023 53rd European Microwave Conference (EuMC), Berlin, Germany, 2023, pp. 823-826, doi: 10.23919/EuMC58039.2023.10290658.
- S. R. Zahran et al., "Bondwire Integration Challenges in E-band Systems: from PCB to Die Level," 2023 53rd European Microwave Conference (EuMC), Berlin, Germany, 2023, pp. 846-849, doi: 10.23919/EuMC58039.2023.10290383.
- R. De Marco, E. Arnieri, G. Amendola and L. Boccia, "Microstrip ESPAR Antenna With Conical Beam Scanning," in IEEE Antennas and Wireless Propagation Letters, vol. 23, no. 1, pp. 174-178, Jan. 2024, doi: 10.1109/LAWP.2023.3320790.
- R. De Marco, E. Arnieri, G. Amendola and L. Boccia, "Electronically Steerable Parasitic Array Radiators (ESPAR) for Efficient Phased Array Design," 2023 IEEE International Workshop on Technologies for Defense and Security (TechDefense), Rome, Italy, 2023, pp. 373-377, doi: 10.1109/TechDefense59795.2023.10380915.
- A. Bordbar, R. De Marco, L. Boccia, E. Arnieri and G. Amendola, "Synthesis of a Planar 2D Butler Matrix: A Showcase with a 3×3 Array," 2024 18th European Conference on Antennas and Propagation (EuCAP), Glasgow, United Kingdom, 2024, pp. 1-5, doi: 10.23919/EuCAP60739.2024.10501500.

- R. De Marco et al., "K-band Microstrip ESPAR Antenna Integrated into Large Array," 2024 18th European Conference on Antennas and Propagation (EuCAP), Glasgow, United Kingdom, 2024, pp. 1-5, doi: 10.23919/EuCAP60739.2024.10501280.